Field-theoretic simulations with advanced interaction potentials

Alexander Weyman

Field-Theoretic Simulations with Advanced Interaction Potentials

Diss. ETH No. 28665

DISS. ETH NO. 28665

FIELD-THEORETIC SIMULATIONS WITH ADVANCED INTERACTION POTENTIALS

A thesis submitted to attain the degree of

DOCTOR OF SCIENCES of ETH ZURICH
(Dr. sc. ETH Zurich)

presented by

ALEXANDER WEYMAN
M.Sc. in Physics, University of Stuttgart
born on 20 February 1991

accepted on the recommendation of

Prof. Dr. Hans Christian Öttinger
Prof. Dr. Glenn H. Fredrickson
Prof. Dr. Vlasis G. Mavrantzas
Prof. Dr. Robert A. Riggleman

2022

DOI: 10.3929/ethz-b-000570125

Dedicated with love and gratitude
to Mathias Lehnert (1928–2021).

ABSTRACT

In modern computational research in soft matter, especially in polymer science, field-theoretic simulations have evolved into a powerful complement to particle-based simulations, and quite often to a superior tool, guiding the design, engineering, and discovery of new materials. At the heart of the field-theoretic modeling is an approximation-free particle-to-field transformation that decouples pair interactions in the underlying classical particle model, thus arriving at an exact statistical theory incorporating continuous auxiliary fields interacting with each other through an inverted representation of the original potential. While this decoupling is the cornerstone of the framework, at the same time, the appearance of the inverted potential imposes major limitations that restrict its applicability to relatively simple (from a physical point of view) interaction models.

In this thesis, a systematic classification of commonly used interactions is proposed for the first time, and the inverse potential problem is formally stated and addressed. Guided by the classification scheme, important aspects of the inverse potential problem are brought up and analyzed in detail, and systematic solutions are proposed that help incorporate into the framework advanced interactions. First, the known concept of effective potentials is revisited and the underlying idea of field masking is exploited to formulate new effective potentials accounting for more physically relevant interatomic interactions. Second, a new perspective is opened by showing how field-theoretic simulations can be coupled with pure particle methods like molecular dynamics, the inverse potential acting as an interface to pass important structural information from one to the other. Third, two methods are proposed and implemented for the direct calculation of the inverse potential of an advanced interaction model, the so-called Morse potential that is broadly used in particle-based simulations. One is numerical involving direct inversion on a regular grid or deconvolution. The other is purely analytical and is based on representing attractive and repulsive contributions to the Morse potential as higher order derivatives of the Dirac delta function.

Given the profound nature of physical interaction models, the implications of the work presented in this thesis are manifold: A) New models are now available to be incorporated in the field-theoretic framework, thus opening totally new directions to the field, possibly defining a new generation of such field-based simulations. B) Simulation methods of totally different nature, particle-based on the one hand and field-based on the other hand, have been formally bridged and coupled. C) The path followed in this thesis to develop new potentials is open to extensions, for example, through the use of more general convolutions building on the fundamental concepts from statistical mechanics mastered in this thesis.

ZUSAMMENFASSUNG

In der heutigen computergestützten Forschung auf dem Gebiet der weichen Materie, insbesondere in der Polymerforschung, haben sich feldtheoretische Simulationen zu einer leistungsstarken Ergänzung zu teilchenbasierten Simulationen und nicht selten zu einem überlegenen Hilfsmittel entwickelt, das Design, Konstruktion und Entdeckung neuer Materialien vorantreibt. Im Mittelpunkt der feldtheoretischen Modellierung steht eine näherungsfreie Teilchen-zu-Feld-Transformation, durch die Paarwechselwirkungen im zugrundeliegenden klassischen Teilchenmodell entkoppelt werden, so dass eine exakte statistische Theorie mit stetigen Hilfsfeldern erzeugt wird, die durch eine invertierte Form des ursprünglichen Potentials miteinander wechselwirken. Während diese Entkopplung den eigentlichen Kern des Formalismus ausmacht, schränkt das auftretende invertierte Potential seine Anwendbarkeit auf (aus physikalischer Sicht) relativ einfache Wechselwirkungsmodelle ein.

In dieser Arbeit wird erstmals eine systematische Klassifizierung häufig verwendeter Wechselwirkungen vorgeschlagen und das Problem des inversen Potentials formell beschrieben und behandelt. Geleitet von diesem Klassifizierungsschema werden die zentralen Aspekte des inversen Potentialproblems aufgezeigt und detailliert untersucht, sowie systematische Lösungen vorgeschlagen, die es ermöglichen, komplexere oder ausgeklügeltere Wechselwirkungen in den Formalismus mit einzubeziehen. Als Erstes wird das bekannte Konzept der effektiven Potentiale wieder aufgegriffen und die zugrundeliegende Idee der Feldmaskierung zur Formulierung neuer effektiver Potentiale weiterentwickelt, wodurch physikalisch relevantere interatomare Wechselwirkungen beschrieben werden können. Zweitens wird in einer neuen Perspektive gezeigt, wie feldtheoretische Simulationen mit reinen Teilchenmethoden, etwa mit der Molekulardynamik, gekoppelt werden können, indem das inverse Potential als Schnittstelle dient, um wichtige Strukturinformationen von einer Methode zur anderen zu übertragen. Drittens werden zwei Methoden zur direkten Berechnung des inversen Potentials eines fortgeschrittenen und in teilchenbasierten Simulationen weit verbreiteten Wechselwirkungsmodells, des sogenannten Morse-Potentials, vorgeschlagen und umgesetzt. Die erste Methode ist numerisch und umfasst die direkte Invertierung auf einem regulären Gitter oder die Lösung durch Rückwärtsfaltung. Die Zweite ist rein analytisch und stützt sich auf die Darstellung der attraktiven und repulsiven Beiträge des Morse-Potentials als Ableitungen höherer Ordnung der Dirac-Delta-Funktion.

In Anbetracht der tiefgründigen Natur physikalischer Wechselwirkungsmodelle haben die in dieser Arbeit vorgestellten Konzepte vielfältige Auswirkungen: A) Es stehen nun neue Modelle zur Verfügung, die in den feldtheoretische Formalismus einbezogen werden können,

wodurch sich völlig neue Perspektiven für das Forschungsfeld eröffnen und möglicherweise eine neue Generation derartiger feldbasierter Simulationen begründet wird. B) Völlig unterschiedliche Simulationsmethoden wie teilchenbasierte auf der einen Seite und feldbasierte auf der anderen Seite wurden formal miteinander verbunden und gekoppelt. C) Der beschriebene Weg zur Entwicklung neuer Potentiale lässt sich weiter ausbauen, z. B. durch die Verwendung allgemeiner Faltungsansätze, die auf den grundlegenden Konzepten der statistischen Mechanik aufbauen und in dieser Arbeit behandelt werden.

CONTENTS

NOTATION

ABBREVIATIONS

AF	Auxiliary Field
BS	Bead-Spring
CFD	Computational Fluid Dynamics
CKE	Chapman–Kolmogorov Equation
CL	Complex Langevin
CS	Coherent States
CV	Collective Variable
DFT	Density Functional Theory
DPD	Dissipative Particle Dynamics
EM	Euler–Maruyama
FEM	Finite Element Method
FFT	Fast Fourier Transform
FT	Fourier Transform
FTS	Field-theoretic Simulations
GER	Gaussian Equivalent Representation
GREM	Gaussian-regularized Edwards Model
HPF	Hybrid Particle-Field
HS	Hubbard–Stratonovich
LJ	Lennard-Jones
MC	Monte Carlo
MD	Molecular Dynamics
RDF	Radial Distribution Function
RFT	Radial Fourier Transform
RMSD	Root-Mean-Square Deviation
SCFT	Self-consistent Field Theory
UV	Ultraviolet

SYMBOLS

d	dimensionality
$\mathcal{D}$	functional integral
$\hat{f}$	shorthand notation for $\mathcal{F}[f]$
$\mathcal{F}[f]$	Fourier transform of the function f
$\mathcal{F}^{-1}[\hat{f}]$	inverse Fourier transform of the function $\hat{f}$
$g(r)$	radial distribution function[1]
$\mathcal{H}$	field-theoretic Hamiltonian
i	imaginary unit (or integer index if used in subscript)
$\boldsymbol{k}$	wave vector
k	wavenumber
k_B	Boltzmann constant
L	box length along each (or indicated) axis[2]
M	number of grid points along each (or indicated) axis[2]
n	number of molecules (chains, monomers or particles)[2]
N	step for discrete schemes
q	chain propagator
Q	reduced partition function[1]
$\boldsymbol{r}$	coordinate vector
r	radial coordinate
$r_{\min}$	Morse parameter
R	box radius
$S(k)$	static structure factor
t	(fictitious) time
T	temperature
$u(\boldsymbol{r})$	pair potential[2]
U	potential energy
$w(\boldsymbol{r})$	auxiliary field[1,2]
$\mathcal{Z}_c$	canonical partition function
β	thermodynamic beta, defined as $(k_B T)^{-1}$
$\Gamma(\boldsymbol{r})$	(masking) function used for convolution[2]
$\delta(\boldsymbol{r})$	Dirac delta function
Δt	(fictitious) time step
ϵ	pair potential energy parameter[2]
$\tilde{\mu}$	chemical potential related field observable[1]
ξ	Morse parameter
ρ_0	bulk fluid density, defined as $\frac{n}{V}$
$\hat{\rho}(\boldsymbol{r})$	microscopic density
$\tilde{\rho}(\boldsymbol{r})$	density field observable[1]
σ	Lennard-Jones parameter
χ	Flory–Huggins chi parameter

CONVENTIONS

Dirac's bra–ket notation in the field-theoretic context

$$\langle w|\hat{\rho}\rangle \equiv \int_V \mathrm{d}^3 r\; w(\boldsymbol{r})\; \hat{\rho}(\boldsymbol{r})$$
$$\langle \hat{\rho}|u|\hat{\rho}\rangle \equiv \int_V \mathrm{d}^3 r \int_V \mathrm{d}^3 r'\; \hat{\rho}(\boldsymbol{r}) u(\boldsymbol{r}-\boldsymbol{r}')\hat{\rho}(\boldsymbol{r}')$$

Fourier transforms

3D Cartesian coordinates:

$$\mathcal{F}\left[f\right](\boldsymbol{k}) \equiv \hat{f}(\boldsymbol{k}) = \int_{\mathbb{R}^3} \mathrm{d}^3 r\; \exp\left(-i\boldsymbol{k}\cdot\boldsymbol{r}\right) f(\boldsymbol{r})$$
$$\mathcal{F}^{-1}\left[\hat{f}\right](\boldsymbol{r}) \equiv f(\boldsymbol{r}) = \frac{1}{(2\pi)^3} \int_{\mathbb{R}^3} \mathrm{d}^3 k\; \exp\left(i\boldsymbol{k}\cdot\boldsymbol{r}\right) \hat{f}(\boldsymbol{k})$$

Spherically symmetric functions in 3D, i.e. $f(\boldsymbol{r}) = f(r)$:

$$\hat{f}(k) = \frac{4\pi}{k} \int_0^\infty \mathrm{d}r\; f(r)\, r\, \sin(kr)$$
$$f(r) = \frac{1}{2\pi^2 r} \int_0^\infty \mathrm{d}k\; \hat{f}(k)\, k\, \sin(kr)$$

Convolutions

Definition:

$$\left[f * g\right](\boldsymbol{r}) \equiv \int_{\mathbb{R}^3} \mathrm{d}^3 r'\; f(\boldsymbol{r}-\boldsymbol{r}')\, g(\boldsymbol{r}')$$

Convolution theorem:

$$\mathcal{F}\left[f * g\right](\boldsymbol{k}) = \hat{f}(\boldsymbol{k})\, \hat{g}(\boldsymbol{k})$$

1 The symbol may have a superscript asterisk to indicate a saddle-point solution.
2 The symbol may be marked with subscript if necessary or to avoid ambiguity.

1

INTRODUCTION

Small minds are concerned with the extraordinary, great minds with the ordinary.

— Blaise Pascal

Polymers seem to have gone out of fashion these days. In the general public, the drastic reduction to the term *plastics* is accompanied by widespread prejudice. The highly laudable slogan *Say No to Single-use Plastic!*[1] in support of sustainable and environmentally conscious societies is even too hastily shortened to just *Say No to Plastic!*[2]. This lack of differentiation gives the impression that plastics (and, according to this public understanding, polymers as well) are obsolete and environmentally harmful materials whose use should be avoided wherever possible.

In this context, polymers have been unfairly discredited and their mere reduction to plastic bags and disposable forks is, of course, utter nonsense. Polymers in themselves are essentially molecules made up of repeating chemical units called monomers. The fact that these monomers, linked by covalent bonds, actually form stable macromolecules is not self-evident. It was Hermann Staudinger's pioneering research work in 1920 [1] that laid the foundations for polymer science almost exactly a century ago. Natural polymers (such as cellulose, proteins, or our not-so-old-fashioned DNA double helix) have been joined since those early days by a variety of synthetic polymers. Nowadays, polymers are so fundamentally anchored in the foundation of our technological development that it is almost impossible to find areas of our society and everyday lives in which they do not play a significant role. Remarkably, there are many areas far from disposable plastics in supermarkets, such as medical products and medicines, applications in the energy sector, in the technology sector and also in artistic creative areas, which are typically not associated with the aforementioned public prejudices.

In all application areas, a unique principle of materials modeling with polymers is exploited: Depending on which monomers are used as the building blocks of the polymers and depending on the circumstances under which they are assembled, that is, the physical and chemical conditions under which polymerization takes place, materials with completely different properties can be produced. Although assembling polymers according to the Lego principle may seem simple and primitive in an ideal world, the synthetic fabrication of polymers in the real world quickly encounters difficulties and limitations.

1 Especially the campaigns in India have received international attention being now followed by official governmental measures, see for example `https://pib.gov.in/PressReleasePage.aspx?PRID=1837518` (posted on June 28, 2022).

2 An exemplary case is the popular TEDx talk of a young future scientist: *Say No to Plastic!* from March 1, 2019 available at `https://youtu.be/QRb2UDvACGs`.

Even today, these make the experimental processes seem like they are in their infancy when compared to the sophisticated mechanisms in the formation of proteins or DNA found in nature.[3]

In addition to practical synthesis, there is also the aspect of a profound theoretical understanding of polymers, evident not only from an academic point of view. With the picture of polymers as a generally chaotic entanglement of tiny, string-like chains in mind, it may at first seem hopeless to derive physically sound principles from this microscopic tangle. Yet, at the time polymers were discovered, the scientific and social importance of this entirely new class of materials attracted the attention of many bright minds. It is difficult to give full credit to the contributions of all the scientists involved, but the chemist Paul John Flory was certainly one of the most prominent researchers to pursue Staudinger's hypothesis of covalently bonded polymer chains. Besides his important experimental work, he has contributed significantly to better understand static properties of polymers, which he comprehensively summarized (including the work of others) in his book [3] published in 1953. It so happens that all students of polymer science learn about the Flory exponent and the Flory–Huggins chi parameter; the latter will be revisited later on. Building on these foundations, dynamic properties of polymers were then explored in greater detail in the field of polymer physics. As a significant example, the physicist Pierre-Gilles de Gennes proposed in 1971 to understand the dynamics of polymers by a special type of diffusion of the chains, called reptation, along their axis in a tube bounded by the surrounding molecules [4].[4] Even though de Gennes was awarded the Nobel Prize in Physics in 1991 for his research on polymers,[5] the role of polymer physics per se in the field of physics seems dubious. Physicist Michael Rubinstein, well known for the "Polymer Physics" book [6], gets to the heart of the matter with his question, *Will polymer physics ever become a part of "proper" physics?* [7]. Similar to the seemingly unattractive perception of polymers in the public eye, this further highlights the discouraging barrier for scientists to address questions about the theoretical understanding of polymers at an academic level – in spite of their tremendous societal and technological importance.[6]

What makes the understanding of polymers so difficult is their peculiarity that their typical macroscopic material properties strongly depend on the conformation and cross-linking of the chains, which in turn are dictated by the microscopic structure of the (macro)molecules

3 However, ever newer and more advanced methods in this field (see, e.g., Ref. [2]) give reason for optimism.

4 The reptation model was later further developed by Masao Doi and Samuel Frederick Edwards [5] and also extended to deformable tubes.

5 More precisely, the prize was awarded "for discovering that methods developed for studying order phenomena in simple systems can be generalized to more complex forms of matter, in particular to liquid crystals and polymers", see `https://www.nobelprize.org/prizes/physics/1991/summary/`.

6 From this perspective, it is plausible (and sympathetic) that world-class scientists turn to other fields of research besides polymer physics (seemingly belonging to "proper" physics), and that world-class universities (not-so-sympathetically) consider to close their polymer physics group altogether.

involved. The intra- and interchain interactions of the monomers take on a special importance here, which will be the central focus of this work. Based on the character of the interactions, even for the simple case of linear chains forming block copolymers, an almost unlimited variety of materials can be realized. Owing to this inherent complexity, computational methods are the common tool of choice in the scientific study of polymers. Widely used methods here are those that can be broadly described as computer experiments. Depending on the length and time scales of interest, an attempt is made to model polymers as accurately as possible in order to then analyze their behavior in a way similar to a laboratory experiment. This can be advantageous, for example, to better understand properties through the computer that are difficult (or even impossible) to access experimentally. Less common are, on the other hand, computational endeavors of theory-driven methods, where the description of the entire system is based on a self-contained physical model of mathematical equations.[7] As with the reptation model, these start with an extensive and demanding process of physics-informed model building. Apart from being exceedingly insightful in itself, by its reduction to the relevant physical features of the problems, this process can result in highly efficient and powerful numerical tools for addressing them. The obvious high entry barriers may cause these methods to look like a niche in the theoretical study of polymers. However, it appears reasonable to assume that the chances for further significant breakthroughs in the understanding of these unique materials are fairly good for the latter, physics-informed approach.

We live in exciting times! Our ever-improving interconnectedness makes the world seem smaller, the explosion of computing power in recent decades has opened up a host of new possibilities in a now digital world. Many new fields of research are flourishing in science, and also our societies are undergoing a drastic change driven by new technologies based on, for instance, machine learning and artificial intelligence. Embracing these new possibilities, the work that has led to this dissertation has no less an ambition than to further develop a powerful computational tool for the discovery of new materials. Out of a deep conviction of the absolute necessity and usefulness of physical models in ongoing and future computer-based research, this work builds on a comparatively novel framework, the field-theoretic simulations, of which early concepts were published already in 2001 [8]. This framework enables the computational study of polymers on a physically sound basis, paving the way to exploit the full potential of this seemingly underappreciated but magnificent class of materials.[8] Even though the framework now appears to have moved beyond the early conceptual stage, it exhibits a gross weakness in describing the

7 In this context, already the different interpretations of the equals sign in the various scientific disciplines seem to be telling a lot about the different conceptions of mathematical descriptions.

8 Polymers and their compounds are in fact an exceedingly great class of materials: they can be stiffer than steel, softer than a feather, literally as flexible as rubber, as durable as rock, as colorful as a rainbow, and so much more.

all-important monomer interactions which, after all, essentially shape all polymer properties manifested at various scales. It is in this context that this dissertation formulates the inverse potential problem and points out possible solutions to it.

The work on the inverse potential problem is presented in this dissertation according to the following structure. First, a comprehensive introduction to the concepts of field-theoretic simulations is given in Chapter 2. In addition to an overview of important work in the field, monomer interactions are classified systematically for the first time and the current limitations of the framework are highlighted. An already established method of extending the monomer interactions is the introduction of smeared microscopic density fields. Chapter 3 summarizes this method and takes it to the higher level of more general potentials. Since the replacement of the underlying microscopic density fields is potentially a major interference in the particle-to-field transformation and thus in the resulting field-theoretic model itself, the two subsequent chapters deal with alternative concepts, developed in this work, and are directly devoted to the inverse potential, u^{-1}. In Chapter 4, it is shown how inverse potentials can be derived in an interplay with external methods and this is demonstrated by the example of the Morse potential, widely known from particle-based simulations. Chapter 5 then deals with the direct calculation of inverse potentials in general and demonstrates this also on the Morse potential. Finally, in Chapter 6 all important concepts are briefly summarized and an outlook on the possible applications of these new findings is given.

2

FIELD-THEORETIC SIMULATIONS: A POWERFUL TOOL – WITH RESTRICTIONS

I suppose it is tempting, if the only tool you have is a hammer, to treat everything as if it were a nail.
— Abraham Maslow

There is no universal simulation tool. Depending on which properties and questions are in focus, considerations are associated with certain length and time scales. Engineers who optimize the rotor shapes of wind turbines, for example, are most likely less interested in a quantum mechanical description of the air molecules, which would not be computationally feasible anyway. Even on smaller length scales, such as for the computer-based study of mesoscopic polymer properties, the description of all individual atoms is usually not possible due to long equilibration times of the chains, for instance, and coarser models are needed. Thus, for the length and time scales shown in Fig. 2.1, a diverse set of simulation tools and methods have been developed to meet the broad range of requirements. As with Maslow's hammer, moreover, depending on the problem, tools that are suitable and less suitable are available, even if computing power is not the limiting factor.

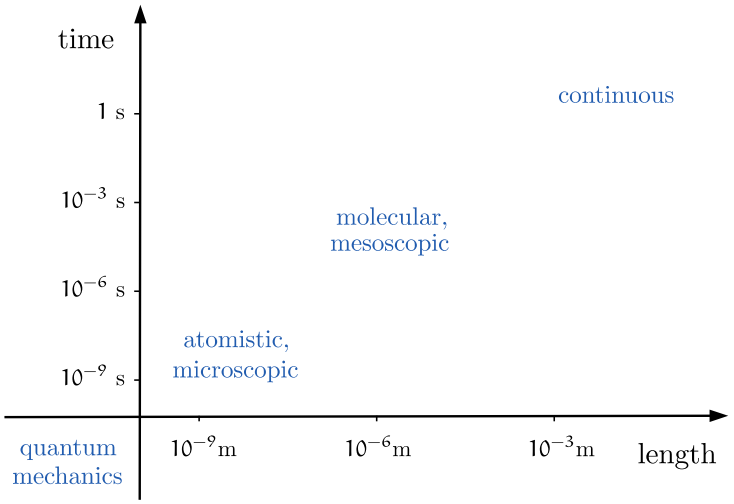

FIGURE 2.1: Levels of description with characteristic length and time scales.

As can be seen in Fig. 2.1, quantum mechanics simulations are used at the smallest length scales at the level of the Schrödinger equation. Here, for example, use is made of the Hartree–Fock method or the Møller–Plesset perturbation theory [9], which is computationally feasible only for small systems (a few molecules). To be able to simulate larger systems, the electronic motions are neglected on the atomistic level and instead classical particles with classical potentials or

force fields are used [10]. Molecular dynamics (MD) and Monte Carlo (MC) simulations have proven to be particularly useful methods for the study of polymeric liquids [11]. When moving to larger scales at the mesoscopic level, the demanding process of coarse-graining attempts to further reduce degrees of freedom while maintaining desired (structural) properties [12]. Depending on the degree of resolution, united atom or coarser bead-based models are common [13]. To account for hydrodynamic effects, the dissipative particle dynamics (DPD) method is also available at this level [14–17], which is still under constant development, such as through work on energy conserving coarse-graining algorithms [18]. It is this mesoscopic level as well where classical field-based methods, such as classical density functional theory (DFT) of simple liquids [19] and polymer fluids [20], are applied using variational principles. On the largest length scale, the continuous level, molecular structures are finally neglected and computational fluid dynamics (CFD) or the finite element method (FEM) are typically applied [21].

After this short overview of common simulation methods on different length scales, the additional utility of another framework may seem questionable at first. What unites most of the methods listed above is that they belong to the category of "computer experiments" described in the introduction, which also has its own problems. Especially for polymeric systems, long relaxation times, for example, render the equilibration process in MD simulations difficult or, on the other hand, the dense nature of these systems makes Monte Carlo moves challenging. With classical DFT, a method apart from computer experiments, these typical methodological problems are efficiently circumvented and a quite powerful tool for the study of mesoscopic systems is already available. What makes the situation very unfortunate, however, is the inevitable need for approximations in model building with excess free energy functionals of classical DFT. It is at this point that the advantages of field-theoretic simulations become apparent: while being a physically well-founded framework, they circumvent the typical problems of particle-based computer experiments, at the same time providing approximation-free transformations of underlying particle-based models. The intention of this chapter is to outline this beauty and elegance of the framework, but also to show limitations in a critical view.

2.1 INTRODUCTION TO FIELD-THEORETIC SIMULATIONS

First of all, the use of the term "field-theoretic simulations" in the scope of this dissertation shall be addressed. This seems necessary because by now several (confusingly similar) statistical field theories have emerged that refer to the field-theoretic context and thus have led to this ambiguity. All these related theories can build on the same level of a particle-based model, but differ fundamentally in their transformation mechanisms in the derivation of their statistical field theory. In the collective variable (CV) method (see for example [22, 23] and references therein), a so-called delta functional transform is applied to the microscopic density of the particles to derive a statistical field theory. Since a collective density field is thereby introduced into the model, this shall be called the density-explicit formalism. A major advantage of this theory is the fact that the pair potential function need not be invertible and that multi-body interactions (beyond pair interactions) can in principle be modeled. Nevertheless, due to massive problems caused by numerical instabilities, no results of the complete density-explicit field theory have been published yet [24] and the initial enthusiasm seems to have faded. Another area in this field is the coherent states (CS) theory, which in this realization is attributed to work by S. F. Edwards and K. F. Freed [25–27], that has recently been revived [28]. The method allows in principle to formulate models using likewise non-invertible pair potentials with more complicated chain geometries into a field theory. However, statistical sampling has proven to be quite challenging in these new simulations and has turned out to be computationally demanding even for simple models. The third theory in this series is the auxiliary field (AF) theory, which was extensively pioneered in this context by S. F. Edwards [29, 30]. Since its early development, this theory has become (by far) one of the most successful cornerstones of field-theoretic simulations without which its many successes, discussed below, would be difficult to envision. In the original sense, therefore, the term field-theoretic simulations is associated with the AF theory, and so it will be in this dissertation.

Ever since the first presentation of FTS concepts in the early 2000s [8, 31, 32], the framework has followed an impressive path of development. Especially in the equilibrium study of mesoscopic polymer structures, field-theoretic simulations have grown to be an extremely powerful tool [33, 34]. A prime example of a system that has been extensively studied on the basis of field-theoretic models are block copolymer melts [35–37]. Also, their (directed) self-assembly [38–40] or template-guided self-assembly and pattern formation [41, 42] is the subject of current research. In combination with homopolymers, for instance, microemulsions of polymer blends [43, 44] have been considered. Another category of field-theoretic simulations includes the study of complex coacervates [45–48], in which the formation of particular structural properties by separation of individual components of charged polymer systems (namely polyelectrolytes) is investigated. Thematically related studies (in the field of electrostatics) also include

the simulation of polymers in electric fields [49, 50]. Apart from linear chains, the study of more complicated molecular architectures is also possible in the FTS framework. An example of this is the work on so-called bottlebrush polymers [51, 52]; these are polymers with side chains grafted to the backbone altering the material properties. Based on field-theoretic principles, studies of a wide variety of hybrid models have been conducted. The closest to the original statistical field theory is the so-called hybrid particle field (HPF) theory [53], in which the field transformation is not applied to all particles. The derived models thus include degrees of freedom of (a few individual) particles in addition to the continuous fields. Studies of polymer nanocomposites, for example [54, 55], have been carried out in this way, which can be advantageous even if a purely field-theoretic description [56] is possible. Slightly further from this, other hybrid field theories include modeling a single chain in mean field to study the morphology of multi-component polymer systems [57, 58] or hybrid models to dynamically study defects in lamellar diblock copolymers [59]. From a physicist's point of view, field-theoretic work on the calculation of free energies for classical fluids and polymers [60] is of interest as well. Even seemingly exotic topics such as liquid-crystalline foods [61] which, however, find applications in food science and technology have already been thematically covered with FTS. Finally (and naturally), the influence of ever evolving technological trends on FTS research can be observed, such as its implementation on graphics cards [62] or its combination with deep learning [63].

Following this broad overview, the next section will provide a more in-depth (and admittedly more technical but vitally important) understanding of the FTS building blocks down to the level of their mathematical description.

2.2 BUILDING BLOCKS OF AN FTS MODEL

Arguably, one of the most convincing arguments in favor of the FTS framework is its construction on the rock-solid foundation of statistical mechanics. As a simple example to begin with, this will be demonstrated using a monatomic fluid.[1] For this, we consider n particles confined in a (three-dimensional) volume V at a temperature T. In contrast to an ideal gas, the particles interact with each other by a pair potential u as schematically shown in Fig. 2.2. The potential energy U of this system is thus simply the sum of the contributions from the individual pair interactions:

$$U = \frac{1}{2}\sum_{i=1}^{n}\sum_{j=1}^{n} u(\boldsymbol{r}_i - \boldsymbol{r}_j) - \frac{n}{2}u(\boldsymbol{0}). \tag{2.1}$$

1 This standard introductory example of a monatomic fluid is also chosen in relevant FTS literature [64]. The presentation given here, however, is intended to follow a slightly adjusted path by focusing on the calculation of field-based observables rather than to demonstrate the derivation of a field-theoretic Hamiltonian.

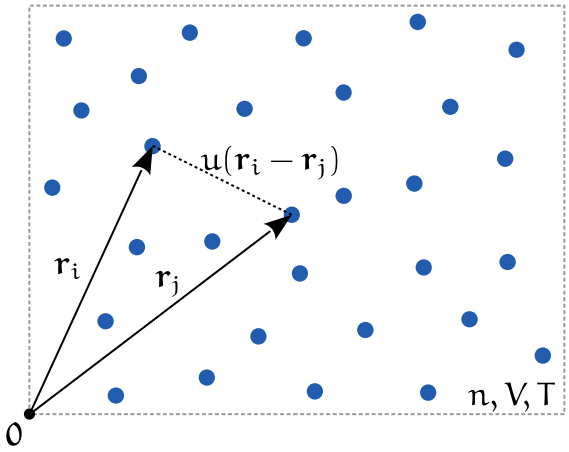

FIGURE 2.2: 2D schematic illustration of the monatomic fluid model in the canonical ensemble.

Here, each pair interaction between the particles with spatial positions $\boldsymbol{r}_i$ and $\boldsymbol{r}_j$ is counted only once (factor $\frac{1}{2}$) and the self-interaction $u(\mathbf{0})$ is excluded. As an alternative to Eq. (2.1), the microscopic density

$$\hat{\rho}(\boldsymbol{r}) = \sum_{i=1}^{n} \delta(\boldsymbol{r} - \boldsymbol{r}_i) \tag{2.2}$$

can be introduced to express the potential energy as a functional (a function of a function) of it as

$$U = \frac{1}{2} \int_V \mathrm{d}^3 r \int_V \mathrm{d}^3 r' \; \hat{\rho}(\boldsymbol{r}) u(\boldsymbol{r} - \boldsymbol{r}') \hat{\rho}(\boldsymbol{r}') - \frac{n}{2} u(\mathbf{0}) \tag{2.3}$$

$$=: \frac{1}{2} \langle \hat{\rho} | u | \hat{\rho} \rangle - \frac{n}{2} u(\mathbf{0}). \tag{2.4}$$

Based on generally known principles of statistical mechanics, statistical averages (ensemble averages) of physical observables of interest can then be derived from an adjusted partition function containing U. For our case of the monatomic fluid in the (n, V, T) (or canonical) ensemble, the ensemble average of a general spatially dependent scalar observable $A(\boldsymbol{r})$ (such as the density) can be obtained by introducing a so-called source field $J(\boldsymbol{r})$ in the adjusted canonical partition function

$$\mathcal{Z}_c[J] = z_0 \int_{V^n} \mathrm{d}^{3n} r \; \exp\left(-\beta U - \langle J | A \rangle\right). \tag{2.5}$$

$\beta = (k_B T)^{-1}$ is introduced here as the thermodynamic beta and the the prefactor z_0 contains, inter alia, the out-integrated translational part and shall not be of further interest here. Moreover, it is easy to verify that for a vanishing source field J the canonical partition

function $\mathcal{Z}_c$ is recovered. From Eq. (2.5), the ensemble average $\langle A(\boldsymbol{r})\rangle$ can then be calculated as

$$\langle A(\boldsymbol{r})\rangle = \frac{\int_{V^n} \mathrm{d}^{3n}r\ A(\boldsymbol{r}) \exp\left(-\beta U\right)}{\int_{V^n} \mathrm{d}^{3n}r\ \exp\left(-\beta U\right)} \tag{2.6}$$

$$= -\frac{\delta}{\delta J(\boldsymbol{r})} \ln \mathcal{Z}_c[J]\bigg|_{J=0}. \tag{2.7}$$

The derivative in Eq. (2.7) denotes the functional derivative with respect to $J(\boldsymbol{r})$, in Eq. (2.6) the apparent general dependence of the observable A on the particle positions has been omitted for the sake of clarity. What makes the practical calculation of general observables in this form difficult, however, is solving the high-dimensional coupled integrals, which is impossible to do analytically for systems of practical interest. In particle-based simulations, therefore, this ensemble average is approximated by mean values of configuration-derived observables, where the update of particle configurations is then subject to fundamentally different concepts depending on the method.[2] Field-theoretic simulations start at the point of Eq. (2.7) and offer as a statistical field theory another way to evaluate physical observables. This will be demonstrated next using the density observable as an example.

At the heart of the field-theoretic framework is the particle-to-field transformation, a Gaussian integral identity, which is also called the Hubbard–Stratonovich (HS) transformation [65, 66] and is further associated with the names Edwards [67], Kac [68], and Siegert [69]. A derivation of the transformation is sketched in Appendix A.1 starting from a conventional d-dimensional Gaussian integral and it can be given by

$$\exp\left(-\frac{\beta}{2}\langle\hat{\rho}|u|\hat{\rho}\rangle\right) = \frac{\int \mathcal{D}w\ \exp\left(-\frac{1}{2\beta}\langle w|u^{-1}|w\rangle - i\langle w|\hat{\rho}\rangle\right)}{\int \mathcal{D}w\ \exp\left(-\frac{1}{2\beta}\langle w|u^{-1}|w\rangle\right)}. \tag{2.8}$$

It is important to note that according to the derivation in Appendix A.1, u must be a positive-definite function. For continuous, integrable functions, this is equivalent to demanding their (radial) Fourier transform to be positive [70]. The Gaussian integral identity of Eq. (2.8) can then be used to calculate, for example, the ensemble average $\langle\hat{\rho}(\boldsymbol{r})\rangle$ according to Eq. (2.7) by a field-based description alternative to the integrals over the particle coordinates. For this purpose, the source field J conjugate to the density is introduced and the modified canonical partition function from Eq. (2.5) is written out for the monatomic fluid as

$$\mathcal{Z}_c[J] = z_0 \exp\left(\frac{1}{2}\beta n u(0)\right) \int_{V^n} \mathrm{d}^{3n}r\ \exp\left(-\frac{\beta}{2}\langle\hat{\rho}|u|\hat{\rho}\rangle - \langle J|\hat{\rho}\rangle\right). \tag{2.9}$$

2 Monte Carlo simulations can be interpreted in the broadest sense as importance sampling of the integrals from Eq. (2.6), in molecular dynamics simulations the ergodic hypothesis is exploited to approximate ensemble averages by time averages.

Then, the Gaussian integral identity from Eq. (2.8) is used to introduce the auxiliary field w where the denominator from Eq. (2.8) is considered here together with the self-interactions in a new prefactor z_0':

$$\mathcal{Z}_c[J] = z_0' \int_{V^n} \mathrm{d}^{3n}r \int \mathcal{D}w \, \exp\left(-\frac{1}{2\beta}\left\langle w\middle|u^{-1}\middle|w\right\rangle - i\left\langle w|\hat{\rho}\right\rangle - \left\langle J|\hat{\rho}\right\rangle\right). \tag{2.10}$$

In this important step, the inverse potential u^{-1} was introduced and the complexities involved with coupled particle-particle interactions through the pair potential u are avoided by bringing in the analysis of local particle-field interactions. This allows one now to calculate the integrals over the particle coordinates individually. Inserting the microscopic density of Eq. (2.2) into the remaining terms and identifying the same factors of integrals leads to

$$\begin{aligned}\mathcal{Z}_c[J] = z_0' \int \mathcal{D}w \, \exp\left(-\frac{1}{2\beta}\left\langle w\middle|u^{-1}\middle|w\right\rangle\right) \\ \times \left(\int_V \mathrm{d}^3r \, \exp\left(-\left(iw(\boldsymbol{r}) + J(\boldsymbol{r})\right)\right)\right)^n.\end{aligned} \tag{2.11}$$

As can be seen, the last term completely includes the remaining integration over the particle coordinates of the original partition function. It is therefore natural to introduce the (dimensionless) reduced partition function, in this case that of a single particle, as

$$Q[iw + J] := \frac{1}{V}\int_V \mathrm{d}^3r \, \exp\left(-\left(iw(\boldsymbol{r}) + J(\boldsymbol{r})\right)\right). \tag{2.12}$$

The use of Eq. (2.12) and the absorption of the term V^n in a new prefactor z_0'' then allows the adjusted canonical partition function to be written as

$$\mathcal{Z}_c[J] = z_0'' \int \mathcal{D}w \, \exp\left(-\frac{1}{2\beta}\left\langle w\middle|u^{-1}\middle|w\right\rangle + n\ln Q[iw + J]\right). \tag{2.13}$$

The fact that the new prefactor z_0'' is now volume-dependent is important to consider in derivations involving volume derivatives such as, for example, in the calculation of the pressure. Having arrived at the point of a complete field-based description, the ensemble average of the density can now be calculated according to Eq. (2.7) as

$$\left\langle\hat{\rho}(\boldsymbol{r})\right\rangle = \frac{-\frac{\delta}{\delta J(\boldsymbol{r})}\int \mathcal{D}w \, \exp\left(-\frac{1}{2\beta}\left\langle w\middle|u^{-1}\middle|w\right\rangle + n\ln Q[iw + J]\right)\Big|_{J=0}}{\int \mathcal{D}w \, \exp\left(-\frac{1}{2\beta}\left\langle w\middle|u^{-1}\middle|w\right\rangle + n\ln Q[iw]\right)}. \tag{2.14}$$

Moving the functional derivative into the integral combined with the subsequent application of the chain rule yields

$$\left\langle\hat{\rho}(\boldsymbol{r})\right\rangle = \frac{\int \mathcal{D}w \left(-n\frac{\delta \ln Q[iw+J]}{\delta J(\boldsymbol{r})}\Big|_{J=0}\right) \exp\left(-\frac{1}{2\beta}\left\langle w\middle|u^{-1}\middle|w\right\rangle + n\ln Q[iw]\right)}{\int \mathcal{D}w \, \exp\left(-\frac{1}{2\beta}\left\langle w\middle|u^{-1}\middle|w\right\rangle + n\ln Q[iw]\right)}. \tag{2.15}$$

What follows from here is a special concept of the field-theoretic framework, that of *field-based* observables, also called operators [64] following concepts of quantum physics in the broadest sense. The underlying idea goes back to the similarity between Eqs. (2.15) and (2.6). In this comparison, it seems natural, first, to define the calculation of the ensemble average of a field-based observable[3] $\tilde{A}(\boldsymbol{r})$ by

$$\left\langle \tilde{A}(\boldsymbol{r}) \right\rangle_w := \frac{\int \mathcal{D}w \; \tilde{A}(\boldsymbol{r}) \exp\left(-\frac{1}{2\beta}\left\langle w \middle| u^{-1} \middle| w \right\rangle + n \ln Q[iw]\right)}{\int \mathcal{D}w \; \exp\left(-\frac{1}{2\beta}\left\langle w \middle| u^{-1} \middle| w \right\rangle + n \ln Q[iw]\right)} \tag{2.16}$$

and, second, to identify the field-based density observable, or more concisely the *density field observable*, as

$$\tilde{\rho}(\boldsymbol{r}) = -n \frac{\delta \ln Q[iw + J]}{\delta J(\boldsymbol{r})}\bigg|_{J=0} \tag{2.17}$$

such that

$$\langle \hat{\rho}(\boldsymbol{r}) \rangle = \langle \tilde{\rho}(\boldsymbol{r}) \rangle_w \,. \tag{2.18}$$

Here it has been established for reasons of clarity to often omit the subscript consisting of the auxiliary fields of the field-based observable. Eventually, after substituting the reduced partition function from Eq. (2.12), the functional derivative in Eq. (2.17) can be calculated to obtain the density field observable for the monatomic fluid:

$$\tilde{\rho}(\boldsymbol{r}) = \rho_0 \, \exp\left(-iw(\boldsymbol{r}) - \ln Q[iw]\right), \tag{2.19}$$

with $\rho_0 = \frac{n}{V}$ being the bulk fluid density.

It is only after discussing the particle-to-field transformation inclusive of the particle-based observable (leading to Eq. (2.15)) and the newly motivated field-based calculation of the ensemble averages (analogy of Eqs. (2.6) and (2.16)) that the widely used foreshortened model derivation (the direct transformation of $\mathcal{Z}_c$) appears comprehensible.[4] In this foreshortened derivation, $\mathcal{Z}_c$ (corresponding to $\mathcal{Z}_c[J = 0]$ from Eq. (2.5)) is transformed and brought to the form

$$\mathcal{Z}_c \propto \int \mathcal{D}w \; \exp\left(-\mathcal{H}[w]\right). \tag{2.20}$$

The introduced functional $\mathcal{H}[w]$ is called effective Hamiltonian [64] (or field-theoretic Hamiltonian) and can be found, by construction, in the exponential functions of Eq. (2.15) as

$$\mathcal{H}[w] = \frac{1}{2\beta}\left\langle w \middle| u^{-1} \middle| w \right\rangle - n \ln Q[iw]. \tag{2.21}$$

3 Field-based observables evidently have a functional dependence on the auxiliary fields. For clarity, this is not explicitly written out for the field observables to be identified by a tilde.

4 I would like to thank Hans Christian for his insistent comments on this in the beginning of my doctorate.

It should be recalled that the computation of the *value* of $\mathcal{Z}_c$, as Eq. (2.20) misleadingly suggests, is generally not important, whereas the field-theoretic model, however, is defined by the functional form of $\mathcal{Z}_c$ specified by $\mathcal{H}$ from Eq. (2.21).

To gain a better intuition for this building block $\mathcal{H}$ of a field-theoretic model, an additional term accounting for monomer or segment connectivity shall now be introduced as an extension to the monatomic fluid model to a simple bead-spring (BS) model, so that chain-like molecules can be described. For this purpose, the same n particles of the monatomic fluid are grouped into n_c chains, each consisting of n_m monomer particles, and the microscopic density is written (equivalently) as a double sum:

$$\hat{\rho}(\boldsymbol{r}) = \sum_{i=1}^{n_c} \sum_{j=1}^{n_m} \delta(\boldsymbol{r} - \boldsymbol{r}_{i,j}). \tag{2.22}$$

The potential energy U from Eq. (2.4) is then extended by a term containing the connectivity in form of a general bond potential h, which might be, for example, a simple harmonic potential acting between adjacent monomers of a chain:

$$U^{(\mathrm{BS})} = \frac{1}{2} \langle \hat{\rho} | u | \hat{\rho} \rangle - \frac{n_c n_m}{2} u(\boldsymbol{0}) + \sum_{i=1}^{n_c} \sum_{j=1}^{n_m - 1} h(\boldsymbol{r}_{i,j} - \boldsymbol{r}_{i,j+1}). \tag{2.23}$$

This simple extension now encompasses all the necessary changes to the particle-based description, which is schematically illustrated in Fig. 2.3. The derivation of the new field-theoretic Hamiltonian from

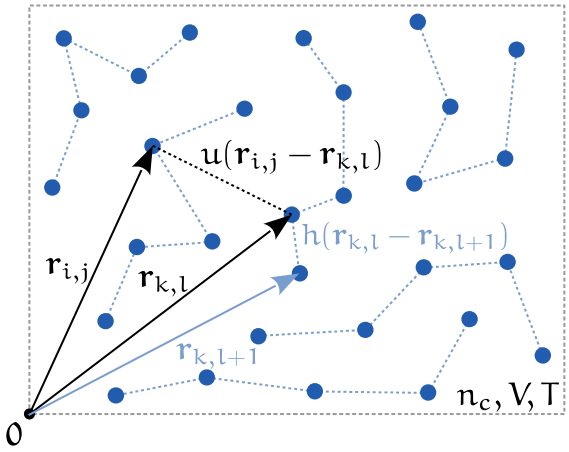

FIGURE 2.3: 2D schematic illustration of a bead-spring model consisting of n_c chains in the canonical ensemble.

this particle-based level can then be done in the shorter way by direct transforming the partition function $\mathcal{Z}_c[J = 0]$. Again, the application of the HS transformation decouples the non-bonded interactions of the particles. However, the newly introduced bonded interaction term leads to a coupling of some individual volume integrals, even if the

identical integrals over the n_c single chain molecules are decoupled similarly to Eq. (2.11):

$$\mathcal{Z}_c^{(\mathrm{BS})} = z_0' \int \mathcal{D}w \, \exp\left(-\frac{1}{2\beta}\left\langle w\middle|u^{-1}\middle|w\right\rangle\right) \times \left(\int_{V^{n_m}} \mathrm{d}^{3n_m}r \, \exp\left(-\sum_{j=1}^{n_m} iw(\boldsymbol{r}_j) - \beta\sum_{j=1}^{n_m-1} h(\boldsymbol{r}_j - \boldsymbol{r}_{j+1})\right)\right)^{n_c}. \tag{2.24}$$

The n_m volume integrals from Eq. (2.24) can then be solved recursively one after the other which will be shown in detail next.

With the intention of reintroducing a dimensionless reduced partition function, as was done for the monatomic fluid, it is common (and proper) in field-theoretic modeling to normalize the volume integrals from Eq. (2.24) with its field-free equivalent [64], effectively assigning the (constant) normalization factor to a substitution of z_0'. Following reference [64], we introduce the reduced partition function as

$$Q^{(\mathrm{BS})}[iw] := \frac{\int_{V^{n_m}} \mathrm{d}^{3n_m}r \, \exp\left(-\sum_{j=1}^{n_m} iw(\boldsymbol{r}_j) - \beta\sum_{j=1}^{n_m-1} h(\boldsymbol{r}_j - \boldsymbol{r}_{j+1})\right)}{V\left(\int_V \mathrm{d}^3b \, \exp\left(-\beta h(\boldsymbol{b})\right)\right)^{n_m-1}}, \tag{2.25}$$

with $\boldsymbol{b}$ being the bond vector. This suggests introducing a term called the normalized bond transition probability as

$$\Phi(\boldsymbol{r}) = \frac{\exp\left(-\beta h(\boldsymbol{r})\right)}{\int_V \mathrm{d}^3r \, \exp\left(-\beta h(\boldsymbol{r})\right)} \tag{2.26}$$

to write the n_m volume integrals from Eq. (2.25) as

$$Q^{(\mathrm{BS})}[iw] = \frac{1}{V}\int_{V^{n_m}} \mathrm{d}^{3n_m}r \, \exp(-iw(\boldsymbol{r}_1))\Phi(\boldsymbol{r}_1 - \boldsymbol{r}_2)\exp(-iw(\boldsymbol{r}_2)) \ldots \times \ldots \exp(-iw(\boldsymbol{r}_{n_m-1}))\Phi(\boldsymbol{r}_{n_m-1} - \boldsymbol{r}_{n_m})\exp(-iw(\boldsymbol{r}_{n_m})). \tag{2.27}$$

For the solution of Eq. (2.27), it is useful to enclose the directly coupled parts in a function for solving the integrals recursively. This recursive function can then be defined as

$$q(\boldsymbol{r}, j+1) = \exp(-iw(\boldsymbol{r}))\int_V \mathrm{d}^3r' \, \Phi(\boldsymbol{r} - \boldsymbol{r}') \, q(\boldsymbol{r}', j) \tag{2.28}$$

with the first element (typically denoted by index $j = 0$)

$$q(\boldsymbol{r}, 0) = \exp(-iw(\boldsymbol{r})). \tag{2.29}$$

A more careful inspection of Eq. (2.28) reveals the form of the Chapman–Kolmogorov equation (CKE): q can be identified as a statistical weight propagated along the chain through the normalized bond transition probability Φ and is accordingly called the chain propagator. The reduced partition function is subsequently calculated from this by

$$Q^{(\mathrm{BS})}[iw] = \frac{1}{V}\int_V \mathrm{d}^3r \, q(\boldsymbol{r}, n_m - 1). \tag{2.30}$$

After this short excursion into the concepts of chain propagators in the spirit of reference [64], the field-theoretic modeling of the bead-spring model can be finalized. Substituting the newly introduced reduced partition function (Eq. (2.25)) into the canonical partition function (Eq. (2.24)) and renormalizing the prefactor, the following field-theoretic Hamiltonian can be identified by comparison with Eq. (2.20):

$$\mathcal{H}^{(\mathrm{BS})}[w] = \frac{1}{2\beta} \left\langle w \middle| u^{-1} \middle| w \right\rangle - n_c \ln Q^{(\mathrm{BS})}[iw]. \tag{2.31}$$

The evident similarity of this field-theoretic Hamiltonian to that of the monatomic fluid (Eq. (2.21)) is striking but not coincidental. As can be seen, the introduced connectivity in the form of bonded interactions leads to an effective reduced number of individual particle constructs[5] (i.e. atoms or their assembly into molecules) from $n = n_c n_m$ to n_c. As a consequence, the reduced partition function of the latter case, $Q^{(\mathrm{BS})}$, contains the connectivity of the n_m particles (and thus the information about the molecular architecture) and, in view of its calculation by Eqs. (2.28)-(2.30) using a chain propagator, exhibits a much higher complexity than that of the monatomic fluid. Since the bead-spring model as well as the monatomic fluid model contains only one type of particles (i.e. only one microscopic density appearing in the particle-based model), also only one HS transformation is performed which introduces one auxiliary field. Therefore, it is plausible that the first term of the field-theoretic Hamiltonian (originating from the decoupling of the non-bonded pair interactions) is identical in both models. In general, each type of particle introduces an auxiliary field into the model and each unique particle construct (atom or molecule of different type) introduces its own reduced partition function.[6] In conclusion to this section, a schematic representation of the discussed building blocks of field-theoretic models is shown in Fig. 2.4.

5 This cumbersome auxiliary term seems necessary only because individual atoms are typically not referred to as molecules.

6 To apply the HS transformation in the case of multiple types of particles, it is necessary to linearly combine the microscopic densities. Details of this can be found in reference [71]. For an excellent presentation of a variety of other field-theoretic models, including continuous chains as a limiting case of the bead-spring model, the reader is referred to reference [64].

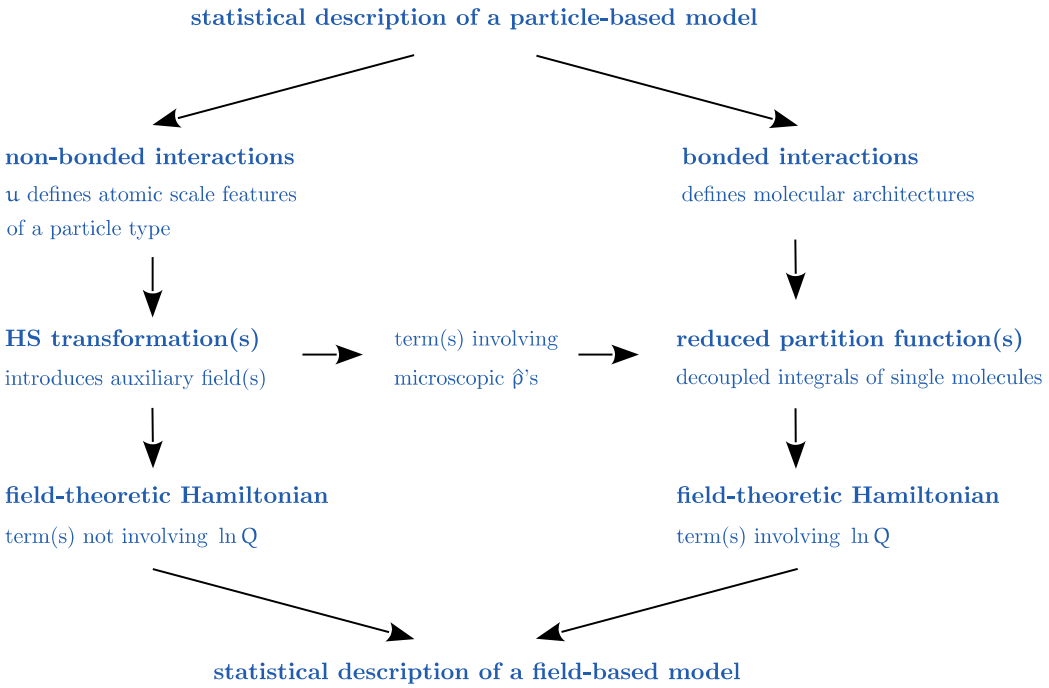

FIGURE 2.4: Schematic representation of common building blocks of field-theoretic models.

2.3 FTS MODELS IN OPERATION

Having provided a sufficient understanding of field-theoretic modeling, the next step is to move on to the practical operation of these models. More specifically, it is not enough to derive sophisticated functionals of continuous fields and field-based observables; rather, for the full implementation of field-theoretic simulations to computationally study polymers and soft matter, the practical calculation and evaluation of the field-theoretic observables is equally essential. With this primary goal of observable computation in mind, the question of how to compute the associated functional integrals of the auxiliary fields (Eq. (2.16)) goes hand in hand.

A serious problem that the field transformation entails is related to the generally complex-valued field-theoretic Hamiltonian $\mathcal{H}$ appearing in the exponents of Eq. (2.16). This equation can be rewritten into the form

$$\left\langle \tilde{A}(\boldsymbol{r}) \right\rangle_w = \int \mathcal{D}w \; \tilde{A}(\boldsymbol{r}) P_c[w], \tag{2.32}$$

so that the complex-valued nature of the statistical weight

$$P_c[w] := \frac{\exp\left(-\frac{1}{2\beta}\left\langle w \middle| u^{-1} \middle| w \right\rangle + n \ln Q[iw]\right)}{\int \mathcal{D}w \; \exp\left(-\frac{1}{2\beta}\left\langle w \middle| u^{-1} \middle| w \right\rangle + n \ln Q[iw]\right)} \tag{2.33}$$

becomes apparent. As a consequence of the complex-valued $\mathcal{H}$, the statistical weight P_c is not positive and instead oscillates strongly. This

so-called *sign problem*, which also occurs in the evaluation of path integrals in quantum models [72], renders the application of conventional Monte Carlo sampling methods seriously difficult [73].

One solution strategy is the approximation of the functional integrals by the extremum of their integrand. Approximating the integrals in this way lays the foundation for self-consistent field theory (SCFT), which was applied to polymer systems early on [74, 75]. In the context of SCFT [76], the extremum of the functional integral is found by a saddle-point configuration of the auxiliary fields and this is derived by solving self-consistent equations, which is the equivalent here to solving saddle-point equations. For instance, the models derived in the previous section are given by field-theoretic Hamiltonians that depend on only a single auxiliary field, w, and the saddle-point configuration w^* is then found by solving the saddle-point equation

$$\left.\frac{\delta\mathcal{H}[w]}{\delta w(\boldsymbol{r})}\right|_{w=w^*} = 0. \tag{2.34}$$

Numerically efficient solution methods of this type of equations are still the subject of current research; a comprehensive comparison was recently published in [77]. To take up the introductory example of the monatomic fluid again, the functional derivative of $\mathcal{H}$ from Eq. (2.21) with respect to $w(\boldsymbol{r})$ is calculated to obtain the following saddle-point equation:

$$\frac{1}{\beta}\left[u^{-1} * w^*\right](\boldsymbol{r}) + i\rho^*(\boldsymbol{r}) = 0, \tag{2.35}$$

with the large asterisk $*$ together with the square brackets denoting a convolution and

$$\rho^*(\boldsymbol{r}) := \tilde{\rho}(\boldsymbol{r})\Big|_{w=w^*} \tag{2.36}$$

being introduced as the saddle-point density. Having reached this point and freely following [64], several observations can be made about this so-called saddle-point approximation. First, the approximation of the functional integral by the extremum of its integrand implies $\mathcal{Z}_c \approx \mathcal{Z}_c^*$ where (up to a normalizing constant)

$$\mathcal{Z}_c^* \propto \exp\left(-\mathcal{H}[w^*]\right). \tag{2.37}$$

For physically meaningful saddle-point configurations, the imaginary part of the integrand should vanish, and $\mathcal{H}[w^*]$ is real. Second, this has the consequence that the solution w^* of the saddle-point equation (Eq. (2.34)) may be complex-valued and thus be located away from the original integration path along the real axis of the functional integral. Following [31], a purely imaginary saddle point as in the case of the monatomic fluid example is shown schematically in Fig. 2.5. In general, field-theoretic models can possess, depending on their level of complexity, multiple saddle points that can be assigned to pure states (such as lamellar or cylindrical), defect states, or mixed states and can be found in the literature ([64] and references therein). Third, in view

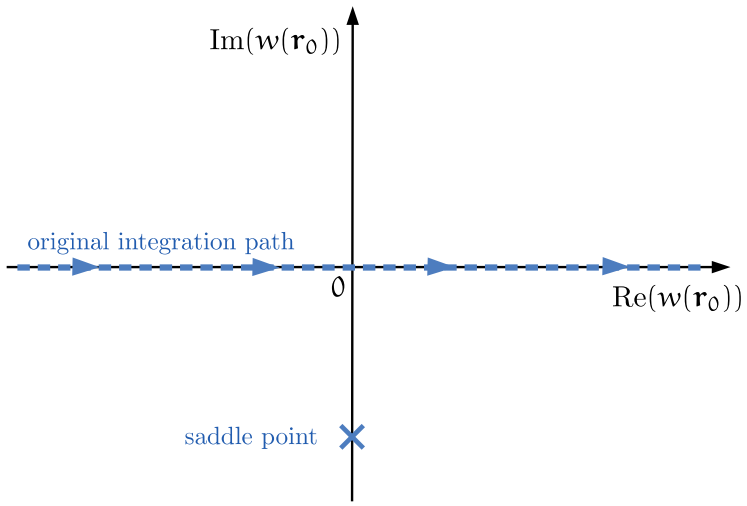

FIGURE 2.5: Original integration path of the auxiliary field w at a given point $\boldsymbol{r}_0$ in the calculation of the functional integral, and exemplary position of a saddle point next to the path.

of Eq. (2.36), and by now trivial, the ensemble average of field-based observables is also approximated using the saddle-point solution w^*:

$$\left\langle \tilde{A}(\boldsymbol{r}) \right\rangle_w \approx \tilde{A}(\boldsymbol{r})\Big|_{w=w^*}, \tag{2.38}$$

and in particular also

$$\langle \hat{\rho}(\boldsymbol{r}) \rangle \approx \rho^*(\boldsymbol{r}). \tag{2.39}$$

The obvious question to be asked at this point is under what circumstances such drastic approximations as Eq. (2.39) still give reasonably good results. If one notes that the approximation of all field contributions to the functional integral by a single, dominating field equally means that the microscopic components (individual particles or chains) contained in the reduced partition function Q are effectively exposed to their environment only through this single, dominating field, it is easy to understand that the application of the saddle-point approximation in its core means the transition to a mean-field theory. If one considers further that in the case of very dense systems the microscopic components are exposed to a large number of other components in their immediate environment, and thus there is effectively an averaging of the interactions occurring anyways, a good applicability of a mean-field description at high densities can be expected. If, on the other hand, dilute or semi-dilute systems are considered or the influence of an approaching order-disorder transition or that of a critical point cannot be neglected, severe inaccuracies of the mean-field theory should be assumed.[7] For the latter, other approaches for calculating the functional integrals have to be found. One of the most powerful and widely used approaches to this is a

7 A reflection beyond this intuitive understanding can be found, for example, in [76] and references therein.

special form of statistical sampling, the complex Langevin simulation technique, which will be briefly presented next.[8]

First of all, the main challenge, which is the handling of the sign problem, should be reminded. Here one can very imaginatively consider that the statistical weight $P_c[w]$, given by Eq. (2.33) for the models discussed here, exhibits a strongly oscillatory behavior over the original w integration path, shown in Fig. 2.5, which makes the numerical evaluation of ensemble averages of field-based observables (using an importance sampling scheme) problematic for this path. A mathematical consideration, however, will show that the specific choice of the integration path is (under certain conditions) not important when calculating the integral. For understanding, it shall be sufficient in the following to consider the one-dimensional case of conventional integrals.[9] Ensemble averages of observables then take the simple form

$$\left\langle \tilde{A} \right\rangle_w = \int_{\mathbb{R}} \mathrm{d}w \; \tilde{A}(w) P_c(w), \tag{2.40}$$

with the statistical weight

$$P_c(w) = \frac{\exp(-\mathcal{H}(w))}{\int_{\mathbb{R}} \mathrm{d}w \; \exp(-\mathcal{H}(w))}. \tag{2.41}$$

Cauchy's integral theorem can then be applied to introduce a deformed path γ in the complex plane which, together with the real axis, forms the closed contour of a simply connected domain such that

$$\int_{\mathbb{R}} \mathrm{d}w \; \tilde{A}(w) P_c(w) = \int_{\gamma} \mathrm{d}w \; \tilde{A}(w) P_c(w), \tag{2.42}$$

provided the integrand (in particular $\exp(-\mathcal{H}(w))$) is analytic and, considering the right hand side, now with $w \in \mathbb{C}$. An example of such a deformed path, which also passes through a saddle point, is shown in Fig. 2.6. With this possibility of path deformation, the challenge then is to find a suitable path with as minimal oscillations as possible in the integrand (i.e., constant complex phase of P_c) in order to numerically allow efficient importance sampling along this path. It can be shown [64] that steepest contour paths (i.e., locally of constant phase) which run through saddle points are particularly suitable for this purpose.[10] Practically, it is generally very difficult to find such paths a priori and a self-adaptive scheme would be more desirable. The complex Langevin (CL) equation [8], originally proposed

8 As with the introduction of FTS models in Section 2.2, it should be emphasized that complex Langevin sampling is a standard method discussed in relevant FTS literature [64]. As in the case of the FTS models, an intuitive understanding of the methodology is intended to be foremost and the presentation will therefore follow a slightly adjusted path.

9 The transition from common to functional integrals is given by the discretization of the auxiliary field according to Eq. (A.1.2).

10 A formal analysis on the issue of contour deformation through saddle points can be found in an applied mathematics text, such as in Ref. [78].

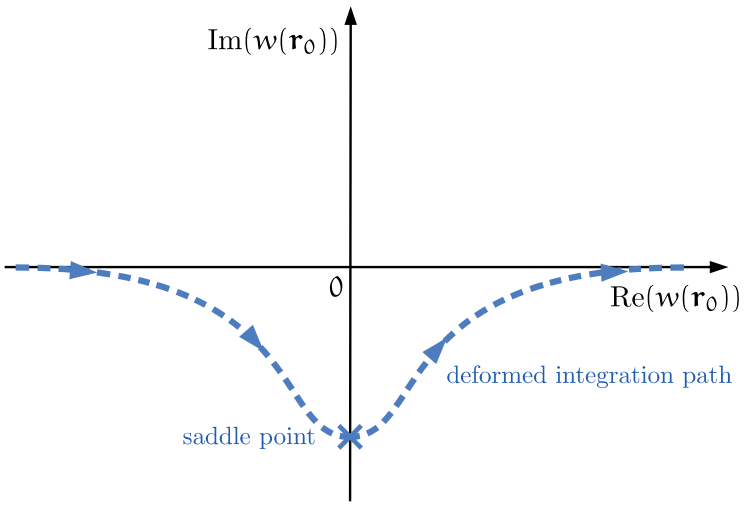

FIGURE 2.6: Deformed integration path of the auxiliary field w at a given point r_0 in the calculation of the functional integral, and exemplary position of a saddle point located on the path.

independently by Klauder [79] and Parisi [80] in a different context, should be viewed from this perspective:

$$\frac{\mathrm{d}}{\mathrm{d}t}w(t) = -\frac{\partial \mathcal{H}(w)}{\partial w(t)} + \eta(t), \tag{2.43}$$

with the fictitious time t, the now complex-valued auxiliary field w, and the purely real noise $\eta(t)$ fulfilling the time averages

$$\langle \eta(t) \rangle_t = 0, \tag{2.44}$$

$$\langle \eta(t)\eta(t') \rangle_t = 2\,\delta(t - t'). \tag{2.45}$$

The working principle of the complex Langevin equation can be easily understood based on the previous considerations. Without the noise, Eq. (2.43) takes the form of a so-called relaxation equation:[11]

$$\frac{\mathrm{d}}{\mathrm{d}t}w(t) = -\frac{\partial \mathcal{H}(w)}{\partial w(t)}, \tag{2.46}$$

where the field is relaxed in such a way that the right hand side vanishes. In this way the saddle-point equation is solved and the field is relaxed to a saddle-point configuration. Including the noise (which acts on the real part), only the imaginary part of the derivative, $\mathrm{Im}\left(\frac{\partial H(w)}{\partial w(t)}\right)$, is subject to relaxation. The vanishing of this derivative implies at the same time a relaxation towards a constant phase path. Along this path, a stochastic Brownian dynamics is driven by the noise term. Using the complex Langevin equation (Eq. (2.43)) and taking a detour through a hypothetical real and positive statistical

11 The term relaxation becomes meaningful when the time derivative is discretized and approximated by the forward Euler method. Under the condition that $\frac{\mathrm{d}^2\mathcal{H}(w)}{\mathrm{d}w^2} > 0$, this can then be transformed into a damped version of Newton's method. Consequently, the equation relaxes the field on the left hand side in such a way that the function of it on the right hand side vanishes.

weight [81], a complex Fokker–Planck equation for P_c can then be derived as was done in Ref. [64] as[12]

$$\frac{\partial P_c(w,t)}{\partial t} = \frac{\partial}{\partial w}\left(\frac{\partial}{\partial w} + \frac{\partial \mathcal{H}(w)}{\partial w}\right) P_c(w,t). \tag{2.47}$$

The stationary solution (relevant in practice) is given by $P_c(w) \propto \exp(-\mathcal{H}(w))$, the said stochastic Brownian dynamics along the constant phase path consequently samples configurations of the auxiliary field with the correct statistical weight. Although it appears not to be important in practice [64], it should nevertheless be pointed out that convergence to the steady state solution of the complex Langevin scheme is not guaranteed. Conditions under which the method can be trusted are discussed in detail in references [82, 83]. As for the numerical solution of the complex Langevin equation, a variety of integrator algorithms have been developed, some of which are presented in detail in reference [71].

In conclusion to this part, the operation of a complex Langevin simulation will be visualized by means of a schematic model that is compatible with the discussion above. Here, the analogue of the bead-spring model discussed in Sec. 2.2 will serve as an example. To begin with, the reduced partition function can be calculated analytically as

$$Q(iw) = \exp\left(-in_m w\right). \tag{2.48}$$

With the contact potential

$$u(r) = u_0\,\delta(r), \tag{2.49}$$

the field-theoretic Hamiltonian is given by

$$\mathcal{H}(w) = \frac{w^2 V}{2\beta u_0} + in_c n_m w. \tag{2.50}$$

Using the derivative

$$\frac{\partial \mathcal{H}(w)}{\partial w} = \frac{wV}{\beta u_0} + in_c n_m, \tag{2.51}$$

the saddle-point configuration can be calculated as

$$w^* = -i\frac{n_c n_m \beta u_0}{V}. \tag{2.52}$$

The real part of the complex weight, $\mathrm{Re}(\exp(-\mathcal{H}(w)))$, and the points sampled by the complex Langevin scheme are shown from two different perspectives in Fig. 2.7. The strong oscillations along the origi-

12 Using the argument of the deformability of the path and assuming that $P_c(w)$ is an analytic function, it is easy to see by comparing the two Fokker-Planck equations in Ref. [64] for these statistical weights that the hypothetical real statistical weight, P, corresponds exactly to a parametrization of P_c along a constant phase path ($P(w,t) = \mathrm{Re}(P_c(w,t))$ for $w \in \mathbb{C}$ under the condition that $\mathrm{Im}(P_c(w,t)) = \text{const.}$). The search for this hypothetical weight can thus also be interpreted as a search for deformed constant phase paths which, according to Cauchy's integral theorem, form a (vanishing) closed path integral together with the real axis.

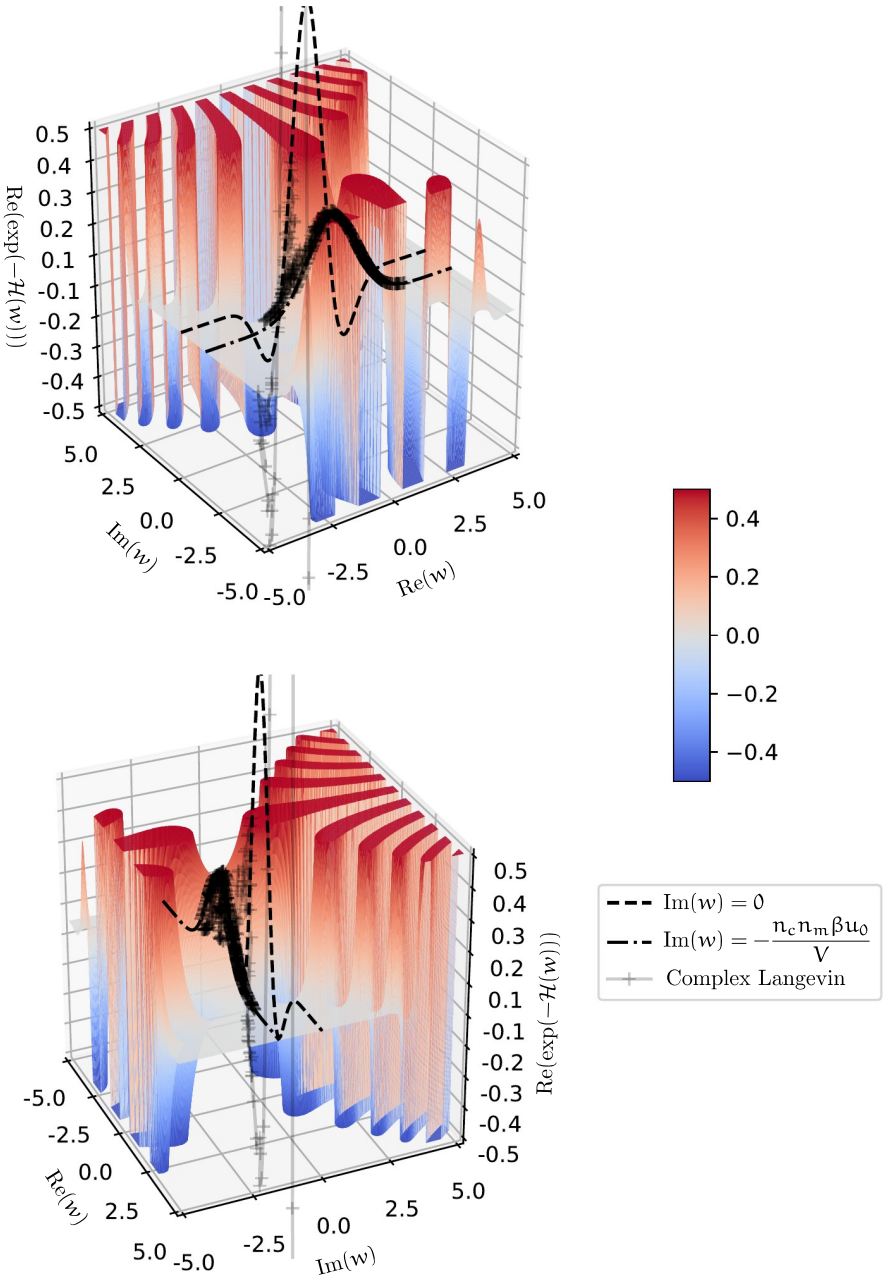

FIGURE 2.7: Real part of $\exp(-\mathcal{H}(w))$ plotted from two different perspectives. Two integration paths are shown: The original integration path along the real axis and a shifted parallel path through the saddle point. The saddle point is located at $w^* = -1.5i$ with $n_m = 1.5$ and all other model parameters set to one.

nal integration path are immediately obvious. For this simple model, the parallel path drawn through the saddle point is a constant phase path. As can be seen nicely, the complex Langevin scheme finds this path starting from a random initial point. The said stochastic Brownian dynamics along this path is driven by the noise. In this sense, furthermore, sampling of field configurations along this path can be recognized as a type of importance sampling.

2.4 THE INVERSE POTENTIAL PROBLEM – A SEVERE LIMITATION TO FTS

Following an introductory broad overview of important work on field-theoretic simulations in Section 2.1, this chapter has focused primarily on providing a solid and intuitive understanding of the methodological concepts of FTS. With this in mind, Section 2.2 reviewed in detail how a statistical particle-based model can be used to construct an approximation-free description by continuous fields. Given this overview of the important components of a field-theoretic model, the practical operation was subsequently outlined in Section 2.3 by means of the saddle-point approximation (leading to SCFT) as well as the complex Langevin method (leading to fully fluctuating field models). Up to this point, already existing basics have been recapitulated to a large extent, albeit the way of presentation has been rethought and reinterpreted in some parts in the hope of providing a fresh perspective on the subject. One supposed detail, on the other hand, has not received much attention so far: Even though the success of statistical field-theoretic models relies largely on their ability to decouple particle-particle interactions, interestingly enough, these hardly seem to have come into the actual focus of research. This chapter will therefore conclude by addressing this shortcoming and providing a new perspective on the issue. Finally, following our work [84], this section presents a novel systematic classification of interactions commonly used in FTS.

The decoupling of the particle-particle interactions is accomplished by applying the Gaussian integral identity from Eq. (2.8) as can be seen from the model building principles of Section 2.2. This step introduces the inverse potential u^{-1}, being the *functional* inverse of u, into the field-theoretic model equations. The pair potential u and its inverse u^{-1} are related according to the definition of functional inverses via [31]

$$\int_{\mathbb{R}^d} \mathrm{d}^d r' \; u(\boldsymbol{r}-\boldsymbol{r}')\, u^{-1}(\boldsymbol{r}'-\boldsymbol{r}'') = \delta(\boldsymbol{r}-\boldsymbol{r}''). \tag{2.53}$$

The derivation of the functional inverse u^{-1} from this may seem innocent. However, it has been recognized over the years that this is not the case because for u^{-1} to exist u must have certain properties. As a consequence, the powerful tool of field-theoretic simulations is merely used for physically relatively simple models. Our systematic classification of non-bonded interactions commonly used in FTS, which has been first presented in Ref. [84], shall illustrate this. For this purpose, it is useful to write the part of the potential energy which is subject to the field transformation as

$$U_{ij} = \frac{1}{2} \left\langle \hat{\rho}_i | u_{ij} | \hat{\rho}_j \right\rangle . \tag{2.54}$$

By introducing the subscripts i, j, interactions between different species types can be considered such as the components of a block copolymer or of polymer blends.

In light of Eq. (2.53), probably the most obvious choice of u is the explicit use of δ-interactions. Unsurprisingly, this first class of interactions shall therefore be termed the class of "explicit δ-interactions". These interactions can be identified in the literature either between the same species type or between different types of species. The former case is widely used for modeling excluded volume effects. For instance, the homopolymer model consisting of continuous chains and explicit δ-interactions in the form

$$u(\boldsymbol{r}) = u_0\,\delta(\boldsymbol{r}), \tag{2.55}$$

with u_0 being the excluded volume parameter and the inverse

$$u^{-1}(\boldsymbol{r}) = \frac{1}{u_0}\delta(\boldsymbol{r}), \tag{2.56}$$

is better known as the famous Edwards model for homopolymers [29]. The latter case is better known as the field-theoretic analogue of the Flory–Huggins interactions [85, 86], which are used to model dissimilarity between chemical components. In AB diblock copolymer models [87–90], for example, an energetic contribution in the form

$$U_{AB} = \frac{\chi_{AB}}{2}\left\langle\hat{\rho}_A|\hat{\rho}_B\right\rangle, \tag{2.57}$$

with χ_{AB} being the Flory–Huggins parameter, is often used for this purpose. By rewriting Eq. (2.57) (see also Eq. (A.2.6)) as

$$U_{AB} = \frac{1}{2}\left\langle\hat{\rho}_A|\chi_{AB}\delta|\hat{\rho}_B\right\rangle, \tag{2.58}$$

it is easy to identify the explicit δ-interactions between components A and B as

$$u_{AB}(\boldsymbol{r}) = \chi_{AB}\,\delta(\boldsymbol{r}). \tag{2.59}$$

Conceptually, therefore, this latter case is very similar to the former case, albeit linear combinations of the microscopic densities are required to apply the Gaussian integral identity, as outlined in the model building in Sec. 2.2.

Another approach to solving Eq. (2.53) is the hope of finding useful potentials which satisfy this equation through integration by parts. Hence, the inevitable appearance of derivatives of the Dirac delta function becomes comprehensible in this way. Since these terms are not necessarily directly evident from the interaction potential u of the particle-based model but are present in the field-theoretic model, this second class shall be termed the class of "implicit δ-interactions". So far, this relatively difficult approach does not seem to have been very successful in deriving relevant potentials, and there are very few examples to count. In a seminal work by Edwards [30] the functional inverse of the Yukawa potential is given that way. Furthermore, the Coulomb potential as a limiting case of it is commonly used in field-theoretic studies of complex coacervates [48, 47]. Here, the interactions are formulated as

$$U_c = \frac{1}{2}\left\langle\hat{\rho}_c\left|\frac{\lambda_B'}{r}\right|\hat{\rho}_c\right\rangle, \tag{2.60}$$

with $\hat{\rho}_c(\boldsymbol{r})$ being the microscopic charge density, $\lambda_B = \lambda'_B/(k_BT)$ the Bjerrum length, and $r = |\boldsymbol{r}|$ the radial coordinate. Using the identity for the Green's function of the three-dimensional Laplace operator

$$-\nabla^2 \frac{1}{4\pi r} = \delta(\boldsymbol{r}), \tag{2.61}$$

it is straightforward to find the following pair of the Coulomb potential in three dimensions:

$$u_c(\boldsymbol{r}) = \frac{\lambda'_B}{r}, \tag{2.62}$$

$$u_c^{-1}(\boldsymbol{r}) = -\frac{1}{4\pi\lambda'_B}\nabla^2\delta(\boldsymbol{r}). \tag{2.63}$$

As can be seen, in this example of implicit δ-interactions, a derivative of the Dirac delta function enters the field-theoretic model directly through u_c^{-1}, whereas this δ-term is not immediately obvious only by glancing at u_c.

Besides these two approaches of explicit and implicit δ-interactions, no other solution methods seem to be widespread for deriving additional u, u^{-1} pairs to be used in field-theoretic models. What can be found instead has its origin in a technique for regularization of ultraviolet (UV) divergent field-theoretic models [91, 92, 34]. These ultraviolet divergences manifest themselves mainly by failing to observe convergence of (individual) derived observables under increasing refinement of the discrete description and they have their origin in an occurring divergence in the pair potential u (like with the δ-potential at $r = 0$). As a remedy for this UV divergent behavior, an established regularization approach is the smearing of the microscopic densities by a convolution. In this approach, the microscopic densities are replaced by a convolution with, for example, a Gaussian [92] before the particle-to-field transformation is applied. It is important to note that this changes the microscopic model and replaces Eq. (2.54) with

$$U'_{ij} = \frac{1}{2}\left\langle \Gamma_i * \hat{\rho}_i | u_{ij} | \Gamma_j * \hat{\rho}_j \right\rangle, \tag{2.64}$$

where Γ_i (or Γ_j) denotes a general masking function used for convolution (e.g., the 3D Gaussian mentioned above). It is then a mathematical argument, namely the rewriting of Eq. (2.64) (see Eq. (A.2.9) for this) as

$$U'_{ij} = \frac{1}{2}\left\langle \hat{\rho}_i | \Gamma_i * u_{ij} * \Gamma_j | \hat{\rho}_j \right\rangle, \tag{2.65}$$

which illustrates the equivalence of the picture of smeared particles interacting through the original potentials (as in Eq. (2.64)) with the picture of the original particles interacting through smeared potentials instead (as in Eq. (2.65)). Through the convolution approach, the interaction potential u is thus replaced by an effective potential of the form

$$u'_{ij}(\boldsymbol{r}) = \left[\Gamma_i * u_{ij} * \Gamma_j\right](\boldsymbol{r}). \tag{2.66}$$

From this perspective, this convolution (or smearing) approach can be interpreted as a third class of interactions, representing an extension to the first two classes of explicit and implicit δ-interactions. In respect of the masking function Γ, this third class shall be termed the class of "masked δ-interactions". In addition to introducing Gaussian pair interactions into FTS, nanoparticles in polymer nanocomposites, for example, have also been modeled in this way. In that case, the spatial extent of nanoparticles has been described in reference [56] by masking point particles with the complementary error function (erfc).

In summary, the three discussed classes of interactions commonly used in FTS are shown in Table 2.1. The explicit δ-interactions cer-

	explicit δ	**implicit δ**	**masked δ**
interactions	δ-interactions, Flory–Huggins	Coulomb, Yukawa	Gaussian, derived from erfc
applications	Edwards model, (di)block copolymers	complex coacervates	UV regularization, nanoparticles

TABLE 2.1: Systematic classification of non-bonded pair interactions common in field-theoretic models.

tainly represent the simplest interaction model. Even though the high degree of simplicity of this class renders the resolution of atomic-scale features impossible, this type of interaction has nevertheless proven to be extremely useful in toy models of polymeric systems. Much more sophisticated interactions can be realized in the class of implicit δ-interactions. Unfortunately, the derivation of physically relevant interactions seems relatively difficult in this case, so that only very few examples can be found. The more recent approach of masked δ-interactions has proven useful not only for the regularization of UV divergent models but it also allows the field-theoretic modeling of particles with finite spatial extent. Upon closer inspection of the modeling (which will be an essential part of Chapter 3), it turns out that the original interactions are essentially augmented with the masking function with no new functional inverse appearing in the field-theoretic model. However, one should keep in mind that this regularization process results in a complicated field-theoretic description and also that the smearing of the microscopic densities fundamentally changes the underlying particle model.

The above classification of interactions common in FTS has dramatically shown the severe limitation to the framework that exists in the choice of non-bonded particle interactions. Returning now to the components of FTS models illustrated in Fig. 2.4, this problem appears all the more profound: what distinguishes field-theoretic simulations significantly is their ability to decouple the non-bonded particle-particle interactions. However, it is at this point, of all places, that the weak spot of this yet so beautiful framework appears to be! If this fundamental problem could be overcome, it would most likely amount to a

breakthrough in this field of research. It is this ambition to enrich the set of physically relevant interactions that motivates the subsequent chapters of this dissertation. The systematic classification elaborated here shall serve as a helpful guidance for that purpose. So, in the following chapter, it will first be proceeded to take up and continue the concepts of masked δ-interactions.

3

SMEARED FIELDS IN FTS: CONVOLUTIONS AND MASKED INTERACTIONS

If others would but reflect on mathematical truths as deeply and continuously as I have, they would make my discoveries.

— Carl Friedrich Gauß

For some time now, polymers have been the subject of "smearing", not only as far as it concerns their overwhelming use in our society nowadays but also in terms of treating microscopic densities in polymer models. This latter modeling is originally motivated by a regularization approach of field-theoretic models in which there are divergences in the pair interactions. By replacing the microscopic density, typically with a Gaussian convoluted one [92], the density is smeared and the underlying microscopic model is thus changed. As a result of the change, the obtained regularized model is free of UV divergences. At the same time, this regularization can also be understood as effectively changing the non-bonded interactions of the original non-smeared microscopic density, as discussed in Section 2.4. Since no new functional inverses need to be found to describe these interactions, this class seems to be of particular interest for realizing new and physically relevant interactions in FTS. In this context, and as an introduction to embedding advanced interactions into the field-theoretic simulation framework, this chapter will address some important conceptual issues related with this evident possibility. Here, *conceptual* shall mean to explore the fundamental options available for employing advanced masked interactions in FTS. As such, Section 3.1 focuses on novel Γ masking functions that lead to new effective potentials through the masking of δ-interactions. After an in-depth analysis of the challenges in deriving the functional inverse potential u^{-1} in Section 3.2, Section 3.3 moves away from the original δ-interactions to address a convoluted version of a more general u^{-1}. Finally, in Section 3.4, the potentially far-reaching approach building on the concept of convoluted inverse potentials is demonstrated by two examples.

3.1 SMEARED DENSITY MODELS AND A GENERALIZATION

What distinguishes a smeared density model from the original field-theoretic one is a modified particle-based model, with the modification through a masking function carried smoothly throughout the field-theoretic modeling. Revisiting the introductory example of the monatomic fluid presented in Section 2.2, the starting point of its

smeared variant is the analogue of Eq. (2.4) for a convoluted microscopic density:

$$U' = \frac{1}{2}\langle \Gamma * \hat{\rho} | u | \Gamma * \hat{\rho} \rangle - \frac{n}{2}\left[\Gamma * u * \Gamma\right](\mathbf{0}). \tag{3.1}$$

The self-interaction term is also embedded in convolutions with the masking function Γ and thus possible divergences from $u(\mathbf{0})$ can be removed.[1] Although this formulation can be considered in the context of an effective potential acting on $\hat{\rho}$ (see Eqs. (2.64)-(2.66)), it is important to emphasize that the particle-to-field transformation is performed with respect to the original pair potential u so that $\Gamma * \hat{\rho}$ is the quantity that is subject to the transformation. In the hypothetical case of transforming with respect to the effective potential $\Gamma * u * \Gamma$ keeping the microscopic density $\hat{\rho}$ intact, the original problem of finding the functional inverse would still exist. Following then the shorter path from Chapter 2 of directly transforming the canonical partition function for the purpose of model building, the application of the Gaussian integral identity leads to

$$\mathcal{Z}_c' \propto \int_{V^n} \mathrm{d}^{3n} r \int \mathcal{D}w \, \exp\left(-\frac{1}{2\beta}\left\langle w \middle| u^{-1} \middle| w \right\rangle - i\langle w | \Gamma * \hat{\rho}\rangle\right). \tag{3.2}$$

It is now possible to exchange the convolution in the last term of the exponent according to Eq. (A.2.7) (that is, $\langle w|\Gamma * \hat{\rho}\rangle = \langle \Gamma * w|\hat{\rho}\rangle$) and continue with the model building procedure to derive the field-theoretic Hamiltonian of the smeared model

$$\mathcal{H}'[w] = \frac{1}{2\beta}\left\langle w \middle| u^{-1} \middle| w \right\rangle - n \ln Q[i\Gamma * w]. \tag{3.3}$$

Compared to the non-smeared original one of Eq. (2.21), the masking function Γ enters the field-theoretic model in the functional argument of the reduced partition function Q.

Based on such a fundamental manipulation of the field-theoretic model, Villet and co-workers [92, 93] have brilliantly worked out a UV regularized version of the Edwards model and its derived field-based observables. What should be of particular interest in the context of this dissertation is not this regularization per se but the effective non-bonded interactions that follow from it. Specifically, in Villet's Gaussian-regularized Edwards model (GREM), a (3D) Gaussian masking function

$$\Gamma_G(\boldsymbol{r}) = \frac{1}{(2\pi a^2)^{3/2}} \exp\left(-\frac{|\boldsymbol{r}|^2}{2a^2}\right) \tag{3.4}$$

is used in combination with u from Eq. (2.55) describing δ-interactions. The effective interactions between point particles for Gaussian

1 For interaction potentials with a divergence in $u(\mathbf{0})$ that cannot be removed via a convolution, the Fourier integral is also not convergent so that the Fourier transform is not well-defined. As will become clear in Section 3.2, this renders the use of these pair potentials fundamentally difficult since the existence of the Fourier transform (or representations of it) appears of crucial importance for the calculation of the functional inverse u^{-1}.

masked δ-interactions are given, according to Eq. (2.66) (and as also noted between equations in the text of Ref. [92]), by

$$u'_G(\boldsymbol{r}) = u_0 \left[\Gamma_G * \Gamma_G\right](\boldsymbol{r}) \tag{3.5}$$

$$= \frac{u_0}{\left(4\pi a^2\right)^{3/2}} \exp\left(-\frac{|\boldsymbol{r}|^2}{4a^2}\right). \tag{3.6}$$

Effectively, point-like particles in this Gaussian-smeared description interact via a potential which is also a Gaussian but characterized by an adjusted variance $2a^2$. In a more general sense, zero-centered effective Gaussian interactions could serve as (non-orthogonal) basis functions to approximate a realistic pair potential function up to a certain accuracy. As will become clear later in the thesis (in Chapter 5 where the decomposition of a rather common pair potential is discussed), this requires the introduction of several (one for each basis function) auxiliary fields. Although this will proportionally increase the computational demands and the memory requirements, such a combination of simple masked δ-interactions seems to sketch a conceptual path for approximating potentials in FTS that are more realistic than the commonly considered ones.[2]

Another way to think about masked δ-interactions is presented in the work of Koski and co-workers on the modeling of nanoparticles [56]. In this case, the interactions are not modeled primarily with view to an effective interaction potential. Instead, the interpretation of the interactions takes place much more on the level of the microscopic density in view of the finite spatial extent of point particles. More specifically, point particles are convoluted with a complementary error function as a masking function, with the understanding that these expanded (mass) structures interact with each other locally via δ-interactions. Although this picture can also be applied to Villet's GREM to some extent, Koski's work differs fundamentally in that, when using the complementary error function as a masking function, the analytical calculation of the effective interaction potential does not appear to be straightforward, so that it was given graphically (Fig. 3 in Ref. [56]) and it seems not obvious from its shape to recognize the masking function in contrast to the GREM case. From this point of view, the choice of the masking function seems arbitrary to some extent or, to put it more gently, there seems to be at least a certain freedom in the choice of possible Γ's. To cover the options of incorporating advanced interactions into FTS as fully as possible, this freedom in the choice of feasible Γ's is briefly explored next.

The starting point for identifying masking functions to transform δ-interactions to tractable effective potentials for use in FTS is Eq. (3.5) valid for any masking function. To calculate the hypothetical masking

2 I would like to thank Prof. Fredrickson for mentioning this approach to approximate realistic potentials in FTS. Based on this idea, I would like to further propose to also consider derivatives of Gaussians with the aim of constructing a set of orthogonal basis functions (in analogy to Hermite functions).

function Γ for a particular effective potential u', it is useful to transform this equation into Fourier space and formally solve for $\hat{\Gamma}$, the Fourier transform of Γ, by using the convolution theorem:

$$\hat{\Gamma}(\boldsymbol{k}) = \sqrt{\frac{\hat{u}'(\boldsymbol{k})}{u_0}}. \tag{3.7}$$

This simple equation may seem inconspicuous, yet it has several implications regarding the choice and actual use of the masking function. First of all, of course, the Fourier transform $\hat{u}'$ of the effective pair potential must exist. As discussed in Chapter 2, the requirement to possess a Fourier transform also applies to the bare potential u, although the argument for effective potentials is a conceptually different one. This requirement excludes from the very beginning the vast majority of typical pair potentials (in their unregularized form) exhibiting specific divergences at $r = 0$. Second, and less obvious, the Fourier integral of radially symmetric pair potentials contains only real terms. For real masking functions,[3] the square root must be positive and thus, with $u_0 > 0$, $\hat{u}'$ must be positive. As a consequence of considering real masking functions, only those qualify for which $\hat{\Gamma}$ is also positive. Third, the derived hypothetical Fourier transform $\hat{\Gamma}$ should be unproblematic to handle when transforming back to Γ. This last point requires an appropriate decay behavior of $\hat{\Gamma}$ in the Fourier integral. In view of such a generalization of the masking function and the underlying conditions, at least the choice of analytic forms for both Γ and u' for physically meaningful purposes seems challenging. Nonetheless, and as a closing to this section, the detail of such a generalization can be demonstrated by means of a (to the best of our knowledge) novel example.

Motivated by the decaying exponential interactions to be discussed in Chapters 4 and 5, the effective potential

$$u'_{\mathrm{ex1}}(\boldsymbol{r}) = A \exp\left(-B\,|\boldsymbol{r}|\right), \quad B > 0 \tag{3.8}$$

is considered here whose 3D Fourier transform is

$$\hat{u}'_{\mathrm{ex1}}(\boldsymbol{k}) = \frac{8\pi AB}{\left(|\boldsymbol{k}|^2 + B^2\right)^2}. \tag{3.9}$$

Using Eq. (3.7) and comparing with the functional form of the Yukawa potential

$$u_Y(\boldsymbol{r}) = a_Y \frac{\exp\left(-b_Y\,|\boldsymbol{r}|\right)}{|\boldsymbol{r}|}, \quad b_Y > 0 \tag{3.10}$$

3 The restriction to real masking functions seems natural in the physical picture of density smearing. From a mathematical point of view, however, this restriction does not seem compelling. In fact, for the d-dimensional Gaussian integral in Eq. (A.1.1), from which the Gaussian integral identity is derived, a complex-valued $\boldsymbol{b}$ (corresponding to the density field ρ) is possible. The condition of a positive definite matrix $\boldsymbol{A}$ is preserved, since, in terms of continuous functions, the original u is not altered by the convolution.

and its Fourier transform

$$\hat{u}_Y(\boldsymbol{k}) = \frac{4\pi a_Y}{|\boldsymbol{k}|^2 + b_Y^2}, \tag{3.11}$$

the masking function belonging to u'_{ex1} is then identified as

$$\Gamma_{\mathrm{ex1}}(\boldsymbol{r}) = \sqrt{\frac{AB}{2\pi u_0}} \frac{\exp\left(-B\,|\boldsymbol{r}|\right)}{|\boldsymbol{r}|}. \tag{3.12}$$

Exponentially decaying effective interactions such as that of Eq. (3.8) between point-like particles can thus be modeled by convolution of the microscopic density with a function similar to that of the Yukawa potential.[4] Conversely, the Fourier pairs from Eqs. (3.8) and (3.9) can be used in a similar way to derive for the effective potential

$$u'_{\mathrm{ex2}}(\boldsymbol{r}) = \frac{AB}{\left(|\boldsymbol{r}|^2 + B^2\right)^2}, \quad B > 0 \tag{3.13}$$

the following masking function:

$$\Gamma_{\mathrm{ex2}}(\boldsymbol{r}) = \sqrt{\frac{A}{u_0}} \frac{8B}{\pi\left(4\,|\boldsymbol{r}|^2 + B^2\right)^2}. \tag{3.14}$$

As in the case of effective Gaussian interactions, the similarity between the functional form of the potential u'_{ex2} and that of the masking function Γ_{ex2} is apparent.

3.2 INSIGHTS FROM A REFORMULATED EQUATION FOR u^{-1}

In connection with convolutions of the microscopic density field and the resulting effective interaction potentials arising between point-like particles, the generalization of the masking function for δ-interactions was presented in the previous section. As a counterpart to the effective potential, the concept of an effective *inverse* potential will be proposed for the first time later in this dissertation. For an understanding of why this step may be worthwhile, this intermediate Section 3.2 deviates somewhat from the discussion of convolutions in field-theoretic models by presenting in some more detail the properties of the defining equation for the inverse potential u^{-1}.

To begin with, the usual notation in the FTS literature of the defining equation of u^{-1} through Eq. (2.53) shall be understood for the case of a radially symmetric interaction potential u and the corresponding symmetry property of u^{-1} shall be concluded. As a basis, the most general form of this defining equation of u^{-1} is to be used [64], namely

$$\int_{\mathbb{R}^d} \mathrm{d}^d r'\; u(\boldsymbol{r}, \boldsymbol{r}')\, u^{-1}(\boldsymbol{r}', \boldsymbol{r}'') = \delta(\boldsymbol{r} - \boldsymbol{r}''). \tag{3.15}$$

4 It seems important to note that, as long as Γ_{ex1} is applied together with a convolution, the apparent singularity at $r = 0$ is not transferred to the convoluted function (due to 3D radial symmetry).

In the next step, a radially symmetric interaction potential, that is $u(\boldsymbol{r},\boldsymbol{r}') = u(|\boldsymbol{r}-\boldsymbol{r}'|)$, is assumed. With $\boldsymbol{R}$ being a general rotation matrix, the relation

$$u(\boldsymbol{r},\boldsymbol{r}') = u(\boldsymbol{R}\cdot\boldsymbol{r},\boldsymbol{R}\cdot\boldsymbol{r}') \tag{3.16}$$

then holds for all rotation angles due to the radial symmetry. The introduction of this general rotation matrix is helpful, since

- $u^{-1}(\boldsymbol{r},\boldsymbol{r}')$ is the inverse of $u(\boldsymbol{r},\boldsymbol{r}')$ and thus also of $u(\boldsymbol{R}\cdot\boldsymbol{r},\boldsymbol{R}\cdot\boldsymbol{r}')$,
- $u^{-1}(\boldsymbol{R}\cdot\boldsymbol{r},\boldsymbol{R}\cdot\boldsymbol{r}')$ is the inverse of $u(\boldsymbol{R}\cdot\boldsymbol{r},\boldsymbol{R}\cdot\boldsymbol{r}')$ and thus also of $u(\boldsymbol{r},\boldsymbol{r}')$.

Given the uniqueness of the inverse, it also follows that

$$u^{-1}(\boldsymbol{r},\boldsymbol{r}') = u^{-1}(\boldsymbol{R}\cdot\boldsymbol{r},\boldsymbol{R}\cdot\boldsymbol{r}') \tag{3.17}$$

and thus the inverse $u^{-1}(\boldsymbol{r},\boldsymbol{r}') = u^{-1}(|\boldsymbol{r}-\boldsymbol{r}'|)$ is also radially symmetric. Therefore, for radially symmetric interaction potentials, Eq. (3.15) can be written as

$$\int_{\mathbb{R}^d} \mathrm{d}^d r'\; u(|\boldsymbol{r}-\boldsymbol{r}'|)\, u^{-1}(|\boldsymbol{r}'-\boldsymbol{r}''|) = \delta(\boldsymbol{r}-\boldsymbol{r}''). \tag{3.18}$$

Beyond that, the expression

$$\int_{\mathbb{R}^d} \mathrm{d}^d r_1\; u(|\boldsymbol{r}_0-\boldsymbol{r}_1|)\, u^{-1}(|\boldsymbol{r}_1|) = \delta(\boldsymbol{r}_0) \tag{3.19}$$

can be derived by variable substitution, which corresponds to the definition of the convolution

$$\left[u * u^{-1}\right](\boldsymbol{r}) = \delta(\boldsymbol{r}). \tag{3.20}$$

The special attractive feature of this simpler form of the convolution equation is that it allows for a more intuitive understanding of the inverse potential problem. Besides the obvious picture of the potential being smeared by the inverse potential, the convolution equation permits a solution approach by Fourier transform, since a direct application of the convolution theorem provides a relation between the hypothetical Fourier transform of the inverse potential and the Fourier transform of the interaction potential as

$$\mathcal{F}[u^{-1}](\boldsymbol{k}) = \left(\mathcal{F}[u](\boldsymbol{k})\right)^{-1}. \tag{3.21}$$

This relation implies certain constraints on the functional form of u for $\left(\mathcal{F}[u](\boldsymbol{k})\right)^{-1}$ to be a well-defined quantity. As in the case of the effective interaction potential u' discussed in the previous section, an important condition that u must possess is to have a Fourier transform. Once again, this condition excludes hard-core models with specific divergences at $r = 0$. Moreover, and in order to avoid divergences in $\hat{u}^{-1}(\boldsymbol{k}) := \mathcal{F}[u^{-1}](\boldsymbol{k})$, it is essential that $\hat{u}(\boldsymbol{k}) := \mathcal{F}[u](\boldsymbol{k})$ has no roots and thus does not change sign. Interaction potentials for which such a sign change of the Fourier transform occurs are special

in other respects [94] but cannot be used in this context. In consideration of the discrete case of the positive definite $\boldsymbol{u}$ matrix discussed in Appendix A.1, the typical requirement $\hat{u} > 0$ in the FTS literature [64] is thus straightforward to understand.

Eq. (3.21) reveals a key problem that exists in the relation between u and u^{-1}. This issue can already be sensed from the intuitive picture of smearing u by u^{-1}, requiring a delta function to be generated from it (Eq. (3.20)): Typical interaction potentials u, such as the Yukawa one discussed above, drop to zero at large distances r. Likewise, their Fourier transform $\hat{u}$ drops to zero for large wavenumbers k and the transformation between u and $\hat{u}$ via the corresponding radial Fourier integrals is unproblematic and straightforward. However, when considering the inverse $\hat{u}^{-1}$ in Eq. (3.21), the decrease of $\hat{u}$ with k results in an increase of $\hat{u}^{-1}$ with k. This behavior, in turn, renders the derivation of the back-transform u^{-1} challenging with regard to the rising integrand in the Fourier integral. By means of the intuitive potential-smearing picture, the fundamental question may even arise whether it is principally possible at all to transform non-delta functions by a smearing to a single delta peak.[5] The answer can be found through the class of implicit δ-interactions: there exist functions that have a close, non-obvious relation with the delta function, which only becomes obvious in Fourier space by Eq. (3.21) rendering such a smearing of u indeed possible. For the Yukawa potential of Eq. (3.10) or the Coulomb potential of Eq. (2.62) as the limiting case $b_Y \to 0$ of it, it is interesting to note that such an increase of $\hat{u}^{-1}$ with k is captured by the Laplacian (acting on the delta function) and u^{-1} can be given accordingly as in Eq. (2.63). This property will be exploited in Chapter 5 to find ways to directly calculate u^{-1} for advanced interaction potentials. Before this, in the next section, the concept of using a (Gaussian) masking function for regularization will be discussed in the context of the inverse potential u^{-1}.

3.3 A SECOND GENERALIZATION AND CONVOLUTIONS OF u^{-1}

In Section 3.1, the idea of using masking functions that gives rise to the concept of effective potentials was brought up and discussed, leaving aside the original concern of Gaussian regularized field-theoretic models (namely the regularization of UV divergent behavior [92]). In such a regularization, the focus is not on an explicit change of the interaction potential but on the development of a new model that is as close as possible to the original one but which, in contrast to that, does not contain the problematic property that results in the UV-divergent behavior. With this understanding it is comprehensible that Gaussian convolutions are used which contain the original model in the limiting case of infinitely narrow Gaussians (which means convolutions by delta functions). In that sense, the original underlying

5 I would like to thank Hans Christian for making me appreciate the tremendous importance of an intuitive understanding in mathematical descriptions and for asking such fundamental questions.

particle model is fundamentally changed, something that is evident in particular in the changed interaction term

$$\langle\hat{\rho}|u|\hat{\rho}\rangle \neq \langle\Gamma * \hat{\rho}|u|\Gamma * \hat{\rho}\rangle \tag{3.22}$$

for $\Gamma(\boldsymbol{r}) \neq \delta(\boldsymbol{r})$ and general u. In Sec. 3.1 it was recalled that the field-theoretic Hamiltonian $\mathcal{H}'$ of a smeared model (Eq. (3.3)) differs from the original $\mathcal{H}$ (Eq. (2.21)) only in the functional argument of the reduced partition function Q. Since Q is the only component in the field-theoretic model in which the microscopic density appears, this is understandable and will actually inspire a useful subscript shorthand notation here.

This new notation shall be introduced as straightforwardly as possible using the simple monatomic fluid example introduced in Sec. 2.2. Given that the reduced partition function is defined directly in terms of the $\langle w|\hat{\rho}\rangle$ leftover involving the microscopic density $\hat{\rho}$ from the particle-to-field transformation (Eq. (A.1.14)) as

$$Q[iw]^n = \frac{1}{V^n}\int_{V^n} \mathrm{d}^{3n}r \;\exp\left(-i\,\langle w|\hat{\rho}\rangle\right) \tag{3.23}$$

and concerning the contained $\hat{\rho}$, this Q shall be provided with an appropriate subscript as

$$Q[iw]_{\hat{\rho}} := Q[iw]. \tag{3.24}$$

Then, along with the introduction of the convoluted microscopic density

$$\breve{\rho}(\boldsymbol{r}) := [\Gamma * \hat{\rho}]\,(\boldsymbol{r}), \tag{3.25}$$

the corresponding Q for a convoluted argument can be written as

$$\begin{aligned} Q[i\Gamma * w]^n &= \frac{1}{V^n}\int_{V^n} \mathrm{d}^{3n}r \;\exp\left(-i\,\langle \Gamma * w|\hat{\rho}\rangle\right) && (3.26)\\ &= \frac{1}{V^n}\int_{V^n} \mathrm{d}^{3n}r \;\exp\left(-i\,\langle w|\breve{\rho}\rangle\right) && (3.27)\\ &=: Q[iw]^n_{\breve{\rho}} && (3.28) \end{aligned}$$

and, similar, for the double convoluted microscopic density

$$\breve{\breve{\rho}}(\boldsymbol{r}) := [\Gamma * \Gamma * \hat{\rho}]\,(\boldsymbol{r}) \tag{3.29}$$

as

$$Q[i\Gamma * \Gamma * w] = Q[iw]_{\breve{\breve{\rho}}}. \tag{3.30}$$

This procedure suggests the second conceptual generalization of this chapter, namely the generalization of the microscopic density and thus the possibility of multi-convoluted models. Additionally, and with respect to Eqs. (3.24), (3.28), and (3.30), it seems reasonable to introduce a general (undecorated) placeholder density ρ for use in the field-theoretic model and in particular with Q. Even though this subscript notation was introduced using the monatomic fluid as an

example, in general Q contains the microscopic density always in the pair $\langle w|\hat{\rho}\rangle$ due to the property of the particle-to-field transformation.[6] Therefore, this notation can be applied generally and is not restricted to the above example.

The notation is particularly useful because it connects the manipulated field representation (here through Q) directly to the corresponding particle representation (here through ρ) for general pair potentials. This illustration of the effects on the field model from changing the underlying particle model shall motivate the reverse case: Since the particle-to-field transformation by means of the Gaussian integral identity is approximation-free, it is equally conceivable to manipulate the field-theoretic description and study the corresponding consequences on the particle-based description. In analogy to the particle-based manipulation of $\hat{\rho}$ by Inequality (3.22), a core component of the field-theoretic model shall now be manipulated as

$$\left\langle w\middle|u^{-1}\middle|w\right\rangle \neq \left\langle w\middle|\Gamma * u^{-1} * \Gamma\middle|w\right\rangle \tag{3.31}$$

for $\Gamma(\boldsymbol{r}) \neq \delta(\boldsymbol{r})$ and general u^{-1}. For clarity, it is advantageous to label the (inverse) potential with a corresponding label so that, with respect to Inequality (3.31),

$$u_2^{-1}(\boldsymbol{r}) := \left[\Gamma * u_1^{-1} * \Gamma\right](\boldsymbol{r}) \tag{3.32}$$

can be viewed as an effective convoluted inverse potential. Rearranging Eq. (3.32) in Fourier space and utilizing Eq. (3.21), it is found that

$$u_1(\boldsymbol{r}) = [\Gamma * u_2 * \Gamma](\boldsymbol{r}). \tag{3.33}$$

To understand now how the manipulation of the field-theoretic model given by Inequality (3.31) affects the particle-based description, the above simple monatomic fluid example shall be used to compare the relevant terms of the particle-to-field transformations for both cases u_1 and u_2. For the general microscopic density ρ_1 associated with the interaction potential u_1, one can find the relation:

$$\int_{V^n} \mathrm{d}^{3n}r\ \exp\left(-\frac{\beta}{2}\langle\rho_1|u_1|\rho_1\rangle\right) \propto \frac{\int \mathcal{D}w\ \exp\left(-\frac{1}{2\beta}\left\langle w\middle|u_1^{-1}\middle|w\right\rangle + n\ln Q[iw]_{\rho_1}\right)}{\int \mathcal{D}w\ \exp\left(-\frac{1}{2\beta}\left\langle w\middle|u_1^{-1}\middle|w\right\rangle\right)}. \tag{3.34}$$

Similar, for the general microscopic density ρ_2 associated with the interaction potential u_2, one can find the analogous relation:

$$\int_{V^n} \mathrm{d}^{3n}r\ \exp\left(-\frac{\beta}{2}\langle\rho_2|u_2|\rho_2\rangle\right) \propto \frac{\int \mathcal{D}w\ \exp\left(-\frac{1}{2\beta}\left\langle w\middle|\Gamma * u_1^{-1} * \Gamma\middle|w\right\rangle + n\ln Q[iw]_{\rho_2}\right)}{\int \mathcal{D}w\ \exp\left(-\frac{1}{2\beta}\left\langle w\middle|\Gamma * u_1^{-1} * \Gamma\middle|w\right\rangle\right)}. \tag{3.35}$$

6 As can be seen from Section 2.2, w is conjugate to the density field and can therefore be conceived as a kind of position-dependent chemical potential field or, more illustratively, as a "density killer field" (credited to Hans Christian).

In Eqs. (3.34) and (3.35), it is important to emphasize that the model has been changed by the double convolution of u_1^{-1}. Moreover, and in contrast to the GREM [92] discussed in Section 3.1 where the model was modified by smearing the microscopic density, in the present case there is freedom to choose the corresponding microscopic density field ρ_2 in relation to ρ_1 such that model equivalence is established. More precisely, substituting Eq. (3.33) into (3.34) and comparing with Eq. (3.35), the following condition for model equivalence is found:

$$\langle \Gamma * \rho_1 | u_2 | \Gamma * \rho_1 \rangle \stackrel{!}{=} \langle \rho_2 | u_2 | \rho_2 \rangle \tag{3.36}$$

or, equivalently,

$$\rho_2(\boldsymbol{r}) \stackrel{!}{=} [\Gamma * \rho_1](\boldsymbol{r}). \tag{3.37}$$

Together with the relation of the (inverse) potentials (Eqs. (3.32) and (3.33)), this connection between general microscopic densities can be used recursively to relate additional field descriptions containing multi-convoluted density fields one to the other (based on the choices of ρ_1, u_1 and ρ_2, u_2).

To interpret the effect of manipulating the field-theoretic description at the level of the particle-based description, it is helpful to refer back to Eqs. (3.34) and (3.35). Taking the monatomic fluid as an example, for the case $\rho_1 = \hat{\rho}$, point particles interacting via a physical pair potential u_1 can be imagined. But the direct calculation of u_1^{-1} itself as a stand-alone function may be difficult due to a non-decaying behavior of $\hat{u}_1^{-1}$ in Fourier space, as described in Section 3.2. In the alternative description, $\rho_2 = \check{\rho}$ as described by Eq. (3.25) and the smeared particles interact with a pair potential u_2. In view of Eq. (3.33), the specification of u_2 may seem as difficult as the direct calculation of u_1^{-1}. However, by model equivalence, the complex probability weights derived from Eqs. (3.34) and (3.35) are constructed so as to provide the same statistics under application; thus, the functional form of u_2 may remain only of hypothetical interest. The great advantage of the approach presented here is that problems in Fourier space caused by non-decaying functions can be circumvented for u_2^{-1} by choosing a suitable masking function (such as a Gaussian) whose Fourier transform $\hat{\Gamma}$ (then also a Gaussian) decays accordingly fast compared to the non-decaying $\hat{u}_1^{-1}$. In this way, a stand-alone function u_2^{-1} describing the inverse potential can be calculated. With this particular u_2^{-1}, it is then convenient to use the field-theoretic Hamiltonian of Eq. (3.35)

$$\mathcal{H}_2[w] = \frac{1}{2\beta} \left\langle w \middle| u_2^{-1} \middle| w \right\rangle - n \ln Q[iw]_{\rho_2} \tag{3.38}$$

to describe the *original* system (the one characterized by the interaction potential u_1 and the microscopic density ρ_1). It is encouraging that, mathematically, one can directly arrive at a field-theoretic Hamiltonian that is equivalent to Eq. (3.38) by just substituting the field w in Eq. (3.34) with $\Gamma * w$; however, such an approach does not reveal the corresponding implications of the transformation for the interactions

at the particle level.[7] It should be emphasized again that although the example of the monatomic fluid has been chosen here for demonstration purposes, the concept based on the general equations (3.31), (3.32), (3.33), and (3.37) is by no means restricted to this example and can be applied generally.

3.4 EXAMPLES FOR CONVOLUTED INVERSE POTENTIALS

After having motivated multi-convoluted models and elaborated their underlying theoretical concepts in the previous section, this section is devoted to applying this general approach in two examples. Given that the method was also inspired by the density smearing in the GREM, the application to it as the first example seems natural. As second example, an analytical consideration in conjunction with the Yukawa potential follows, whose already well-known inverse potential is rederived as a limiting case.

In the GREM case, as presented in Ref. [92] by Villet and Fredrickson, a Gaussian (Eq. (3.4)) is used as a masking function of the continuous polymer chains, and the relevant quantities of the model can be specified in the context of the above discussion as listed in Table 3.1. Unlike the general case, and due to the simple form of the interac-

	original GREM	**convoluted GREM**
microscopic density	$\rho_1 = \Gamma * \hat{\rho}$	$\rho_2 = \Gamma * \Gamma * \hat{\rho}$
interaction potential	$u_1 = u_0\,\delta$	u_2 not specified
inverse potential	$u_1^{-1} = u_0^{-1}\,\delta$	$u_2^{-1} = \Gamma * u_1^{-1} * \Gamma$
field-theoretic Hamiltonian	$\mathcal{H}_1 = \frac{1}{2\beta}\left\langle w\middle\vert u_1^{-1}\middle\vert w\right\rangle - n \ln Q[i\Gamma * w]$	$\mathcal{H}_2 = \frac{1}{2\beta}\left\langle w\middle\vert \Gamma * u_1^{-1} * \Gamma\middle\vert w\right\rangle - n \ln Q[i\Gamma * \Gamma * w]$

TABLE 3.1: Relevant quantities in the application of the novel multi-convoluted density approach to the original GREM by Villet and Fredrickson [92].

tions, both u_1 and its inverse u_1^{-1} can be specified, whereas it seems to be very difficult to give the functional form of u_2. As described above, it is nevertheless possible to specify the inverse u_2^{-1} by requiring model equivalence. To demonstrate that this theoretical construct also works in practice, the GREM was implemented for this work from scratch for a fully fluctuating field based on the descriptions of Ref. [92], and then accordingly extended following the new approach.

A physical quantity on which Villet and Fredrickson [92] put a special focus is the excess chemical potential. It is straightforward to introduce this quantity in terms of the Helmholtz free energy

$$A(n, V, T) = -k_B T \ln \mathcal{Z}_c(n, V, T) \tag{3.39}$$

$$= A_{\mathrm{id}}(n, V, T) + A_{\mathrm{ex}}(n, V, T). \tag{3.40}$$

7 I would like to thank Prof. Fredrickson for bringing this issue to my attention.

As indicated in Eq. (3.40), the Helmholtz free energy splits into a non-interacting ideal gas part and an excess part. The chemical potential, given by its thermodynamic definition

$$\mu = \left.\frac{\partial A}{\partial n}\right|_{T,V} \tag{3.41}$$

$$= \mu_{\mathrm{id}} + \mu_{\mathrm{ex}}, \tag{3.42}$$

may be split analogously into an ideal and an excess part. Considering the self-interaction term $\frac{nn_m}{2}\left[\Gamma * u_1 * \Gamma\right](\mathbf{0})$ of Eq. (3.1) and the field-theoretic Hamiltonians in Table 3.1, the excess chemical potential of the original (μ_{ex1}) and of the convoluted (μ_{ex2}) model can be found by insertion and differentiation as

$$\mu_{\mathrm{ex1,2}} = -k_B T \left\langle \ln Q[iw]_{\rho_1,\rho_2} \right\rangle - \frac{n_m}{2}\left[\Gamma * u_1 * \Gamma\right](\mathbf{0}). \tag{3.43}$$

Based on this relation, it seems logical to introduce a field-theoretic observable in connection with the excess chemical potential as

$$\tilde{\mu}_{1,2} = -\ln Q[iw]_{\rho_1,\rho_2} \tag{3.44}$$

such that

$$\beta\mu_{\mathrm{ex1,2}} = \left\langle \tilde{\mu}_{1,2} \right\rangle - \frac{\beta n_m}{2}\left[\Gamma * u_1 * \Gamma\right](\mathbf{0}). \tag{3.45}$$

Following the original work by Villet and Fredrickson [92], dimensionless units can be introduced[8] and the chain propagators of the continuous chains can be computed according to the pseudo-spectral algorithm [64] employing an improved scheme by Ranjan, Qin, and Morse [95] for integration along the chain contour. For the t integration of the complex Langevin equation, the "limit" method[9] of Ref. [96] can be used as a straightforward extension of the Euler–Maruyama (EM) method. The instantaneous values over simulation time of the real part[10] of both $\tilde{\mu}_1$ and $\tilde{\mu}_2$ are shown in Fig. 3.1 for a direct comparison of the two model variants. It is seen that both curves, starting from a (randomly chosen) initial state, rapidly approach a plateau and then fluctuate around it. Considering the basics of complex Langevin simulations described in Section 2.3, the ensemble average of field-theoretic observables is approximated by the mean of their instantaneous values in this plateau region. For the same choice of Γ (and only then), these plateaus appear congruent for both model variants and their value is in agreement with the work of Villet and Fredrickson (cf. Fig. 2a in [92]).

What seems less instructive in the case of the GREM example is the fact that through the simple functional form of u_1, its inverse u_1^{-1}

8 For simulations of the GREM presented here, the following values were chosen in the variable notation of Ref. [92]: $B = 1$, $C = 1$, $\alpha = 0.1$, $\tilde{L} = 3.2$, $M = 32^3$, $ds = 0.01$, $dt = 0.001$.

9 I would like to thank Xiaocheng Shang for suggesting this method to me.

10 Since the mean value of the corresponding imaginary part vanishes due to the nature of the complex Langevin equation, only the real part shall be of interest.

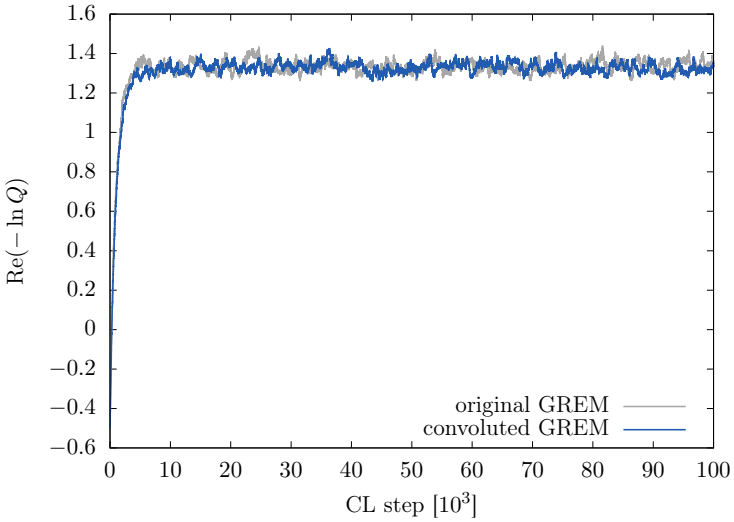

FIGURE 3.1: Comparison of the field-theoretic observable $\tilde{\mu}_1$ obtained from a reimplementation of the GREM according to Villet and Fredrickson [92] with the $\tilde{\mu}_2$ of the novel alternative model described here.

is trivially given. The basic intention of the novel alternative description of Section 3.3, namely to derive an inverse u_2^{-1} as a stand-alone function that exhibits decaying behavior in Fourier space and is thus straightforward to compute, is thus not fully revealed in the example. This issue is addressed in greater detail in the next example of the Yukawa potential. The Yukawa potential is particularly suitable for this purpose, since the problem of non-decaying functions in Fourier space can be readily demonstrated and its inverse is nontrivial and well-known (the latter is not necessary, yet will prove helpful).

In this example, $u_1 = u_Y$, i.e., the Yukawa potential defined by Eq. (3.10). To calculate the inverse u_2^{-1}, it is useful to provide not only the Fourier transform $\hat{u}_Y$, see Eq. (3.11), but also the Fourier transform of the Gaussian masking function Γ_G from Eq. (3.4) as

$$\hat{\Gamma}_G(\boldsymbol{k}) = \exp\left(-\frac{1}{2}a^2\,|\boldsymbol{k}|^2\right). \tag{3.46}$$

With these Fourier transforms and the adjusted variance $\overline{\sigma}^2 := 2a^2$ of the Gaussian, the inverse u_2^{-1} can be given in Fourier space according to Eq. (3.32) as

$$\hat{u}_2^{-1}(\boldsymbol{k}) = \frac{1}{4\pi a_Y}\left(|\boldsymbol{k}|^2 + b_Y^2\right)\,\exp\left(-\frac{1}{2}\overline{\sigma}^2\,|\boldsymbol{k}|^2\right). \tag{3.47}$$

The interplay of the first non-decaying interaction potential term with the second decaying exponential masking term is particularly obvious in Eq. (3.47). The presence of the exponential term makes the radial Fourier integral involving $\hat{u}_2^{-1}$ straightforward to solve, which allows obtaining the transform in the spatial domain as

$$u_2^{-1}(\boldsymbol{r}) = -\frac{1}{4\pi a_Y}\left(\frac{|\boldsymbol{r}|^2}{\overline{\sigma}^4} - \frac{3}{\overline{\sigma}^2} - b_Y^2\right)\,\frac{1}{\left(2\pi\overline{\sigma}^2\right)^{3/2}}\exp\left(-\frac{|\boldsymbol{r}|^2}{2\overline{\sigma}^2}\right), \tag{3.48}$$

thereby identifying a Gaussian contribution in the last part written separately. Even more important, parts of the polynomial in parentheses can be replaced by the 3D Laplacian acting on the Gaussian, thus the inverse can be expressed as

$$u_2^{-1}(\boldsymbol{r}) = -\frac{1}{4\pi a_Y}\left(\nabla^2 - b_Y^2\right)\ \frac{1}{\left(2\pi\overline{\sigma}^2\right)^{3/2}}\exp\left(-\frac{|\boldsymbol{r}|^2}{2\overline{\sigma}^2}\right). \tag{3.49}$$

As in the GREM example and its alternative description contrasted in Table 3.1, the inverse u_2^{-1} may be used in an alternative model described, for instance, by $\mathcal{H}_2$ as in Eq. (3.38).

In conclusion to this example, it seems instructive to discuss the limiting case when u_2^{-1} approaches u_1^{-1}. As is apparent from Section 3.3, this case occurs when the masking function is given by the Dirac delta function, which can be expressed as the limiting case of an infinitely narrow Gaussian by

$$\delta(\boldsymbol{r}) = \lim_{\overline{\sigma}\to 0}\frac{1}{\left(2\pi\overline{\sigma}^2\right)^{3/2}}\exp\left(-\frac{|\boldsymbol{r}|^2}{2\overline{\sigma}^2}\right). \tag{3.50}$$

This representation of the Dirac delta function can then be used to calculate the inverse of the Yukawa potential as a limiting case of Eq. (3.49) as

$$u_Y^{-1}(\boldsymbol{r}) = \lim_{\overline{\sigma}\to 0} u_2^{-1}(\boldsymbol{r}) \tag{3.51}$$

$$= -\frac{1}{4\pi a_Y}\left(\nabla^2 - b_Y^2\right)\delta(\boldsymbol{r}), \tag{3.52}$$

the latter expression already being well-known from Edwards' seminal work [30]. The case $\overline{\sigma} \to 0$ is also interesting with respect to the Fourier transform $\hat{u}_2^{-1}$ from Eq. (3.47). It suggests that non-decaying functions in Fourier space are not problematic per se but it is rather the finding of the functional form of the inverse which appears to be quite difficult. For non-decaying Fourier transforms, the latter is not feasible by simply solving the Fourier integral but requires representative notations such as, in the example of the Yukawa potential, in terms of derivatives of the Dirac delta function. This subject will be addressed in more detail in the direct calculation of u^{-1} in Chapter 5.

4

FTS AND MD: AN IMPOSED INVERSE POTENTIAL

No man can think, feel, will, nor even dream,
without everything being defined, conditioned,
limited, directed by a goal which floats before him.
— Alfred Adler

Field-theoretic simulations are not meant to be used as a substitute for molecular dynamics simulations. In view of the inverse potential problem discussed in Section 2.4, a major reason for this is the difficulties associated with inverting the non-bonded particle interactions. In fact, the simplicity of the underlying physical model is one of the most defining characteristics of the FTS framework compared to particle-based methods. It so happens that for polymer models of continuous or discrete chains, practically the entirety of the related FTS studies consider either exclusively simple on-contact interactions or, at best, Coulomb-like ones (leaving aside their masked versions). An argument in favor of this is that atomic details become less and less relevant at larger length scales. For example, according to Ref. [64], interactions between neutrons seem to be well described by on-contact δ-interactions. Of course, polymer chains are not built by neutrons and the presence of van der Waals forces, for instance, may significantly shape many of their properties.[1] Clearly, atomic-level features cannot be resolved by the relatively simple models used in FTS, thus necessitating in some cases calibration of the model parameters; a typical example is the Flory χ-parameter often employed to correctly predict order-disorder transitions in polymers [89]. This missing direct connection to the chemistry [24] severely limits the predictive capabilities of these phenomenological field-based models.

On the other hand, there are circumstances (for example, very dense systems) where particle simulations rapidly reach their limits and the physical system studied may be better approached by a field-based method. In that case, it would be desirable if the field-based model could keep as much as possible of the richness of interactions included in the corresponding particle-based model. Motivated by this, the current chapter borrows material from the published work in Ref. [84] to show how, in general, field-theoretic simulations can be connected to other frameworks or methods, in particular, how a direct interplay between FTS and MD (both operating on an equal level of description) can be conceptualized.

To enable such an interplay, the key idea exploited here is not to directly invert the pair potential for use in the field-theoretic model but instead to deduce indirectly an inverse potential that is consistent

1 A neat demonstration of this can be found, for example, in Ref. [97], a paper not associated with this dissertation. In it, the formation of microphase separations in polyelectrolytes is compared for systems with and without the presence of van der Waals forces.

with the model equations and simultaneously is guaranteed to generate the correct molecular structure. This approach allows for more flexibility in dealing with the corresponding mathematical structure and, in addition, helps to preserve in the field description the details of the corresponding interatomic interactions. First, Section 4.1 presents an example of a simple but realistic molecular system, liquid argon, and provides a meaningful parametrization of the interactions involved in terms of a Morse potential. A suitable field-theoretic formulation for this system is given in Section 4.2. How the inverse potential for this system can be inferred from MD simulations is formally presented in Section 4.3. The corresponding numerical method and the results obtained are shown in Section 4.4. The chapter concludes with Section 4.5 discussing the opportunities opened by having computed u^{-1} as well as some limitations of the method followed, such as the transferability of the computed inverse potential to other thermodynamic conditions.

4.1 LIQUID ARGON – A REAL-WORLD EXAMPLE OF A MONATOMIC FLUID

In classical theoretical textbooks on molecular theories of liquids such as Reference [19], the noble gas argon is a popular choice of study. It is chemically inert under most practical conditions, and relatively easy to isolate from the atmosphere typically in monatomic form.[2] The latter property of being monatomic renders it particularly attractive also in the context of this dissertation and the methods of study that will be developed. Argon has been well studied experimentally over the years, and extensive reports have been presented already since the early 1970s such as that by Yarnell and co-workers [98] on its molecular structure in the liquid state and how experimental data compare with a simple molecular dynamics simulation (cf. Ref. [99]). What Yarnell et al. did was to perform neutron scattering experiments to deduce a (corrected) static structure factor from the raw experimental data. As demonstrated in detail in Appendix A.3 (see Eq. (A.3.15)) of this thesis, the static structure factor S and the radial distribution function g form a Fourier pair (up to a constant prefactor):

$$\rho_0 \, \mathcal{F}[g-1](\boldsymbol{k}) = S(\boldsymbol{k}) - 1. \tag{4.1}$$

This relation [98] is particularly useful since S can be experimentally measured by scattering experiments, whereas g is accessible through particle simulations. So the above Fourier transform can be used to go from one quantity to the other.

In Ref. [98], a parametrization of the 12-6 Lennard-Jones (LJ) potential

$$u_{\mathrm{LJ}}(r) = 4\epsilon_{\mathrm{LJ}} \left(\left(\frac{\sigma}{r}\right)^{12} - \left(\frac{\sigma}{r}\right)^{6} \right) \tag{4.2}$$

2 A listing of the thermophysical properties of argon can be found here, for example: Engineering ToolBox, (2008). *Argon - Thermophysical Properties*. [online] Available at: https://www.engineeringtoolbox.com/argon-d_1414.html [Accessed July 2022].

has also been presented that is compatible with the experimental data. The LJ potential of Eq. (4.2) is composed of a repulsive part ($\propto r^{-12}$) that dominates at short interatomic distances and an attractive part ($\propto r^{-6}$) that in turn is dominant at large distances r. The separation between these regions is given by the potential minimum at $r = 2^{1/6}\sigma$; the mathematical form of the attractive interactions is motivated by that of van der Waals forces, whereas the form of the repulsive interactions describing Pauli repulsion is chosen as such mainly for reasons of better practicability (i.e. $r^{-12} = (r^{-6})^2$). Because of its monatomic nature and inert character, the above Lennard-Jones potential is an ideal model to describe liquid argon. The corresponding energy and length parameters are reported in the work by Yarnell et al.:

$$\epsilon_{\mathrm{LJ}}/k_B = 119.8\,\mathrm{K}, \tag{4.3}$$

$$\sigma = 3.405\,\text{Å}. \tag{4.4}$$

Unfortunately, the 12-6 Lennard-Jones potential as given by Eq. (4.2) is not suitable for use in related field-theoretic models because of its behavior at $r = 0$ (see also Ref. [64]). As a solution, this work adopts the Morse potential

$$u_{\mathrm{Morse}}(r) = \epsilon\Big(\exp\left(-2\xi\left(r - r_{\mathrm{min}}\right)\right) - 2\exp\left(-\xi\left(r - r_{\mathrm{min}}\right)\right)\Big), \tag{4.5}$$

with the positive Morse parameters ϵ, r_{min}, and ξ, for use in field-theoretic models, which is also widely used in particle simulations as an alternative to the 12-6 Lennard-Jones one. Similarly to the 12-6 Lennard-Jones potential, the Morse one contains a repulsive and an attractive component; however, the Morse potential assumes a finite value at $r = 0$. In the literature, Morse parameters for argon can be found in Ref. [100], albeit for the gas phase:

$$\epsilon^{(1)}/k_B = 118.1\,\mathrm{K}, \tag{4.6}$$

$$r_{\mathrm{min}}^{(1)} = 4.13\,\text{Å}, \tag{4.7}$$

$$\xi^{(1)} = 1.253\,\text{Å}^{-1}. \tag{4.8}$$

An alternative approach has been presented in Ref. [101], where the Morse parameters were obtained based on a fitting approach from the corresponding Lennard-Jones ones according to the following relations:

$$\epsilon^{(2)} = \epsilon_{\mathrm{LJ}}, \tag{4.9}$$

$$r_{\mathrm{min}}^{(2)} = 2^{1/6}\sigma, \tag{4.10}$$

$$\xi^{(2)} = \frac{6}{r_{\mathrm{min}}}. \tag{4.11}$$

To test which of the above set of parameters better describes the structure of liquid argon, molecular dynamics simulations[3] were performed in this thesis and the resulting $g(r)$'s were compared to the

3 The MD simulations are conducted using the "Extensible Simulation Package for Research on Soft Matter" (ESPResSo) (see Ref. [102]).

corresponding one from Ref. [98]. Following Ref. [98], the MD simulations were performed in the canonical (n, V, T) ensemble. For this purpose, the bulk density was set to $\rho_0 = 0.021\,38\,\text{Å}^{-3}$ and the temperature was fixed to $T = 86.56\,\text{K}$ using a Langevin thermostat. The original MD simulation of the LJ fluid was also repeated as a validation test and the calculated RDF, shown as the "Reference" curve in Fig. 4.1a, is observed to be consistent with the corresponding RDF reported in Ref. [98]. In addition to the RDF from the LJ fluid, that from the Morse fluid was also determined and shown in Fig. 4.1a: once with the parameters from Eqs. (4.6)-(4.8) which is labeled as "Morse 1" and once with the parameters from Eqs. (4.9)-(4.11) which is labeled as "Morse 2". To complement the RDF, Fig. 4.1b shows the static structure factor $S(k)$ as calculated by the relation in Eq. (4.1) from $g(r)$. Concerning the $S(k)$ of Fig. 4.1b, it should be noted that

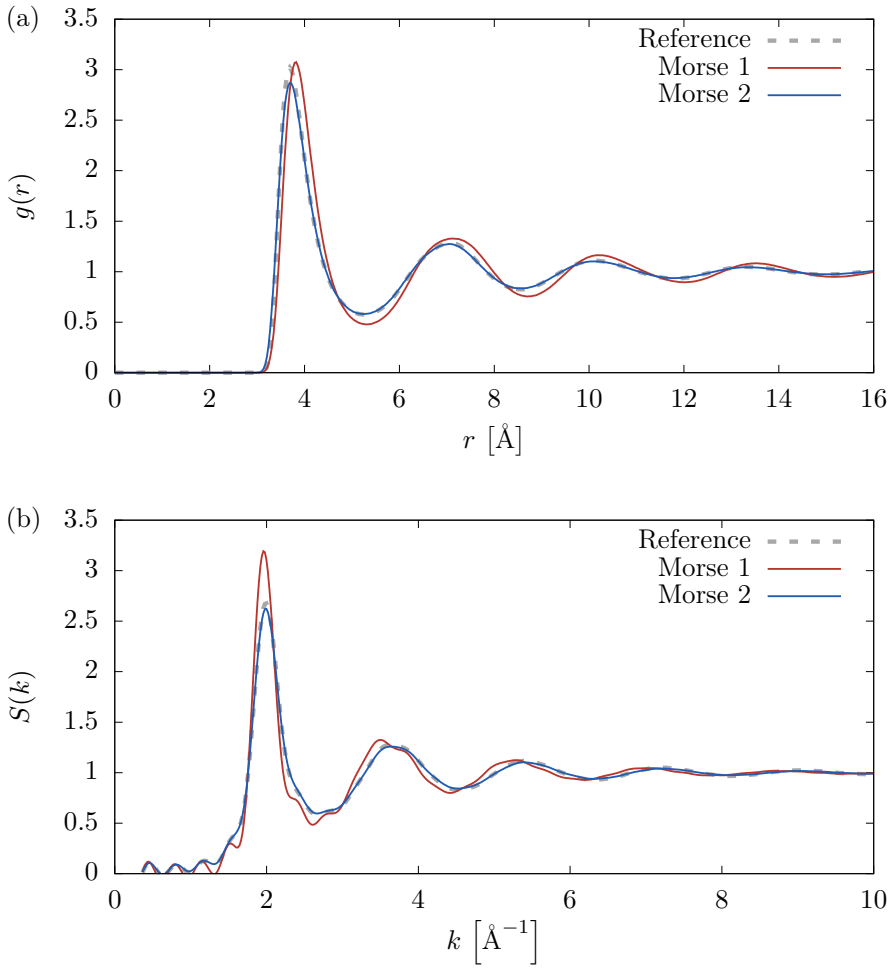

FIGURE 4.1: (a) Radial distribution function $g(r)$ from MD simulations and (b) the static structure factor $S(k)$ derived by Fourier transformation for a Lennard-Jones fluid (denoted "Reference") in comparison to two differently parameterized Morse fluids. The exact values of the simulation parameters are given in the text.

the small oscillations that occur for $k \lessapprox 2\,\text{Å}^{-1}$ are artifacts caused by the finite box size of the simulation domain and the resulting trunca-

tion of $g(r)$. In direct comparison with the reference simulation, the fitted "Morse 2" parameters lead to better agreement than the "Morse 1" parameters taken from Ref. [100]. Based on this comparison, in the remainder of this chapter, the parameters calculated according to Eqs. (4.9)-(4.11) have been used for the Morse potential.

4.2 A HYBRID MODEL FOR STUDYING DENSITY PROFILES

Although quantities such as the static structure factor can be derived from field-based observables in the field-theoretic framework, a modified yet simple monatomic fluid model shall be presented here to allow for directly accessing certain structural properties. More precisely, this model is created with the sole intention of studying the distribution of particles around a probe particle depending on the choice of interparticle interactions. This setup, applied in similar form in Refs. [53, 56], has the advantage that, by considering the density distribution around a tagged particle, the connection to the radial distribution function becomes almost immediately apparent.

The underlying idea is not to apply the particle-to-field transformation to all n particles but to exclude one of them, say the n-the particle, thus leading to a hybrid model which, in addition to the continuous auxiliary field(s), also contains degrees of freedom (here the coordinates) of the non-transformed particles. With the intention to exclude the n-th particle, the microscopic density of the monatomic fluid from Eq. (2.2) is written as

$$\hat{\rho}(\boldsymbol{r}) = \hat{\rho}'(\boldsymbol{r}) + \delta(\boldsymbol{r} - \boldsymbol{r}_n) \tag{4.12}$$

with the microscopic density of the remaining $n-1$ particles being

$$\hat{\rho}'(\boldsymbol{r}) := \sum_{i=1}^{n-1} \delta(\boldsymbol{r} - \boldsymbol{r}_i). \tag{4.13}$$

With this notation, the interaction term (which will be subjected to the transformation) is expressed as

$$\frac{1}{2}\langle\hat{\rho}|u|\hat{\rho}\rangle = \frac{1}{2}\langle\hat{\rho}'|u|\hat{\rho}'\rangle + \sum_{i=1}^{n-1} u(\boldsymbol{r}_i - \boldsymbol{r}_n) + \frac{1}{2}u(\boldsymbol{0}) \tag{4.14}$$

for the symmetric pair potential $u(\boldsymbol{r}) = u(-\boldsymbol{r})$. To obtain the RDF as straightforwardly as possible from the density distribution around the probe particle, the n-th particle is chosen to be located at the origin of the coordinate system, $\boldsymbol{r}_n = \boldsymbol{0}$. This fixing of the probe particle is considered in the canonical partition function by writing this as follows:

$$\mathcal{Z}_c\Big|_{\boldsymbol{r}_n=\boldsymbol{0}} = z_0 \int_{V^n} \mathrm{d}^{3n}r \, \exp\left(-\beta U\right) \delta(\boldsymbol{r}_n - \boldsymbol{0}). \tag{4.15}$$

Using the interaction term given by Eq. (4.14) in U (defined by Eq. (2.4)) and applying the Gaussian integral identity to transform the microscopic density $\hat{\rho}'$ finally leads to the following field-theoretic Hamiltonian

$$\mathcal{H}^{(\mathrm{HPF})}[w] = \frac{1}{2\beta}\left\langle w\middle|u^{-1}\middle|w\right\rangle - (n-1)\ln Q^{(\mathrm{HPF})}[iw] \tag{4.16}$$

for this hybrid particle-field model. The hybrid character of the model is most evident in the reduced partition function:

$$Q^{(\mathrm{HPF})}[iw] = \frac{1}{V}\int_V \mathrm{d}^3 r\ \exp\left(-\beta u(\boldsymbol{r}) - iw(\boldsymbol{r})\right). \tag{4.17}$$

Besides the original form (Eq. (2.12) with $J = 0$), $Q^{(\mathrm{HPF})}$ contains the pair potential u in the exponent brought up by the second term in Eq. (4.14) containing the sum, formally representing the interaction of the field model with the probe particle. Analogous to the procedure described in Section 2.2, a field-based density observable associated with the microscopic density $\hat{\rho}'$ can then be derived as

$$\tilde{\rho}(\boldsymbol{r}) = \frac{n-1}{V}\exp\left(-\beta u(\boldsymbol{r}) - iw(\boldsymbol{r}) - \ln Q^{(\mathrm{HPF})}[iw]\right). \tag{4.18}$$

Concerning this density observable, a simplification shall be motivated. It can be seen that the prefactor of the exponential function corresponds to the value of the bulk density which is approximated by $\tilde{\rho}$ (in the ensemble mean) for large absolute values of $\boldsymbol{r}$. For physically relevant systems, it is to be assumed that this bulk density is not appreciably affected by the presence of a single probe particle, so that $\rho_0 = n/V \approx (n-1)/V$ holds and thus

$$\tilde{\rho}(\boldsymbol{r}) \approx \rho_0\ \exp\left(-\beta u(\boldsymbol{r}) - iw(\boldsymbol{r}) - \ln Q^{(\mathrm{HPF})}[iw]\right) \tag{4.19}$$

appears to be a reasonable approximation. Moreover, different contributions to the density observable of the hybrid model can be identified and intuitively understood from a thermodynamic perspective:[4] Besides $\ln Q^{(\mathrm{HPF})}$, which may be interpreted as a thermodynamic potential, $\tilde{\rho}(\boldsymbol{r})$ has two other contributions, one from the direct intermolecular potential $u(\boldsymbol{r})$ and a second from $iw(\boldsymbol{r})$ playing the role of a chemical potential spatially resolved around the probe particle. The subtle mechanism[5] by which damped oscillations may arise in the density profile around the probe particle can then be understood from this perspective as the result of an interplay between individual competing interactions.[6]

The particular advantage of this hybrid particle-field model is the notably simple relation between the density observable and the radial distribution function. Because $g(r)$ is defined by integration of the two-particle distribution function, see Eq. (A.3.1), in case of the present model, the RDF can simply be calculated from the rescaled average density distribution around the fixed particle as

$$g(r) = \frac{\langle\tilde{\rho}(r)\rangle}{\rho_0} \tag{4.20}$$

4 I would like to thank Hans Christian for pointing this out to me and for continuously making me realize the tremendous insights that come from a thermodynamic perspective.

5 The "subtle mechanism" was termed and brought up by Hans Christian.

6 Of course, for purely repulsive systems, the distribution of particles (i.e., the density) must be constrained in some way for such oscillations to occur in the density profile.

assuming an isotropic system, i.e. $\langle\tilde{\rho}(\boldsymbol{r})\rangle = \langle\tilde{\rho}(r)\rangle$. This result seems particularly important because, as shown in Sec. 4.1, $g(r)$ can be easily obtained by, for example, particle-based simulations, thus providing a straightforward connection between these methods and the field-theoretic model.

4.3 INFERENCE AND USE OF AN IMPOSED INVERSE POTENTIAL

The central idea in this chapter as an overcoming of the inverse potential problem relies heavily on employing a given density distribution in the field-theoretic model under the condition that the model equations remain valid. A fundamental consideration in designing the approach as also presented in Ref. [84] is significantly influenced by the work of Koski and co-workers [56]. What seems so interesting about Koski's work in this context are the encouraging results of an RDF $g(r)$ presented for a similar hybrid particle-field model. In particular, excellent agreement was demonstrated for radial distribution functions (synonymous with the "pair distribution function" term used in Ref. [56]) obtained by particle-based Monte Carlo simulations and by field-theoretic simulations performed both for fully fluctuating fields using complex Langevin dynamics and for the saddle-point approximation (cf. Fig. 1 in [56]). The success of the saddle-point approximation to describe (under appropriate conditions discussed in Section 2.3) density distributions with the desired accuracy for a hybrid particle-field model, motivated the use of the same approximation also in this work. Consequently, the average density profile $\langle\rho(\boldsymbol{r})\rangle$ is approximated by the saddle-point density $\rho^*(\boldsymbol{r})$ (cf. Eq. (2.39)), which corresponds to the density observable from Eq. (4.19) with the saddle-point solution $w^*(\boldsymbol{r})$ inserted (cf. Eq. (2.36)). The saddle-point solution $w^*(\boldsymbol{r})$, however, shall not be derived from the saddle-point equation (2.34) but instead be deduced from a given density profile obtained from another, independent method.

In this regard, it is instructive to write the saddle-point density using Eqs. (4.17) and (4.19) as

$$\rho^*(\boldsymbol{r}) = \rho_0 V \frac{\exp\left(-\beta u(\boldsymbol{r}) - i w^*(\boldsymbol{r})\right)}{\int_V \mathrm{d}^3 r \;\exp\left(-\beta u(\boldsymbol{r}) - i w^*(\boldsymbol{r})\right)}. \tag{4.21}$$

From this equation it is straightforward to note that if $w^*(\boldsymbol{r})$ is a solution of $\rho^*(\boldsymbol{r})$, then $w^{*\prime}(\boldsymbol{r}) = w^*(\boldsymbol{r}) + \text{const.}$ is also a solution. The arbitrary constant, however, is fixed by the value of $Q^{(\mathrm{HPF})}$ from Eq. (4.17). For this reason, the field configuration

$$w_Q^*(\boldsymbol{r}) = i\beta u(\boldsymbol{r}) + i \ln\left(\rho^*(\boldsymbol{r})/\rho_0\right) + i \ln Q^{(\mathrm{HPF})}, \tag{4.22}$$

being the solution of Eq. (4.21) for a given $\rho^*(\boldsymbol{r})$ and under the constraint of Eq. (4.17), is labeled with a Q subscript. Starting from the functional derivative

$$\frac{\delta \mathcal{H}^{(\mathrm{HPF})}[w]}{\delta w(\boldsymbol{r})} = \frac{1}{\beta}\left[u^{-1} * w\right](\boldsymbol{r}) + i\tilde{\rho}(\boldsymbol{r}), \tag{4.23}$$

the second step is to employ the saddle-point equation

$$\frac{1}{\beta}\left[u_Q^{-1} * w_Q^*\right](\boldsymbol{r}) + i\rho^*(\boldsymbol{r}) = 0 \tag{4.24}$$

to calculate the inverse potential u_Q^{-1} by deconvolution given the known w_Q^* and ρ^* profiles. For this, the application of the convolution theorem and thus the calculation of u_Q^{-1} in Fourier space seems natural. The specific conditions under which such a deconvolution may be performed shall be discussed in Section 4.4 by means of a particular use case. However, it turns out that the deconvolution of Eq. (4.24) is relatively unproblematic to handle, in contrast to the already discussed deconvolution of Eq. (3.20) due to the challenges associated with a non-decaying Fourier transform in Eq. (3.21). Third, by exploiting the saddle-point equation, a value for $Q^*(n, V, T)$ has to be found such that the corresponding u_Q^{-1} function defines an inverse potential which is independent of the thermodynamic state variables. This is accomplished by integrating Eq. (4.24) to obtain the expression

$$\frac{1}{\beta}\int_V u_Q^{-1}(\boldsymbol{r})\mathrm{d}^3r\ \left(\frac{1}{iV}\int_V w_1^*(\boldsymbol{r})\mathrm{d}^3r\ + \ln Q^{(\mathrm{HPF})}\right) + \rho_0 = 0. \tag{4.25}$$

For large volumes and a sufficiently fast decaying u, the first term in parentheses vanishes, thus it can be found that

$$\int_V \mathrm{d}^3r\ u_Q^{-1} = -\frac{\beta\rho_0}{\ln Q^{(\mathrm{HPF})}}, \tag{4.26}$$

and then the saddle-point solution of $Q^{(\mathrm{HPF})}$ is

$$Q^* = \exp\left(-\zeta\beta\rho_0\right), \tag{4.27}$$

where $\zeta := \left(\int_V \mathrm{d}^3r\ u_{Q^*}^{-1}(\boldsymbol{r})\right)^{-1} \equiv \int_V \mathrm{d}^3r\, u(\boldsymbol{r})$ as motivated by Eq. (3.21) for $\boldsymbol{k} = \boldsymbol{0}$.

On the basis of the saddle-point approximation, the inverse potential thus obtained would in principle offer itself for use in further field-theoretic simulations conducted at different thermodynamic state points. Within the scope of this discussion, the study of these states shall be based on the saddle-point approximation as well. As described in Section 2.3, it is common in such stand-alone saddle-point (i.e., SCFT) calculations to find the saddle point via relaxation dynamics by applying a relaxation equation (cf. Eq. (2.46)). Accordingly, and motivated by the complex Langevin equation in the absence of fluctuations (cf. Eq. (2.43)), the following relaxation equation

$$\frac{\partial w(\boldsymbol{r}, t)}{\partial t} = -\lambda_w \frac{\delta\mathcal{H}^{(\mathrm{HPF})}[w]}{\delta w(\boldsymbol{r}, t)}, \tag{4.28}$$

is applied in this chapter, with λ_w being the relaxation parameter and t the fictitious time. It shall be noted, however, that in the literature [40] other iterative approaches such as the Anderson mixing scheme [103–105] are used as an alternative and effective way to perform saddle-point calculations.[7] As discussed in the context of the

7 I would like to thank the anonymous reviewer of Ref. [84] for pointing this out.

saddle-point approximation in Section 2.3, a comparison of different methods can be found in Ref. [77].

In test computations preceding the numerical studies presented in Section 4.4, the exclusive application of Eq. (4.28) for relaxation indicated an inefficient (meaning slow) convergence of $Q^{(\mathrm{HPF})}$ toward Q^*. Although the scheme drives w to a saddle-point solution that is consistent with Q^*, the relaxation of the density field $\tilde{\rho}$ toward ρ^* occurs much faster than the adjustment of the offset in w to approach Q^*. One option to overcome this and to speed up the relaxation process would be an instantaneous correction of the $Q^{(\mathrm{HPF})}$ value. This would correspond to shifting the field configuration $w(\boldsymbol{r}, t)$ at instantaneous time t so that its offset is aligned with the targeted, yet unknown, saddle-point configuration $w^*(\boldsymbol{r})$. Taking into account the definition of $Q^{(\mathrm{HPF})}$ from Eq. (4.17), such a shift could be accomplished by replacing the instantaneous field configuration at time t by

$$w'(\boldsymbol{r}) = w(\boldsymbol{r}) + i \ln \frac{Q^*}{Q^{(\mathrm{HPF})}[iw]}. \tag{4.29}$$

However, such a procedure appears to cause a rather strong interference to the relaxation dynamics which might not be desirable in general. As a less strict formulation, and by analogy with the relaxation equation for the w field (Eq. (4.28)), a similar dynamics for $\ln Q^{(\mathrm{HPF})}$ is proposed:

$$\frac{\partial \ln Q^{(\mathrm{HPF})}}{\partial t} = -\lambda_Q \ln \frac{Q^{(\mathrm{HPF})}[iw]}{Q^*} \tag{4.30}$$

with λ_Q playing the role of a control parameter for this extended relaxation scheme.

For the practical implementation of this extended relaxation scheme, the fields are first discretized on a regular grid with M^3 grid points. Since it seems natural to compute the Fourier transforms by the numerically efficient fast Fourier Transform (FFT) algorithm, periodic boundary conditions are automatically imposed on the cubic simulation domain having a volume V described by this regular grid. For the algorithmic implementation of Eqs. (4.28) and (4.30), their time evolution is solved using the simple forward Euler method resulting in the following equations:

$$w_l^{(N+1/2)} = w_l^{(N)} - \lambda_w \Delta t \frac{\delta \mathcal{H}^{(\mathrm{HPF})}[w]}{\delta w(\boldsymbol{r}_l, t^{(N)})}, \tag{4.31}$$

$$\ln Q^{(\mathrm{HPF})(N+1)} = \ln Q^{(\mathrm{HPF})(N)} - \lambda_Q \Delta t \left(\ln Q^{(\mathrm{HPF})(N+1/2)} - \ln Q^* \right), \tag{4.32}$$

$$w_l^{(N+1)} = w_l^{(N+1/2)} + i \ln Q^{(\mathrm{HPF})(N+1)} - i \ln Q^{(\mathrm{HPF})(N+1/2)}, \tag{4.33}$$

where the discrete grid coordinate $\boldsymbol{r}_l$, $w_l^{(N)} := w(\boldsymbol{r}_l, t^{(N)})$, and $\ln Q^{(\mathrm{HPF})(N)} := \ln Q^{(\mathrm{HPF})}[iw]\big|_{t=t^{(N)}}$ have been introduced. From the known field configuration $w_l^{(N)}$, and from this the computed

$\ln Q^{(\mathrm{HPF})(N)}$ value in the N-th step, Eq. (4.31) is first used to calculate $w_l^{(N+1/2)}$ and from it $\ln Q^{(\mathrm{HPF})(N+1/2)}$. Next, the target value of $\ln Q^{(\mathrm{HPF})(N+1)}$ at the $(N+1)$-th step is pre-calculated according to the relaxation scheme (Eq. (4.30)) using Eq. (4.32). Lastly, all these quantities are used in Eq. (4.33) to bring the field $w_l^{(N+1/2)}$ in agreement with the pre-calculated value $\ln Q^{(\mathrm{HPF})(N+1)}$, thus yielding the field values $w_l^{(N+1)}$ at the next iteration step.

A final aspect that appears important in inferring and using the inverse potential is connected with the case of vanishing density fields at small intermolecular distances. Eq. (4.22), in particular, is quite helpful for understanding that field-theoretic models discussed here show divergences at the points where the density field vanishes, i.e., when $\rho^*(\boldsymbol{r}) = 0$. From a physical point of view, local displacements of the density field are associated with the presence of strong repulsive interactions, a common difficulty when considering hard-core potentials for use in field-theoretic models. This consideration is equally appealing because it provides an intuitive understanding to the problem of ultraviolet divergences in field-theoretic models with divergent repulsive interactions. For the Edwards model, for example, this has motivated its Gaussian-regularized version (the GREM from Ref. [92]), in which the microscopic density field is replaced by a smeared one, effectively exchanging the pair potential that diverges at $r = 0$ with a soft Gaussian potential (cf. Chapter 3). In contrast, a regularization of the density field is proposed here. More precisely, the problem of divergences occurring in the w^* field is circumvented by constraining ρ^* to be strictly positive. In general, the exact value of very small densities is dictated by the accuracy with which the corresponding computational method samples the phase space. A *minimum density constraint* is proposed here as a simple solution, by adjusting the density in regions where it appears to vanish due to numerical accuracy reasons. In such a regularization, two cases can be distinguished depending on whether the inverse potential is derived or used in standalone simulations. In the former, ρ^* is imposed externally by replacing the density as follows:

$$\rho'^*(\boldsymbol{r}) = \begin{cases} \rho^*(\boldsymbol{r}) & \text{if } \rho^*(\boldsymbol{r}) \geq \rho_{\min}, \\ \rho_{\min} & \text{if } \rho^*(\boldsymbol{r}) < \rho_{\min}, \end{cases} \tag{4.34}$$

where $\rho_{\min} \ll \rho_0$ is an externally imposed density value close to zero. In the latter, an already known inverse potential is used in a standalone computation, the field w is adapted to satisfy the minimum density constraint, and similar to Eq. (4.34) the density field observable $\tilde{\rho}(\boldsymbol{r})$ is replaced by a hypothetical $\tilde{\rho}'(\boldsymbol{r})$. In contrast to the first case, however, the density is not replaced directly, but instead the desired $\tilde{\rho}'(\boldsymbol{r})$ is reconstructed from $w'(\boldsymbol{r})$ while keeping the value of $\ln Q^{(\mathrm{HPF})}$

unchanged.[8] Proceeding from Eq. (4.22), it is thus straightforward to find

$$w'(\boldsymbol{r}) = \begin{cases} w(\boldsymbol{r}) & \text{if } w(\boldsymbol{r}) \geq w_{\min}(\boldsymbol{r}), \\ w_{\min}(\boldsymbol{r}) & \text{if } w(\boldsymbol{r}) < w_{\min}(\boldsymbol{r}), \end{cases} \tag{4.35}$$

with $w_{\min}(\boldsymbol{r}) = i\beta u(\boldsymbol{r}) + i \ln(\rho_{\min}/\rho_0) + i \ln Q^{(\mathrm{HPF})}$.

4.4 NUMERICAL STUDIES USING THE MORSE POTENTIAL

In this section, the previous parts of this chapter shall be brought together to derive an inverse potential based on a practically motivated example. To this, the Morse potential is used with the parametrization given in Section 4.1 by Eqs. (4.9)–(4.11) based on the structural properties of liquid argon. As already discussed, the choice of the Morse potential is motivated by the fact that the 12-6 Lennard-Jones one, see Eq. (4.2), is not suitable for use in field-theoretic models.

To calculate the inverse potential u_Q^{-1} by solving Eq. (4.24) in Fourier space, it is essential that the Fourier transform of w_Q^* from Eq. (4.22) and hence of u exists. In the case of the Morse potential, the hybrid particle-field model is fully radially symmetric, i.e., $\rho^*(\boldsymbol{r}) = \rho^*(r)$, and the radial Fourier transform of the potential is found to be

$$\hat{u}_{\mathrm{Morse}}(k) = 16\pi\epsilon\xi \exp(r_{\min}\xi) \left(\frac{\exp(r_{\min}\xi)}{(k^2 + 4\xi^2)^2} - \frac{1}{(k^2 + \xi^2)^2} \right). \tag{4.36}$$

This Fourier transform is positive for all wavenumbers k under the condition that $\xi > \frac{4\ln 2}{r_{\min}}$ which is satisfied by Eq. (4.11) for all values of the underlying ϵ_{LJ} and σ parameters. This is significant because it guarantees that u is positive-definite, as was analyzed in Chapter 2. Moreover, the condition that the Fourier transform $\hat{w}_Q^*$ be a positive and sufficiently slowly decaying function for positive k is ensured by the choice of the Morse parameters.

The corresponding radial distribution function required for the derivation of u_Q^{-1} is determined by a molecular dynamics simulation. Considering that the hybrid field-theoretic model is formulated in the canonical ensemble, the MD simulations are also conducted in the (n, V, T) ensemble. For a desired density ρ_0, the temperature in the MD simulation is fixed at its reference value T using a Langevin thermostat. The time average of the radial distribution function $\langle g_{\mathrm{MD}}(r) \rangle_t$ from the simulations is then used to approximate the ensemble average of the density from the field theory as

$$\langle \tilde{\rho}(r) \rangle \approx \rho_0 \langle g_{\mathrm{MD}}(r) \rangle_t . \tag{4.37}$$

For later comparison with stand-alone field-theoretic calculations, a series of MD simulations are performed at different state points.

8 To preserve model consistency (i.e., not to change model parameters indirectly), this procedure implies a sufficiently small $\rho_{\min}$ so that $\frac{1}{V}\int_V \mathrm{d}^3 r\, \tilde{\rho}'(\boldsymbol{r}) \approx \rho_0$ remains unaffected.

The $\langle g_{\mathrm{MD}}(r)\rangle_t$ is calculated at a target pressure of $P = 100\,\mathrm{atm}$, where the system is expected to be in the liquid state over a relatively wide range of temperatures. The bulk densities ρ_0 listed in Table 4.1 for

T (K)	ρ_0 (Å^{-3})
70	0.021560
80	0.020597
90	0.019545
100	0.018367

TABLE 4.1: Bulk densities ρ_0 from MD simulations at pressure $P = 100\,\mathrm{atm} \pm 1\,\%$ and various temperatures T.

the indicated temperatures $T = 70, 80, 90$, and $100\,\mathrm{K}$ are found by an iterative scheme given the target pressure. The MD-predicted radial distribution functions for these temperatures are shown in Fig. 4.2. The strong atomic repulsion inherent in the Morse potential at small

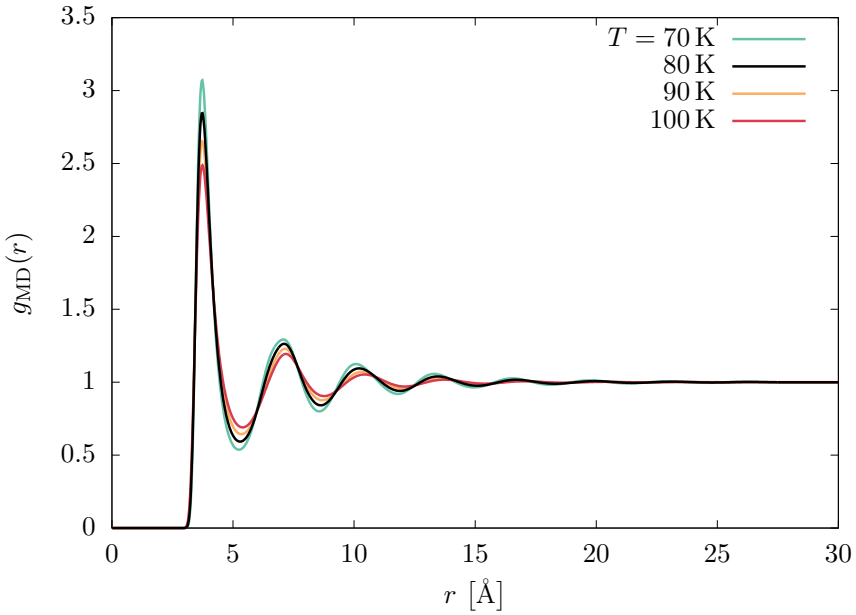

FIGURE 4.2: Radial distribution functions from MD simulations with the Morse fluid conducted at various temperatures ($P = 100\,\mathrm{atm}$, T and ρ_0 from Table 4.1).

distances is particularly evident in the $g_{\mathrm{MD}}(r)$ curves shown in the figure.[9] These repulsive interactions lead to an excluded volume effect and the associated vanishing density at small intermolecular distances necessitates the density regularization discussed in Section 4.3. On the other hand, Fig. 4.2 shows that the local density approaches its bulk value (corresponding to g_{MD} equal to 1) at large distances. Besides, the behavior of $g_{\mathrm{MD}}(r)$ indicates the minimum size of the sim-

9 For brevity and as is common, $g_{\mathrm{MD}}(r)$ here refers to a distribution that has been averaged over many configurations over simulation time (after the system has undergone an initial equilibration stage). Only for the sake of clarity, the time average $\langle g_{\mathrm{MD}}(r)\rangle_t$ is explicitly written out in Eq. (4.37).

ulation domain in the field-theoretic simulations so that such structures in the local density can be reproduced. Accordingly, a generously dimensioned volume $V = 96 \times 96 \times 96\,\text{Å}^3$ of a cubic simulation box is chosen with the simulation domain being discretized using a regular grid (cf. Section 4.3) with $M^3 = 384^3$ grid points in total.

For this numerical setup, first the imposed inverse potential is inferred from the $g_{\text{MD}}(r)$ curve at $T = 80\,\text{K}$ following the algorithm presented in Section 4.3. This temperature choice seems particularly suitable to describe the model system (argon) in the liquid state. A plot of the inferred inverse potential is shown in Fig. 4.3. In the $u^{-1}(r)$ curve,

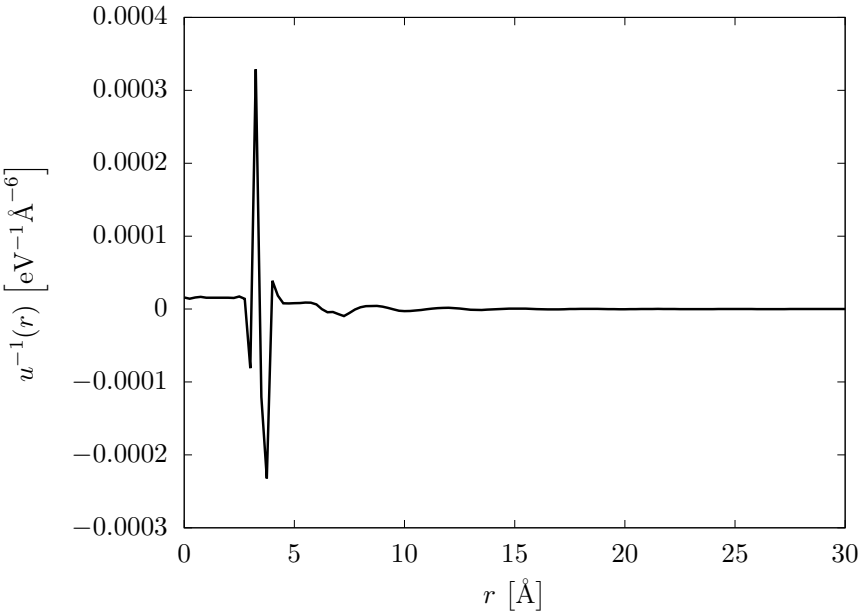

FIGURE 4.3: Inverse potential inferred from the MD-computed radial distribution function (see Fig. 4.2) at $T = 80\,\text{K}$.

significant structure is manifested at distances between 2.7 and 15 Å, the range in which the $g_{\text{MD}}(r)$ curve also exhibits its characteristic fluid-like structure. At larger distances, u^{-1} approaches zero which is understandable given that its volume integral is finite. The behavior is particularly distinctive at distances between 3 and 5 Å, where two main peaks of opposite sign are observed along with two minor ones on their left and right, reminiscent of derivatives of a delta function. It is also pleasing to note that the root of u^{-1} between the two main peaks coincides with the underlying Lennard-Jones σ parameter (Eq. (4.4)).

The inverse potential shown in Fig. 4.3, computed through an inexpensive MD simulation, is then employed in stand-alone field-based simulations to relax a randomly chosen initial field configuration[10] toward the saddle-point solution by using the relaxation scheme described in Section 4.3. The relaxation behavior of the field model can

10 Since the saddle-point approximation assumes a purely imaginary w^*, only the imaginary part of w is considered in the implementation for reasons of numerical efficiency. Nevertheless, the relaxation dynamics is generally not limited to this case and other initial conditions with non-vanishing real and imaginary parts are equally conceivable.

be examined and understood intuitively by looking at the convergence of the density observable $\tilde{\rho}$ toward the saddle-point solution ρ^*. As a quantitative measure of the rate of the relaxation process, the following root-mean-square deviation (RMSD) is introduced

$$\mathrm{RMSD}(t) := \sqrt{\frac{1}{M'} \sum_{l=1}^{M'} \left(\tilde{\rho}(\boldsymbol{r}_l, t) - \rho^*(\boldsymbol{r}_l)\right)^2}, \tag{4.38}$$

specifying the deviation of the density observable $\tilde{\rho}$ at instantaneous time t from the targeted (and, in this case, known) saddle-point solution ρ^* over all space points although it is conceivable that one could define several RMSDs to quantify deviations at specific domains of interest. As discussed when introducing the regular grid in Section 4.3, continuous functions (such as the density field here) are discretized with $\boldsymbol{r}_l$ denoting the position of a grid point. When calculating the RMSD according to Eq. (4.38), however, it should be sufficient to restrict the summation to the M' grid points located on the positive z-axis inside the simulation box. The time evolution of this RMSD

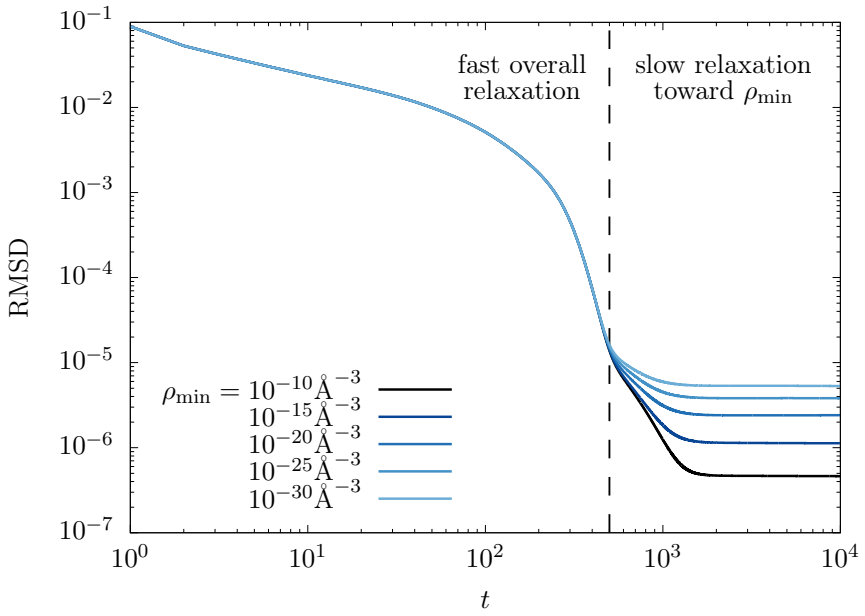

FIGURE 4.4: Time evolution of the root-mean-square deviation (RMSD) of the density observable $\tilde{\rho}$ from the targeted imposed saddle-point density ρ^* at $T = 80\,\mathrm{K}$.

is shown in Fig. 4.4 for different values of the minimum density parameter $\rho_{\min}$. As indicated in the plot, the relaxation from $\tilde{\rho}$ toward ρ^* occurs in two stages. The first stage is nicely illustrated in Fig. 4.5 through the density observable $\tilde{\rho}$ and describes the rapid overall relaxation of the density profile toward the target saddle-point density. In the second stage, a slow relaxation process follows which can be especially well recognized from $\tilde{\rho}$ at small intermolecular distances (close to and below $r_{\min}$) as shown in Fig. 4.6. In addition to these visualizations of $\tilde{\rho}$ during the relaxation process, the effect of the artificial density regularization can be detected in the RMSD curves shown in

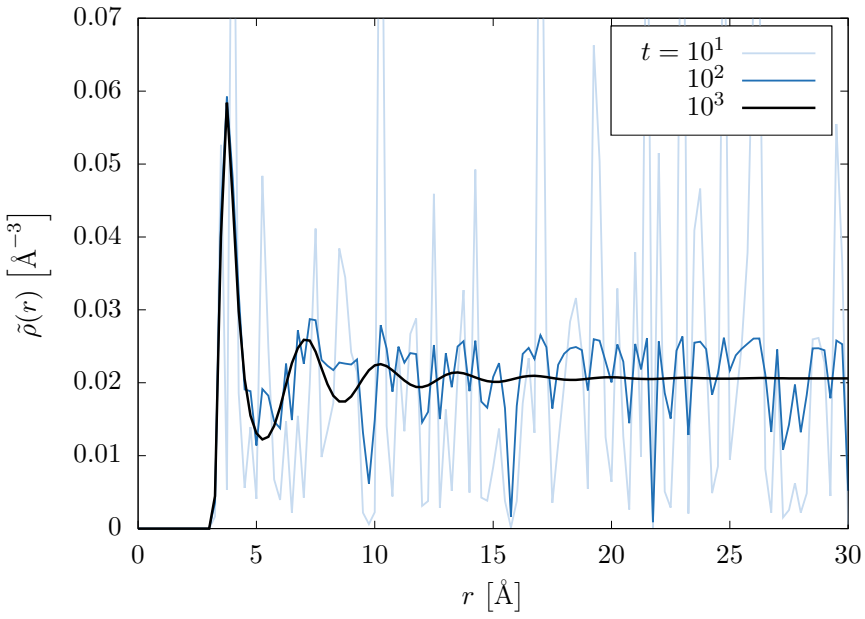

FIGURE 4.5: Fast overall relaxation of the density observable $\tilde{\rho}$ toward the saddle-point density ρ^* at $T = 80\,\mathrm{K}$ and given $\rho_{\min} = 10^{-10}$ Å^{-3}.

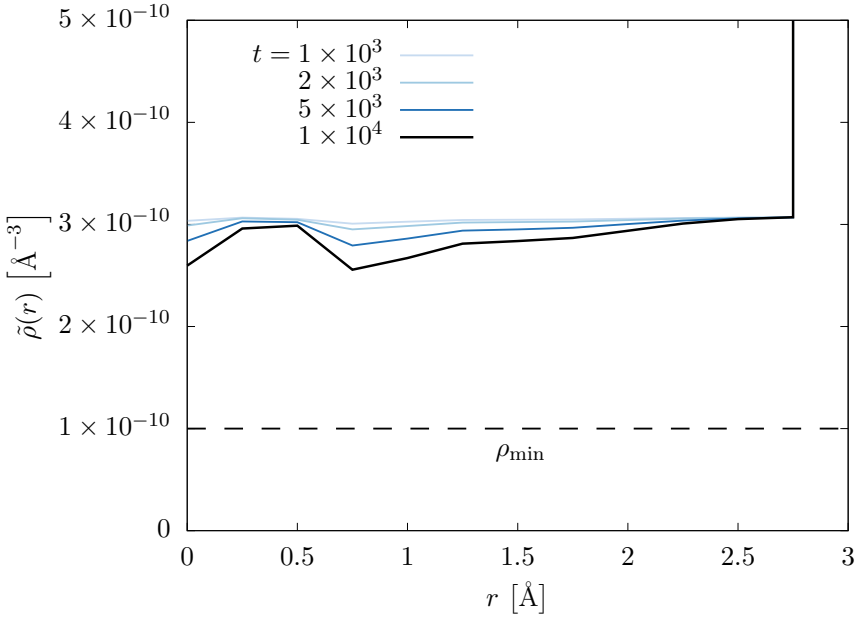

FIGURE 4.6: Slow relaxation of the density observable $\tilde{\rho}$ for distances close to and below $r_{\min}$ at $T = 80\,\mathrm{K}$ and given $\rho_{\min} = 10^{-10}$ Å^{-3}.

Fig. 4.4. In these curves, the minimum density constraint is hardly noticeable in the first stage (fast relaxation). In the second stage (slow relaxation), however, when $\tilde{\rho}$ is close to ρ^*, this constraint becomes more apparent. It is important to note that the density regularization is crucial for a fast and numerically stable relaxation. Nevertheless, the slow convergence to $\rho_{\min}$ (see Fig. 4.6) is of minor interest and the simulation could be stopped as soon as this regime is reached without losing any of the physics of the problem. To conclude this section, it is a remarkable finding that by externally providing an inverse poten-

tial u^{-1}, the method can immediately reproduce the correct structure of the fluid starting from a completely random initial state.

4.5 APPLICATIONS AND LIMITATIONS OF THE DERIVED u^{-1}

The numerical studies presented in the previous section demonstrate by the example of the Morse potential the possibility to infer an inverse potential from an externally (MD-)computed density distribution, which in turn empowers stand-alone field-based simulations to reproduce the correct density distribution even when starting from randomly chosen initial conditions. This approach is particularly powerful in itself, as it shows how other formalisms or computational tools can be embedded in the FTS framework by using the inverse potential as an interface between them. For example, it would allow one to determine $g(r)$ by alternative methods such as those from more sophisticated molecular mean-field theories, for instance, in the form of integral equation theories [106] (e.g., the Percus–Yevick equation [107] or the hypernetted-chain equation [108]) or from better molecular density functionals [109, 110], and in this way to link field-theoretic models directly to these methods.[11]

The inverse potential illustrated in Fig. 4.3 is used next in stand-alone field-based simulations to make predictions of saddle-point density profiles $\rho_p^*(r)$ at the other temperatures and bulk densities listed in Table 4.1. Along with the density profile at $T = 80\,\mathrm{K}$ from Section 4.4, the predicted profiles are shown in Fig. 4.7, obtained by starting from a random initial state and keep relaxing until $t = 2000$ where the slow relaxation regime is reached (cf. Fig. 4.4). Looking at the predicted curves, their dependence on temperature and bulk density becomes immediately visible. It can be seen that as the bulk density increases (the temperature decreases to keep the pressure constant), the entire $\rho_p^*(r)$ curve shifts upward. However, it is striking that no broadening or narrowing of the curves is seen as a consequence of the temperature change but instead the overall shape of the curves at various state points appears to be conserved. In particular, the comparison of the dotted red line ($T = 100\,\mathrm{K}$) with the solid black line ($T = 80\,\mathrm{K}$) in Fig. 4.7, both systems being at the same bulk density, indicates that the density profile is practically unaffected by a sole change in temperature over the range of temperatures considered. Admittedly, this should not be the expected behavior, since, with view to the comparative MD simulations illustrated in Fig. 4.2 by g_{MD}, the shape of the radial distribution function and that of the density distribution ρ_p^* should change as the temperature changes.

Technically, one can convince oneself of the correctness of the implementation leading to the results shown in Fig. 4.7 by inspecting

11 I would like to thank the anonymous reviewer of Ref. [84] for emphasizing the use of other methods in this context.

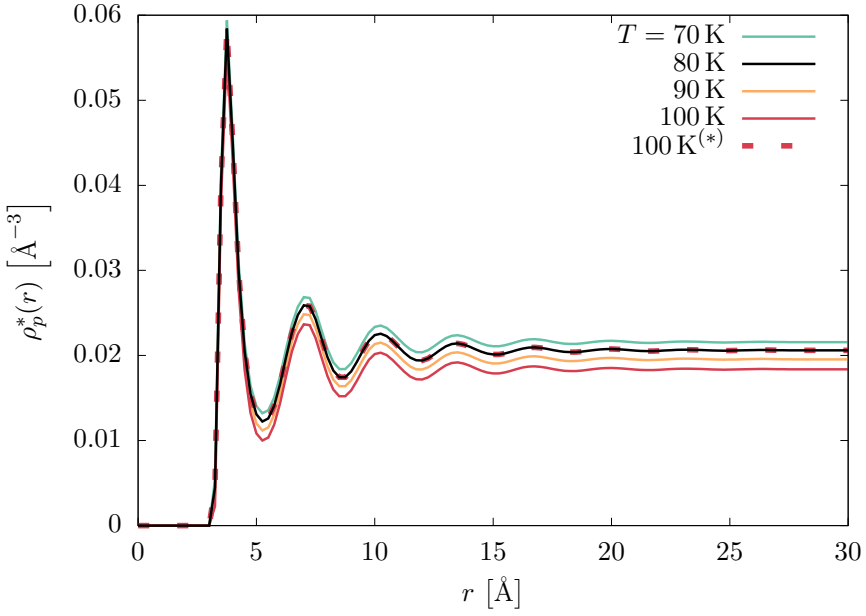

FIGURE 4.7: Predicted saddle-point density profiles $\rho_p^*(r)$ with the inverse potential calculated at $T = 80\,\mathrm{K}$ and $\rho_0 = 0.020\,597\,\text{Å}^{-3}$. The solid colored lines show the predictions at different T and ρ_0 pairs according to Table 4.1. The dotted line marked with (*) corresponds to the same bulk density ρ_0 as used in the calculation of u^{-1} but at temperature $T = 100\,\mathrm{K}$.

the relevant equations in more detail. Rearranging Eq. (4.24) for the saddle-point density leads, with $u^{-1} \equiv u_{Q^*}^{-1}$ and $w^* \equiv w_{Q^*}^*$, to

$$\rho^*(r) = i\left[u^{-1} * \left(\frac{w^*}{\beta}\right)\right](r). \tag{4.39}$$

For the given (MD-imposed) u^{-1}, the solution w^* is found by the relaxation scheme, so that this equation is consistent with

$$\frac{w^*(r)}{\beta} = iu(r) - i\zeta\rho_0 + \frac{i}{\beta}\ln\left(\rho^*(r)/\rho_0\right), \tag{4.40}$$

derived from the density observable (cf. Eqs. (4.22) and (4.27)). According to Eq. (4.39), the temperature dependence of ρ^* is implicit in the term $w^*(r)/\beta$. This term, given by Eq. (4.40), is in turn dominated by the first two terms on the right-hand side of this equation, which are temperature-independent in the present case. Apart from this technical point, the temperature dependence of the model can also be conceptually understood as an inherent limitation of the presented field-theoretic method. The simplifications made have evidently caused the field method to operate at a more coarse-grained level than the MD technique.

Finally, the nature of these simplifications is explored to provide a better understanding of this inherent limitation. Evidently, the saddle-point approximation is the ubiquitous simplification in the (MD-)assisted derivation of u^{-1}. Since the inverse potential in general needs to be determined only once, and a suitable condition for which the

saddle-point approximation holds can be freely chosen for this purpose, this should not be regarded as a severe restriction per se. In the following, and in order to understand the mechanisms of the saddle-point approximation for the present hybrid particle-field model, the saddle-point approximation for the density (Eq. (2.39)) shall not be assumed. Taking into account full fluctuations, the complex Langevin equation (cf. Eq. (2.43)) should serve as a basis. Here it is especially helpful to consider its time average form

$$\frac{\partial}{\partial t}\left\langle w(\boldsymbol{r},t)\right\rangle_t = -\left\langle \frac{\delta\mathcal{H}^{(\mathrm{HPF})}[w]}{\delta w(\boldsymbol{r},t)}\right\rangle_t + \left\langle \eta(t)\right\rangle_t . \tag{4.41}$$

Recalling the discussion of complex Langevin sampling from Section 2.3, (steady-state) time averages recover the corresponding ensemble averages. Noting that the part containing the time derivative trivially vanishes and that the η-containing part also vanishes conditioned by the noise statistics, it can be found that

$$0 = \left\langle \frac{\delta\mathcal{H}^{(\mathrm{HPF})}[w]}{\delta w(\boldsymbol{r})}\right\rangle \tag{4.42}$$

$$= \frac{1}{\beta}\left[u^{-1} * \left\langle w\right\rangle\right](\boldsymbol{r}) + i\left\langle \tilde{\rho}(\boldsymbol{r})\right\rangle . \tag{4.43}$$

The latter equation is similar to the saddle-point equation (Eq. (4.24)), although Eq. (4.43) incorporates fluctuation-corrected averages and refers to an approximation-free model.[12] Nevertheless, the approximate nature of the approach presented above for inferring the inverse potential becomes clear in the next step, which is to find a fluctuation-containing counterpart to Eq. (4.22). The counterpart equation has the underlying idea of using the given density distribution (Eq. (4.22) assumes the saddle-point approximation to this) to obtain information about the descriptive auxiliary field. In this context, Eq. (4.43) suggests that, in parallel with the saddle-point equation, there is a single average field configuration $\langle w(\boldsymbol{r})\rangle$ which, unlike the saddle-point solution $w^*(\boldsymbol{r})$, accounts for fluctuations and accurately describes $\langle\tilde{\rho}(\boldsymbol{r})\rangle$ (instead of $\rho^*(\boldsymbol{r})$ as in the case of $w^*(\boldsymbol{r})$), so that an approximation-free $u^{-1}(\boldsymbol{r})$ can be computed from Eq. (4.43). However, this hypothetical approximation-free line of argument breaks down once the average of the density observable

$$\left\langle\tilde{\rho}(\boldsymbol{r})\right\rangle = \rho_0 \exp\left(-\beta u(\boldsymbol{r})\right)\left\langle \exp\left(-iw(\boldsymbol{r}) - \ln Q[iw]\right)\right\rangle \tag{4.44}$$

is considered. To be able to rewrite now Eq. (4.22) in an analogous version containing the average density distribution $\langle w(\boldsymbol{r})\rangle$, the approximation

$$\left\langle \frac{\exp\left(-iw(\boldsymbol{r})\right)}{Q[iw]}\right\rangle \overset{!}{\approx} \frac{\exp\left(-i\left\langle w(\boldsymbol{r})\right\rangle\right)}{\left\langle Q[iw]\right\rangle} \tag{4.45}$$

12 It is very interesting to note that in Ref. [64] Fredrickson derived an "alternative" expression for $\tilde{\rho}$ through functional integration by parts (see Eq. (4.53) in the reference) which is identical to Eq. (4.43) rearranged in terms of $\tilde{\rho}$.

is required. Only under this approximation can a simple analog to Eq. (4.22) be found as

$$\langle w(\boldsymbol{r})\rangle \approx i\beta u(\boldsymbol{r}) + i\ln\left(\langle\rho(\boldsymbol{r})\rangle/\rho_0\right) + i\ln\left\langle Q^{(\mathrm{HPF})}\right\rangle. \tag{4.46}$$

This complementary perspective to Ref. [84] allows to understand even better the successfully applied principle of the MD-derived inverse potential. The argument here seems to be more profound than simply a saddle-point approximation. Equations (4.43) and (4.46) illustrate that although a density profile which may also contain particle-particle correlations can be dictated (and later be reproduced) for the determination of u^{-1}, the approximation used in Eq. (4.45) is reminiscent of that of a saddle-point consideration and seems to explain the problem in the predictability of density profiles at other state points (i.e., the apparent lack of temperature sensitivity). The implied necessary adjustment of the inverse potential reminds one of the corresponding inability of effective potentials in particle-based coarse-grained models to reproduce the correct structure and thermodynamics at different state points than those for which they were initially parameterized [12].

To give an understanding of the effects of the methodological approximations on the inferred inverse potential, calibrated u^{-1}'s are recomputed using the $g_{\mathrm{MD}}(r)$ curves from Fig. 4.2. The u^{-1} curves

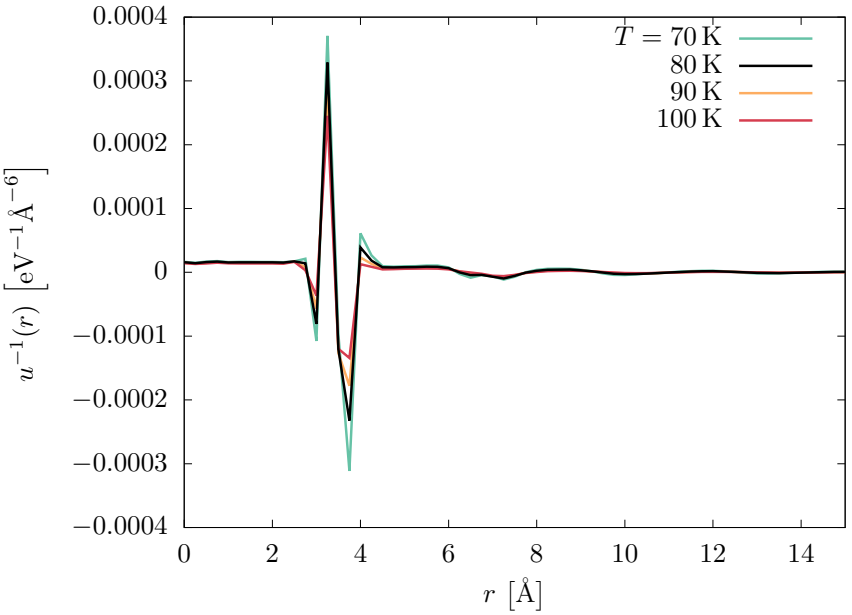

FIGURE 4.8: Calibrated inverse potentials computed at different temperatures from the $g_{\mathrm{MD}}(r)$ curves shown in Fig. 4.2.

shown in Fig. 4.8 keep their characteristic structure at all temperatures, but quantitative differences become apparent as the temperature changes. These differences illustrate, on the one hand, the qualitative accuracy of the model approximations for inferring an imposed inverse potential. On the other hand, they indicate how the original u^{-1} (the one computed at $T = 80\,\mathrm{K}$) should be modified for the predicted $\rho_p^*(r)$ curves to match those from the MD simulations.

Finally, it is important to emphasize that the proposed field-theoretic model is constructed as a prototype of more general models that contain the inverse potential in a form equivalent to $\langle w|u^{-1}|w\rangle$ in their field-theoretic Hamiltonian.[13] Thus, assisted by a low-cost calculation using an external method (not limited to MD), the inverse potential can be calibrated and then incorporated into an extended class of field-theoretic models that make use of it in the form $\langle w|u^{-1}|w\rangle$. This option to circumvent the inverse potential problem opens the way to introducing new, more physically relevant potentials into the FTS framework and thus significantly expands its regime of applicability to soft matter systems. At the same time, the advantage of the simple model formulation presented here brings with it a transferability problem which necessitates a recalibration of u^{-1} for state points outside the regime it was originally calculated.

13 Following Section 2.2, their specific molecular architecture is incorporated in Q.

5

DIRECT CALCULATION OF u^{-1}: THE GOOD, THE BAD, AND THE NAIVE

That the powerful play goes on,
and you may contribute a verse.
— Walt Whitman

Overall, there appears to be only a very small variety of interatomic interaction potentials used in field-theoretic models in the literature. This small number of non-bonded interactions, systematically classified in Section 2.4, reflects both the extent and significance of the inverse potential problem in FTS. Up to this point in the dissertation, several fundamental concepts have been introduced to address this shortcoming: The use of masking functions in various ways as demonstrated in Chapter 3 allows, on one hand, novel effective potentials to be introduced into a field description. On the other hand, in Chapter 4 the (fundamentally different) concept was discussed of how an inverse potential can be imposed on FTS models by coupling with other methods. Besides the use of masking functions and the coupling to external methods, a remaining aspect of the inverse potential problem is the direct calculation of u^{-1} from u, which is the subject of this chapter and closely aligned with the work presented in Ref. [111]. The chapter starts with Section 5.1 which motivates the computation of u^{-1} as a stand-alone function in view of alternative approaches. Next, in Section 5.2, a naive approach of directly inverting u through spatial discretization and matrix inversion or deconvolution is presented to offer more insight into the core problems of such an obvious attempt. Section 5.3 then deals with the actual analytical derivation of inverse potentials and, after a general discussion, takes up again the example of the Morse potential. In Section 5.4, the hybrid particle-field model introduced in Chapter 4 is revisited to demonstrate in a straightforward way how the analytical solution of the inverted Morse potential can be incorporated into a field-theoretic model. Numerical studies employing this FTS model are presented in Section 5.5.

5.1 THE INVERSE POTENTIAL AS A STAND-ALONE FUNCTION

On closer inspection, it may seem surprising that the actual analytical computation of the functional form of u^{-1} (with the exception of a particular case, the Yukawa potential in Section 3.4) has not been addressed so far. In fact, and to best of the author's knowledge, this also appears not to have been a major focus in the FTS literature to date. The reasons are manifold: The restriction to simple toy molecular models involving δ-interactions seems to be sufficient in specific research domains and research orientations for gaining a basic under-

standing of the phenomena taking place as discussed in Chapter 2. Apart from the cost of missing the direct connection to the chemistry [24] as mentioned in Chapter 4 and the consequent need to calibrate the toy model parameters [89], there may also be a conceptual question as to whether the recent and ongoing extensions of these toy models to advanced *molecular architectures* [112] may not make the refinement of *molecular interactions* seem necessary in an intermediate to long term perspective (i.e., to continue the path and move beyond the phenomenological picture).

Another reason for the lack of focus in the literature on the inverse potential itself is less apparent. For example, there has been an exceedingly interesting approach by Baeurle and co-workers in the area of field-theoretic models as they are discussed here which, however, has received comparatively little attention from the FTS community so far.[1] What makes these works (see, e.g., Refs. [113–116]) so interesting is the fact that the functional form of u^{-1} needs not necessarily be known, while at the same time nonlocal (beyond δ) pair interactions can in principle be incorporated into the field theory as demonstrated in Ref. [113] using the example of a Gaussian interaction potential. In the latter reference, a field-theoretic description is first derived by the familiar procedure of transforming the partition function, as generally outlined in Chapter 2. The need to know u^{-1} is formally circumvented initially by writing the corresponding u^{-1}-containing term in Fourier space, in the notation used here, as

$$\langle w|u^{-1}|w\rangle = \frac{1}{(2\pi)^3}\left\langle \overline{\hat{w}}\middle|\frac{1}{\hat{u}}\,\hat{w}\right\rangle, \tag{5.1}$$

assuming a real auxiliary field w according to Eq. (A.2.14) derived in the appendix. Concerning Eq. (5.1), it is seen that the relation between u and u^{-1} in Fourier space given by Eq. (3.21) has been tacitly applied in the work of Baeurle and co-workers. The intention of that work [113] was not to proceed with this Fourier representation containing the inverse potential but instead to perform a sophisticated transformation of the functional integral which contains in the integrand the statistical weight of the field description. At the end of this transformation there is an alternative representation of the functional integral, the so-called Gaussian equivalent representation (GER), which promises more favorable properties compared to the original form with respect to its numerical evaluation and the arising sign problem. As Baeurle and co-workers express it in Ref. [113], the basic idea of the GER is, under the introduction of a modified potential ($D(\boldsymbol{r})$ in their notation), to concentrate the main contribution to the functional integral in a quadratic Gaussian measure (which captures $D^{-1}(\boldsymbol{r})$ in their notation). The functional integration path of the auxiliary field is thereby deformed by a constant contour shift. The modified potential (i.e., its finite number of discrete Fourier components) and the contour shift are then chosen such that linear and

1 I would like to thank the anonymous reviewer of Ref. [111] for bringing to my attention the connection of these early works to the inverse potential problem formulated here.

quadratic terms of the auxiliary field, and as a side effect the inverse potential itself, no longer appear in the integrand of the functional integral. In the same reference [113], the authors proceed to apply to the transformed contour-shifted field-theoretic description a common Metropolis MC method for sampling some thermodynamic observables. Eventually, the authors conclude that this approach indeed seems to be capable of alleviating the sign problem to some extent but fails to solve it and, in particular, severe drawbacks of the method become apparent in regions close to phase transitions. From today's point of view, it seems as if these sampling problems could not be solved satisfactorily during those years, which is the case until today. Instead, Ref. [114] demonstrates the use of a 0-th order approximation of the GER for the grand canonical ensemble. In Ref. [115], this approximation, termed GER0, is also applied to the canonical ensemble and modified to address approximation inaccuracies for high particle densities. In summary, it is important to recognize that the intrinsically approximation-free GER is potentially an advanced approach to address the sign problem, but numerical sampling of thermodynamic observables still seems to present great difficulties in practice. The proposed solution of a 0-th order approximation brings the GER0 into the realm of self-consistent field theories, despite the fact that this approximation appears to offer several (some of them partly remarkable) advantages over conventional saddle-point approximations.

The last reason why the inverse potential appears not to have been a major focus in the FTS literature so far may seem more obvious in the context of the discussion of the inverse potential problem given in this dissertation. In light of the technical discussion in Section 3.2, it simply may not seem a straightforward task to directly derive analytical solutions for the inverse of physically relevant interaction potentials. In spite of this being another reason for the less prominent role of u^{-1} in FTS studies, it may seem clearly beneficial if more advanced inverse potentials are known and analytically available to any researcher interested in applying this powerful framework. Likewise, other models, such as the class that relies on hybrid particle-field simulations [57, 117–119] would potentially benefit substantially.[2] The analytical availability of advanced inverse potentials not only enables a deeper understanding of the accompanied complete theoretical model which, in itself, provides a starting point for the development of derivative models (analogous to the GREM from the Edwards model). But also having an advanced u^{-1} available as a stand-alone function provides an important component, for instance, as part of the complex Langevin method, and therefore paves the way for the development of approximation-free fully fluctuating models with advanced interactions.

2 I would like to thank the anonymous reviewer of Ref. [111] for highlighting this potential benefit.

5.2 BRUTE-FORCE CALCULATION OF u^{-1}

Considering the derivation of the Gaussian integral identity in Appendix A.1 forming the heart of the particle-to-field transformation, it seems natural to compute the inverse potential u^{-1}, based on the discrete representation of the functional integral (Eq. (A.1.2)), by direct numerical (brute-force) inversion of a discrete representation of u. Applying this "naive" approach, $\langle\rho|u|\rho\rangle \approx \boldsymbol{\rho}^T \cdot \boldsymbol{u} \cdot \boldsymbol{\rho}$ is expressed in the discrete case as in Eq. (A.1.7), and the $\boldsymbol{u}$ matrix (required to be positive definite) with entries $u_{ij} = \Delta V^2 u(\boldsymbol{r}_i - \boldsymbol{r}_j)$ is inverted to obtain a matrix representation of the inverse potential. The approximate relationship between the inverse matrix $\boldsymbol{u}^{-1}$ (with entries u_{ij}^{-1}) and the discretized form $u^{-1}(\boldsymbol{r}_i - \boldsymbol{r}_j)$ of the continuous u^{-1} function can then be found by comparing with the defining equation for u^{-1} (Eq. (3.15)) as

$$u^{-1}(\boldsymbol{r}_i - \boldsymbol{r}_j) \approx u_{ij}^{-1}. \tag{5.2}$$

For practical calculations, the volume is discretized on a cubic regular grid with edge length L and M grid points along each direction, resulting in a grid spacing $\Delta x = \frac{L}{M-1}$ with volume element $\Delta V = \Delta x^3$. The indices i and j run from 1 to M^3 thus generating a $\boldsymbol{u}$ matrix with $M^3 \times M^3$ entries. From a computational perspective, this naive way of determining u^{-1} by matrix inversion is challenging, since the size of the $\boldsymbol{u}$ matrix increases rapidly with M rendering its inversion computationally quite expensive. A computationally more favorable alternative to matrix inversion is to solve the derived defining convolution equation for u^{-1} (Eq. (3.20)) by discretization and deconvolution. In this case, it is convenient to apply the efficient 3D FFT algorithm already employed in the numerical computations of Chapter 4. According to the convention for the Fourier transform used in this dissertation, the continuous Fourier transform of u given a discrete $\boldsymbol{k}_i$ is approximated through the Fourier coefficient of the FFT corresponding to this $\boldsymbol{k}_i$ as

$$\mathcal{F}[u](\boldsymbol{k}_i) \approx \Delta V \ \mathrm{FFT}[u](\boldsymbol{k}_i). \tag{5.3}$$

The convolution theorem can then be applied to Eq. (3.20) (leading to Eq. (3.21)) under the approximation of Eq. (5.3) to compute values of u^{-1} at discrete grid points. The associated cubic regular grid in the spatial domain has edge length $L' = 2L$ and contains $M' = 2(M-1)$ grid points along each direction implying the same grid spacing $\Delta x = \frac{L'}{M'}$ as in the matrix inversion approach.

From Eq. (5.3) it becomes clear why the brute-force calculation of u^{-1} as presented here is considered as a "naive" approach. As explained in the discussion of the defining equation for u^{-1} (Eq. (3.15) and Eq. (3.20) respectively) in Section 3.2, the non-decaying behavior of the inverse potential in Fourier space renders the determination of u^{-1} as a stand-alone function a formidable task. At the same time, the discretization of continuous functions onto a regular grid implies at the same time the need to consider only finitely many contributions in Fourier space, and thus to introduce a numerical cutoff to the

wavenumber k. To demonstrate how this wavenumber cutoff affects the uniqueness of the inverse potential computed using this brute-force approach, the behavior of u^{-1} at a single point is considered for different discretization settings. As a possible point for the evaluation of u^{-1}, $r = 0$ lends itself particularly attractive for technical reasons as interpolations are avoided. As a complement to the brute-force approaches, the effect of the numerical wavenumber cutoff on the inverse potential is modeled analytically at $r = 0$ by the radial Fourier transform (RFT)

$$u^{-1}_{\mathrm{RFT}}(0) = \frac{1}{2\pi^2} \int_0^{k_{\mathrm{cut}}} \mathrm{d}k \, \frac{k^2}{\hat{u}(k)}, \tag{5.4}$$

which contains $k_{\mathrm{cut}} = \frac{\pi}{\Delta x}$ as an upper integration limit consistent with the FFT.

Based on this theoretical foundation of the brute-force calculation of u^{-1}, these concepts are next applied to the example of the Morse potential, already familiar from Chapter 4. The pair potential $u = u_{\mathrm{Morse}}$ is described by Eq. (4.5) and its radial Fourier transform $\hat{u} = \hat{u}_{\mathrm{Morse}}$ by Eq. (4.36). As in Chapter 4, the parameter values specified in Eqs. (4.9)-(4.11) are adopted. As a result of numerical inversion, it was shown that u^{-1} is found to be very sensitive to the grid spacing parameter Δx but rather insensitive to L at constant Δx even for very small box sizes. Therefore, $L = 10\,\text{Å}$ is chosen for investigating the sensitivity of $u^{-1}(0)$ to the grid spacing parameter Δx. The numerical results for the brute-force inversion of the Morse potential demonstrating this sensitivity are depicted in Fig. 5.1. The rapid increase of

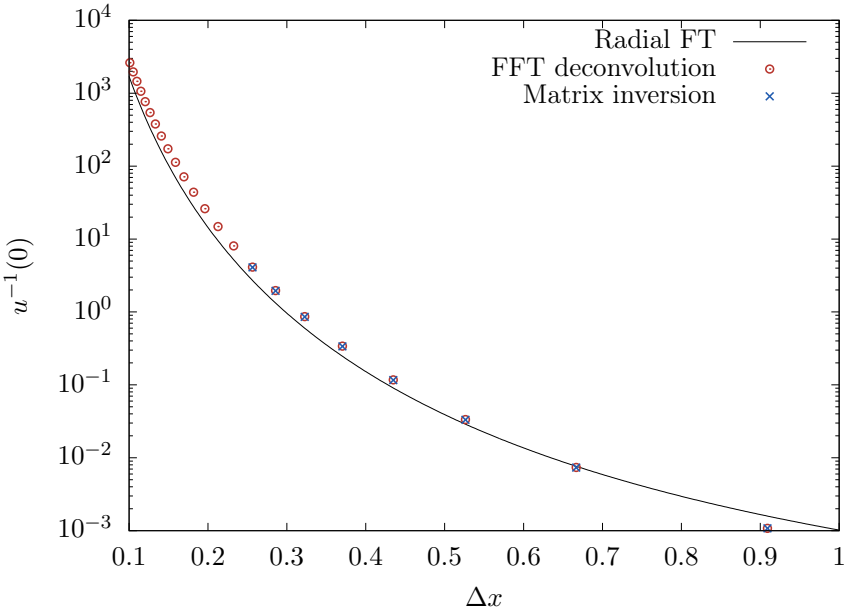

FIGURE 5.1: Sensitivity of u^{-1} to the grid spacing parameter Δx demonstrated at $r = 0$ when naively inverting u by the methods described in the text.

$u^{-1}(0)$ with finer and finer grid spacing Δx is quite evident in the figure providing a direct manifestation of the k-cutoff problem. On the

other hand, it becomes clear that both matrix inversion and deconvolution lead to practically identical results, which suggests that the k-cutoff problem, based on the discussion of the convolution equation, Eq. (3.20), is also an inherent (although less obvious) problem of other discrete methods operating exclusively in the spatial domain. Concerning the satisfactory qualitative description of $u^{-1}(0)$ by $u_{\mathrm{RFT}}^{-1}(0)$, it is encouraging to note that this k-cutoff problem can be modeled analytically and understood intuitively already by the comparatively simple approach connected with Eq. (5.4). This provides another indication for the problem of the numerically imposed cutoff (modeled as k_{cut}) and shows the conflict with the non-decaying Fourier transform $\hat{u}^{-1}(k)$ of the inverse potential.

5.3 ANALYTIC CALCULATION OF u^{-1}

After having highlighted in Section 5.2 the theoretical and numerical issues that come along with naive brute-force inversion of the interaction potential, this section details a procedure for analytically inverting advanced interaction potentials. In view of the systematic classification from Section 2.4 of interaction potentials commonly used in FTS, it is helpful to understand at this point that the presented analytical derivation can be seen as an extension of the second class, namely the implicit δ-interactions (see, for example, Table 2.1). This class is particularly suitable, since the characteristic of the Fourier transform $\hat{u}^{-1}$ to increase with k can be handled analytically for certain pair potentials u by means of the symbolic relation between powers of $\boldsymbol{k}$ in Fourier space and derivatives of the Dirac delta function in real space given by

$$(i\boldsymbol{k})^n \leftrightarrow \mathcal{F}\left[\nabla^n \delta\right](\boldsymbol{k}). \tag{5.5}$$

Based on this correspondence, one can propose pair potentials that are potentially suitable candidates to be utilized as implicit δ-interactions in FTS. Unfortunately, Eq. (5.5) is accompanied by the implicit requirement for the Fourier transform of the inverse potential, which according to Eq. (3.21) is the reciprocal of the Fourier transformed interaction potential, to be a (preferably low-degree) polynomial in $\boldsymbol{k}$. This additional requirement considerably limits the number of u candidates which can be chosen without the need for further approximations. As an illustration, for Gaussian interactions in 3D space

$$u_G(\boldsymbol{r}) = \frac{u_0}{\left(2\pi a^2\right)^{3/2}} \exp\left(-\frac{|\boldsymbol{r}|^2}{2a^2}\right), \tag{5.6}$$

similar to those described in Chapter 3 as effective interactions (cf. Eq. (3.6)), the reciprocal Fourier transform reads

$$\left(\mathcal{F}\left[u_G\right](\boldsymbol{k})\right)^{-1} = \frac{1}{u_0} \exp\left(\frac{1}{2} a^2 |\boldsymbol{k}|^2\right) \tag{5.7}$$

$$= \frac{1}{u_0} \sum_{n=0}^{\infty} \frac{a^{2n}}{2^n n!} |\boldsymbol{k}|^{2n}. \tag{5.8}$$

The inverse potential of these Gaussian interactions is consequently analytically given by the inverse Fourier transform of Eq. (5.8) as

$$u_G^{-1}(\boldsymbol{r}) = \frac{1}{u_0} \sum_{n=0}^{\infty} \frac{(-1)^n a^{2n}}{2^n n!} \nabla^{2n} \delta(\boldsymbol{r}), \tag{5.9}$$

implying the need to work with an infinite series of terms.[3] As expected, in the limiting case of explicit δ-interactions, $\lim_{a\to 0} u_G(\boldsymbol{r}) = u_0\,\delta(\boldsymbol{r})$, the correct inverse is recovered since $\lim_{a\to 0} u_G^{-1}(\boldsymbol{r}) = u_0^{-1}\,\delta(\boldsymbol{r})$. Taking into account the infinite series of terms, however, the approximation-free treatment of Gaussian interactions as implicit δ-interactions seems problematic (and therefore a "bad" choice of modeling), which gives reason to understand that these are commonly implemented as masked δ-interactions, as described in Section 3.1. An important observation that can be made is that, in the spirit of the above analysis, most of these problems are resolved if one uses exponential interactions in the microscopic model.

Indeed, as is apparent in the context of modeling exponentially decaying interactions, here noted as $u_e(\boldsymbol{r}) = A\exp(-B\,|\boldsymbol{r}|)$ with positive B as given earlier by Eq. (3.8), through an effective potential as masked δ-interactions in Section 3.1, the 3D Fourier transform of these interactions,[4] Eq. (3.9), well satisfies the implicit requirement for

$$\left(\mathcal{F}\left[u_e\right](\boldsymbol{k})\right)^{-1} = \frac{1}{8\pi AB}\left(|\boldsymbol{k}|^4 + 2B^2\,|\boldsymbol{k}|^2 + B^4\right) \tag{5.10}$$

to involve a low-degree polynomial in $\boldsymbol{k}$. Accordingly, the inverse potential of exponential interactions is given analytically by

$$u_e^{-1}(\boldsymbol{r}) = \frac{1}{8\pi AB}\left(\nabla^4\delta(\boldsymbol{r}) - 2B^2\nabla^2\delta(\boldsymbol{r}) + B^4\delta(\boldsymbol{r})\right), \tag{5.11}$$

which, unlike the inverse of Gaussian interactions from Eq. (5.9), contains only a finite number of terms.

A "good" example of a physically motivated interaction potential which can be described by exponentially decaying terms is the Morse one as it was also used in the HPF model in Chapter 4. It seems helpful in this perspective to write the Morse potential as a difference of two *positive* functions (a repulsive and an attractive part):

$$u_{\text{Morse}}(\boldsymbol{r}) \equiv u_R(\boldsymbol{r}) - u_A(\boldsymbol{r}). \tag{5.12}$$

with

$$u_R(\boldsymbol{r}) = \epsilon\exp\left(-2\xi\left(r - r_{\min}\right)\right), \tag{5.13}$$
$$u_A(\boldsymbol{r}) = 2\epsilon\exp\left(-\xi\left(r - r_{\min}\right)\right). \tag{5.14}$$

3 To the best of the author's knowledge, it was in Ref. [111] associated with the material of this chapter that the inverse potential of Gaussian interactions u_G^{-1} was presented for the first time as an analytic stand-alone expression in the context of field-theoretic models.

4 I would like to thank Hans Christian for drawing the analogy between the Fourier transform of the exponential interactions, Eq. (3.9), and the one-loop structure of a massive scalar field with quartic interactions, where B has the meaning of the mass of the quantum particle [120].

Being positive-definite functions, both u_R and u_A possess well-defined functional inverses. Using Eq. (5.11) as a basis, the respective identification of A and B for Eqs. (5.13) and (5.14) allows then to find the two inverses as

$$u_R^{-1}(\boldsymbol{r}) = c_R \left[\nabla^4\delta(\boldsymbol{r}) - 8\xi^2\nabla^2\delta(\boldsymbol{r}) + 16\xi^4\delta(\boldsymbol{r})\right], \tag{5.15}$$

$$u_A^{-1}(\boldsymbol{r}) = c_A \left[\nabla^4\delta(\boldsymbol{r}) - 2\xi^2\nabla^2\delta(\boldsymbol{r}) + \xi^4\delta(\boldsymbol{r})\right], \tag{5.16}$$

with

$$c_R = \left(16\pi\epsilon\xi \exp\left(2r_{\min}\xi\right)\right)^{-1}, \tag{5.17}$$

$$c_A = \left(16\pi\epsilon\xi \exp\left(r_{\min}\xi\right)\right)^{-1}. \tag{5.18}$$

5.4 REVISITING THE SELF-CONSISTENT HPF MODEL

How, based on the properties of Fourier transforms, inverse potentials can be analytically derived for possible candidates of physically useful interaction potentials and having demonstrated this approach for the Morse potential in Section 5.3 can certainly be seen as one of the most important contributions of this chapter to the design of novel and seminal FTS studies in the future. The advanced inverse potentials thus derived can be used as a core component in truly sophisticated physically detailed models in soft matter and complex fluids, which have not appeared as approximation-free field descriptions before (with all their advantages and disadvantages compared to particle-based ones). The implementation of such models, nevertheless, is relatively time-consuming and also challenging from a purely technical (algorithmic and/or computational) point of view. However, it would seem inappropriate to stop at this point without at least demonstrating a simple application. The simple application that seems most obvious for this purpose is the hybrid particle-field (HPF) model discussed in detail in Chapter 4.

The mathematical formulation of the HPF model is intended to be close to that of Section 4.2 with the difference being the two-part splitting of the interaction potential according to Eq. (5.12), consequently leading to a two-field model in the derived field-theoretic description. To account for splitting the potential as the *difference* of two positive functions, the density field $i\check{\rho}(\boldsymbol{r}) \equiv \hat{\rho}(\boldsymbol{r})$ is introduced, which allows to separate repulsive and attractive contributions to the energy:

$$U = \frac{1}{2}\langle\hat{\rho}|u_{\text{Morse}}|\hat{\rho}\rangle = \frac{1}{2}\langle\hat{\rho}|u_R|\hat{\rho}\rangle + \frac{1}{2}\langle\check{\rho}|u_A|\check{\rho}\rangle. \tag{5.19}$$

Next, the Gaussian integral identity, Eq. (2.8), is applied to each one of these contributions to transform the canonical partition function into a two-field model of $w_R(\boldsymbol{r})$ and $w_A(\boldsymbol{r})$. Similarly to the procedure described in Chapter 4, fixing the n-th particle at the origin, $\boldsymbol{r}_n = \boldsymbol{0}$, and excluding it from the particle-to-field transformation leads to a field representation of the canonical partition function,

$$\mathcal{Z}_c\big|_{\boldsymbol{r}_n=\boldsymbol{0}} \propto \int \mathcal{D}w_R \int \mathcal{D}w_A \; \exp\left(-\mathcal{H}^{(\text{HPF2})}[w_R, w_A]\right), \tag{5.20}$$

containing the two-field field-theoretic Hamiltonian given (for $n \gg 1$)[5] by

$$\mathcal{H}^{(\mathrm{HPF2})}[w_R, w_A] \approx \frac{1}{2\beta}\langle w_R|u_R^{-1}|w_R\rangle + \frac{1}{2\beta}\langle w_A|u_A^{-1}|w_A\rangle - n\ln Q^{(\mathrm{HPF2})}\left[iw_R + w_A\right], \tag{5.21}$$

where w_A as an argument in the reduced partition function Q does not carry a factor of i as this has been absorbed in the definition of $\check{\rho}$. The reduced partition function

$$Q^{(\mathrm{HPF2})}[iw_R + w_A] = \frac{1}{V}\int \mathrm{d}^3r\, \exp\left(-\beta u_{\mathrm{Morse}}(\boldsymbol{r}) - (iw_R(\boldsymbol{r}) + w_A(\boldsymbol{r}))\right) \tag{5.22}$$

is incorporated into the density field observable of the surrounding $n-1$ particles through

$$\tilde{\rho}(\boldsymbol{r}) = \rho_0 \exp\left(-\beta u_{\mathrm{Morse}}(\boldsymbol{r}) - (iw_R(\boldsymbol{r}) + w_A(\boldsymbol{r})) - \ln Q^{(\mathrm{HPF2})}\right). \tag{5.23}$$

On the basis of this field-theoretic model of the Morse fluid, it is then straightforward to derive the saddle-point equations for a self-consistent model description like it was done in Chapter 4 but now for two fields:

$$\left.\frac{\delta\mathcal{H}^{(\mathrm{HPF2})}[w_R, w_A]}{\delta w_{R,A}(\boldsymbol{r})}\right|_{w_{R,A}=w^*_{R,A}} = 0. \tag{5.24}$$

Exploiting the interchangeability of derivatives for convolutions, the functional derivatives of $\mathcal{H}^{(\mathrm{HPF2})}[w_R, w_A]$ can be calculated directly from Eq. (5.21) as

$$\frac{\delta\mathcal{H}^{(\mathrm{HPF2})}}{\delta w_R(\boldsymbol{r})} = \frac{1}{\beta}\left[u_R^{-1} * w_R\right](\boldsymbol{r}) + i\tilde{\rho}(\boldsymbol{r}) \tag{5.25}$$

$$= \frac{c_R}{\beta}\left(\nabla^4 w_R(\boldsymbol{r}) - 8\xi^2\nabla^2 w_R(\boldsymbol{r}) + 16\xi^4 w_R(\boldsymbol{r})\right) + i\tilde{\rho}(\boldsymbol{r}), \tag{5.26}$$

and

$$\frac{\delta\mathcal{H}^{(\mathrm{HPF2})}}{\delta w_A(\boldsymbol{r})} = \frac{1}{\beta}\left[u_A^{-1} * w_A\right](\boldsymbol{r}) + \tilde{\rho}(\boldsymbol{r}) \tag{5.27}$$

$$= \frac{c_A}{\beta}\left(\nabla^4 w_A(\boldsymbol{r}) - 2\xi^2\nabla^2 w_A(\boldsymbol{r}) + \xi^4 w_A(\boldsymbol{r})\right) + \tilde{\rho}(\boldsymbol{r}), \tag{5.28}$$

thus turning the saddle-point equations into differential equations. Since the interaction potential $u_{\mathrm{Morse}}(\boldsymbol{r})$ is radially symmetric, the two inverses $u_R^{-1}(\boldsymbol{r})$ and $u_A^{-1}(\boldsymbol{r})$ are also radially symmetric and therefore the entire field-theoretic model exhibits radial symmetry as well. This

5 The simplification resulting from this assumption is motivated and discussed in the context of the density field observable $\tilde{\rho}$ of the HPF model in Chapter 4 below Eq. (4.18).

allows to transform the 3D field model into a 1D radial field model which depends only on the spatial coordinate $r = |\boldsymbol{r}|$. For radial symmetry, ∇^2 is described by the radial Laplacian,

$$\nabla_r^2 = \frac{\partial^2}{\partial r^2} + \frac{2}{r}\frac{\partial}{\partial r}, \tag{5.29}$$

and ∇^4 is described by the radial part of the squared Laplacian,

$$\nabla_r^4 = \frac{\partial^4}{\partial r^4} + \frac{4}{r}\frac{\partial^3}{\partial r^3}. \tag{5.30}$$

Using these expressions for the differential operators, the two saddle-point equations are transformed to two fourth-order 1D differential equations,

$$\begin{aligned}\frac{c_R}{\beta}\Bigg(&\frac{\partial^4 w_R^*(r)}{\partial r^4} + \frac{4}{r}\frac{\partial^3 w_R^*(r)}{\partial r^3} - 8\xi^2\frac{\partial^2 w_R^*(r)}{\partial r^2} \\ &- \frac{16\xi^2}{r}\frac{\partial w_R^*(r)}{\partial r} + 16\xi^4 w_R^*(r)\Bigg) + i\tilde{\rho}(r) = 0\end{aligned} \tag{5.31}$$

and

$$\begin{aligned}\frac{c_A}{\beta}\Bigg(&\frac{\partial^4 w_A^*(r)}{\partial r^4} + \frac{4}{r}\frac{\partial^3 w_A^*(r)}{\partial r^3} - 2\xi^2\frac{\partial^2 w_A^*(r)}{\partial r^2} \\ &- \frac{4\xi^2}{r}\frac{\partial w_A^*(r)}{\partial r} + \xi^4 w_A^*(r)\Bigg) + \tilde{\rho}(r) = 0.\end{aligned} \tag{5.32}$$

To solve them, Eqs. (5.31) and (5.32), four boundary conditions are needed for each one. The specification of these boundary conditions does not seem to be an easy task,[6] since the fields $w_R(r)$ and $w_A(r)$ are not physical observables. From the overall eight boundary conditions needed, four are to be specified at $r = 0$ and the remaining four at $r = R$, with the understanding that R tends to infinity. The four boundary conditions on the right ($r = R$) are derived from the condition that the density observable $\tilde{\rho}(r)$ should approach its bulk value there, $\tilde{\rho}(R) = \rho_0$. Since approaching of $\tilde{\rho}(r)$ to a constant value implies also approaching of the auxiliary fields to a constant value, the first two boundary conditions at $r = R$ are

$$\frac{\partial w_R^*(R)}{\partial r} = 0, \tag{5.33}$$

$$\frac{\partial w_A^*(R)}{\partial r} = 0. \tag{5.34}$$

In addition and on the basis of the required bulk behavior at $r = R$, two further boundary conditions are derived from the saddle-point equations, Eqs. (5.31) and (5.32),

$$w_R^*(R) = -\frac{i\beta\rho_0}{16\xi^4 c_R}, \tag{5.35}$$

$$w_A^*(R) = -\frac{\beta\rho_0}{\xi^4 c_A}. \tag{5.36}$$

6 I apologize to the reader for what it is now probably a rather technical and less enjoyable paragraph of this dissertation. Regardless of this and recognizing that you have truly dived so deep into this work to find this little footnote, I would greatly appreciate those of you who arrived at this point to send a quick message to footnote@weyman.ch.

The four boundary conditions on the left ($r = 0$) are more difficult to specify because the behavior of the density observable is unknown there. However, the defining convolution equation of the inverse, Eq. (3.20), can be used to transform the saddle-point equations to the form

$$w_R^*(\boldsymbol{r}) = -i\beta \left[u_R * \tilde{\rho}\right](\boldsymbol{r}), \tag{5.37}$$
$$w_A^*(\boldsymbol{r}) = -\beta \left[u_A * \tilde{\rho}\right](\boldsymbol{r}), \tag{5.38}$$

while maintaining the self-consistency of the model. Two boundary conditions at $r = 0$ conforming to this self-consistency are then formulated as space integrals as follows:

$$w_R^*(0) = -i\beta \int_V \mathrm{d}^3 r \; u_R(\boldsymbol{r})\tilde{\rho}(\boldsymbol{r}), \tag{5.39}$$
$$w_A^*(0) = -\beta \int_V \mathrm{d}^3 r \; u_A(\boldsymbol{r})\tilde{\rho}(\boldsymbol{r}). \tag{5.40}$$

By further calculating the derivatives of Eqs. (5.37) and (5.38) with respect to $\alpha = x, y, z$, it is found that

$$\frac{\partial w_R^*(\boldsymbol{r})}{\partial \alpha} = -i\beta \int_V \mathrm{d}^3 r' \; \frac{\partial u_R(\boldsymbol{r}-\boldsymbol{r}')}{\partial \alpha}\tilde{\rho}(\boldsymbol{r}') \tag{5.41}$$
$$= i\beta \int_V \mathrm{d}^3 r' \; 2\xi \frac{\alpha - \alpha'}{|\boldsymbol{r}-\boldsymbol{r}'|} u_R(\boldsymbol{r}-\boldsymbol{r}')\tilde{\rho}(\boldsymbol{r}') \tag{5.42}$$

and

$$\frac{\partial w_A^*(\boldsymbol{r})}{\partial \alpha} = -\beta \int_V \mathrm{d}^3 r' \; \frac{\partial u_A(\boldsymbol{r}-\boldsymbol{r}')}{\partial \alpha}\tilde{\rho}(\boldsymbol{r}') \tag{5.43}$$
$$= \beta \int_V \mathrm{d}^3 r' \; \xi \frac{\alpha - \alpha'}{|\boldsymbol{r}-\boldsymbol{r}'|} u_A(\boldsymbol{r}-\boldsymbol{r}')\tilde{\rho}(\boldsymbol{r}'). \tag{5.44}$$

Since the integrands become odd functions at $\boldsymbol{r} = \boldsymbol{0}$, it is

$$\frac{\partial w_R^*(\boldsymbol{0})}{\partial \alpha} = 0, \tag{5.45}$$
$$\frac{\partial w_A^*(\boldsymbol{0})}{\partial \alpha} = 0, \tag{5.46}$$

from which the remaining two boundary conditions at $r = 0$ are derived as

$$\frac{\partial w_R^*(0)}{\partial r} = 0, \tag{5.47}$$
$$\frac{\partial w_A^*(0)}{\partial r} = 0. \tag{5.48}$$

5.5 NUMERICAL STUDIES OF THE ANALYTICAL HPF MODEL

Based on the previous Section 5.4, in which a hybrid particle-field model containing the analytical inverses of the Morse potential was derived and the application of the saddle-point approximation was demonstrated, numerical SCFT studies of this model are presented

now in this section. The parameters of the Morse potential are chosen as the standard ones in Eqs. (4.9)-(4.11); similarly, $T = 80\,\mathrm{K}$ and $\rho_0 = 0.020\,597\,\text{Å}^{-3}$ as in Table 4.1. However, a different choice of these parameters may be stated in some additional calculations, for example, when the sensitivity of the results with respect to these parameters is going to be investigated. To numerically solve for the saddle-point configurations w_R^* and w_A^*, the r domain is discretized by using a 1D regular (equidistant) grid with M grid points. After finite size effects have been checked, the domain size is set to $R = 50\,\text{Å}$ and a generously fine grid spacing of $\Delta r = 0.01\,\text{Å}$ is chosen. The first- and second-order derivatives are computed by the fourth-order central finite differences scheme, and the third- and fourth-order ones are computed by the second-order central finite differences scheme. The discretized versions of the continuous functional derivatives $\frac{\delta\mathcal{H}^{(\mathrm{HPF2})}}{\delta w_R(\boldsymbol{r})}$ and $\frac{\delta\mathcal{H}^{(\mathrm{HPF2})}}{\delta w_A(\boldsymbol{r})}$ on the left hand side of Eqs. (5.31) and (5.32) are interpreted as residuals of these equations whose solutions are found using the Newton–Raphson method. For this purpose, the two parts of $\frac{\delta\mathcal{H}^{(\mathrm{HPF2})}}{\delta w_R(r_j)}$ and $\frac{\delta\mathcal{H}^{(\mathrm{HPF2})}}{\delta w_A(r_j)}$ are concatenated to obtain an overall residue vector $\boldsymbol{F}$ which is real ($\boldsymbol{F} \in \mathbb{R}^{2M}$), as only the real part of $w_A(r_j)$ and the imaginary part of $w_R(r_j)$ are considered in the calculations. The boundary conditions are formulated as residuals as well, corresponding to the boundary points of the grid. The Jacobian $\boldsymbol{J} \in \mathbb{R}^{2M\times 2M}$ required in the Newton–Raphson method is computed numerically and the discrete versions of the fields $w_R(r_j)$ and $w_A(r_j)$ are concatenated to form the vector $\boldsymbol{w} \in \mathbb{R}^{2M}$ which is updated according to

$$\boldsymbol{w}^{(N+1)} = \boldsymbol{w}^{(N)} - \lambda \boldsymbol{J}^{-1} \cdot \boldsymbol{F}, \tag{5.49}$$

with $\lambda \in (0, 1]$ acting as an under-relaxation parameter. Having an eye on Eq. (5.49), it is interesting to note its mathematical similarity with common SCFT field update algorithms [77]. For instance, the simple Euler–Maruyama method is obtained for $\boldsymbol{J}_{\mathrm{EM}}^{-1} = \mathbf{1}$ and $\lambda_{\mathrm{EM}} = \Delta t$ (the fictitious time step).

As an introduction to the numerical studies of the analytical Morse fluid, a consistency check of the model's implementation is first presented. This is done by taking advantage of the fact that an analytical expression for the value of Q at the saddle point has already been derived in Chapter 4. Rewriting Eq. (4.27) and inserting the Morse potential from Eq. (4.5),

$$-k_B T \ln Q^* = \rho_0 \int_V \mathrm{d}^3 r \; u_{\mathrm{Morse}}(\boldsymbol{r}) \tag{5.50}$$

$$= \rho_0 \pi \epsilon \xi^{-3} \exp\left(r_{\min}\xi\right)\left(\exp\left(r_{\min}\xi\right) - 16\right), \tag{5.51}$$

showing the strong dependence of this field-theoretic observable on the specific choice of the Morse potential parameters which predestines this observable for a consistency check concerning the implementation of the analytical inverse potential. A comparison of the numerically calculated Q^* values with the analytical predictions given by Eq. (5.51) is shown in Fig. 5.2, indicating excellent agreement. At this point, it may seem helpful to recall the close connection between

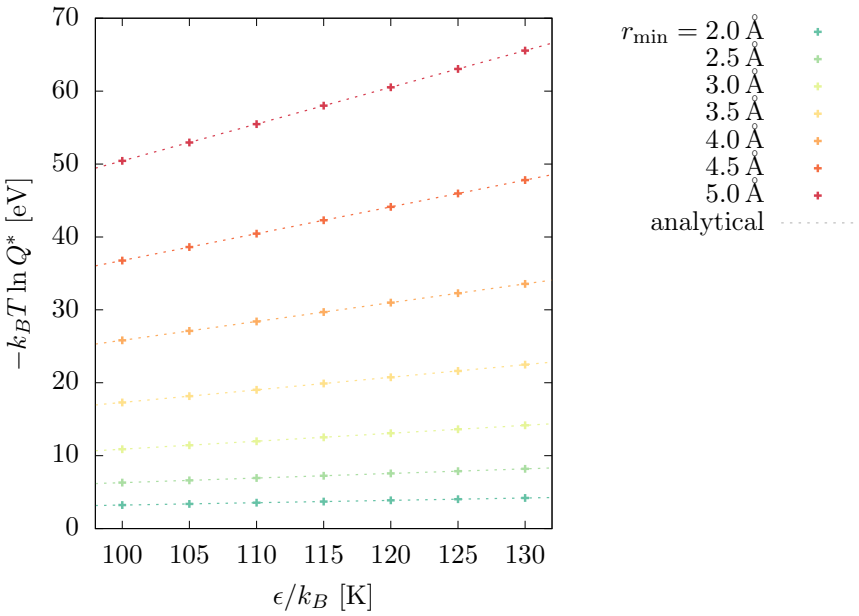

FIGURE 5.2: Numerically computed saddle-point values of Q for different choices of the $r_{\min}$ and ϵ parameters of the Morse potential ($\xi = 6/r_{\min}$) and comparison with the analytical solution given by Eq. (5.51).

$-k_BT \ln Q^*$ and the excess chemical potential for the saddle point as outlined in Section 3.4. The condition for the one-field HPF model from Chapter 4 that $\xi > \frac{4 \ln 2}{r_{\min}}$ (see Sec. 4.4) can be understood here in a more physical sense in terms of the excess chemical potential. Although a two-field model is present here, the same condition on ξ ensures a positive volume integral in Eq. (5.50) and hence a positive contribution to the excess chemical potential. As detailed further in this chapter, ξ can be understood as a parameter governing the softness of the particles. Consequently, a large enough ξ ensures the dominance of the repulsive interactions and counteracts system collapse.

After the successful consistency check has been demonstrated, the saddle-point configurations $w_R^*(r)$ and $w_A^*(r)$ as solutions of the differential equations, Eqs. (5.31) and (5.32), are presented using the standard set of parameters from above. Figure 5.3 shows the radial profiles of the field configurations $w_R^*(r)$ and $w_A^*(r)$, accordingly rescaled by the values of the boundary conditions. This form of rescaling is intended to indicate (also with regard to the slopes of the curves in the boundary regions) the consistency of the saddle-point solutions with the imposed boundary conditions. Further, it can be seen that both fields show a smooth behavior, both of them decaying with r and approaching their bulk value. Regarding the decay behavior, it is expected that the fields should decay on length scales that are characteristic of the respective part of the pair potential. The corresponding decay behavior shown in Fig. 5.3 is immediately understandable when considering that $u_R(r)$ decays faster than $u_A(r)$.

The presented solutions $w_R^*(r)$ and $w_A^*(r)$ of the saddle-point equations can then be used to calculate other field-theoretic observables as-

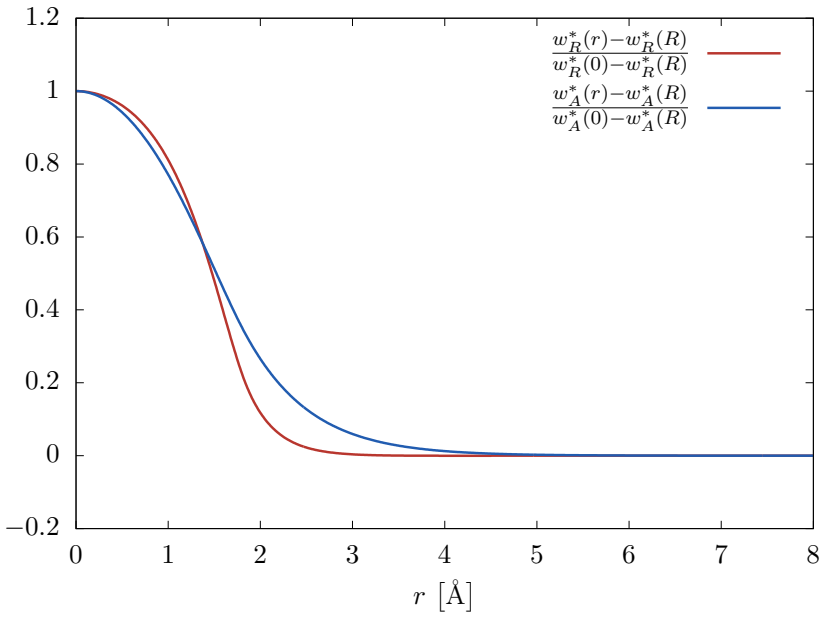

FIGURE 5.3: Saddle-point configurations $w_R^*(r)$ and $w_A^*(r)$ as solutions of Eqs. (5.31) and (5.32) normalized by the values of their boundary conditions (Eqs. (5.35), (5.36), (5.39), and (5.40)) given for the standard set of parameters at the beginning of Sec. 5.5.

suming the saddle-point approximation. For the HPF model at hand, it seems natural to study the density observable from Eq. (5.23) at the saddle point, or equivalently the saddle-point approximation of the radial distribution function $g^*(r)$. The latter is related to the density observable by

$$g^*(r) = \frac{\tilde{\rho}(r)}{\rho_0}\bigg|_{w_{R,A}=w_{R,A}^*} \tag{5.52}$$

in a similar way as discussed in Chapter 4 (cf. Eq. (4.37)). The numerical results of the so calculated $g^*(r)$ are shown by the black curve in Fig. 5.4. In comparison with the MD-calculated $g^*(r)$ from Chapter 4, shown again in the inset in Fig. 5.4, certain similarities but also drastic differences are quite apparent. A particularly striking feature is that the maximum is located at around 1.8 Å, which is substantially below the value of $r_{\min}$ set by the model. Moreover, the curve lacks any secondary peaks as observed for the MD-derived RDF. Concerning the position of the main peak, it may seem reasonable to assume the interactions between the central probe particle and the surrounding bulk particles not to be in balance, meaning that the pair interactions at the particle level (governed by u_{Morse}) are not balanced with the interactions at the field level (governed by the inverse potentials). This imbalance becomes immediately understandable bearing in mind that the field-described part of the HPF model is subject to the saddle-point approximation and therefore the central probe particle interacts with its environment in the sense of a mean-field description. To address the hypothesis that it is indeed an interplay of both interactions (the one inherent to the particle description and the other inherent to the

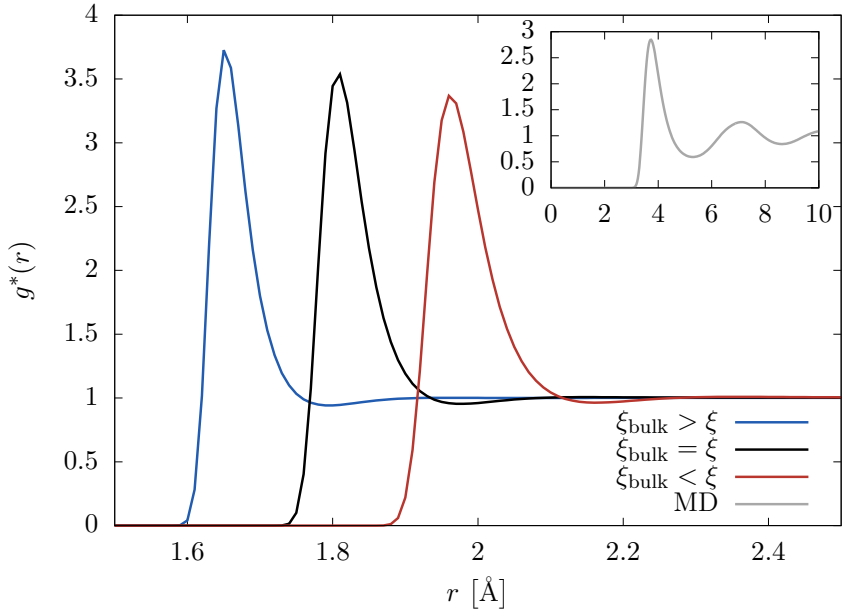

FIGURE 5.4: Saddle-point RDFs $g^*(r)$ for differently tuned bulk interactions characterized by the Morse parameter ξ_{bulk}. The respective deviations of ξ_{bulk} from ξ are within $\pm 5\,\%$. The inset shows the MD-calculated RDF obtained in Chapter 4, wherein thermal fluctuations are fully taken into account.

field description) and that the surrounding density field is not displaced unilaterally by the sole presence of the probe particle, two more curves representing calculations from modified sets of parameters wherein only the field-based bulk interactions have been changed are shown in Fig. 5.4. As noted above, the Morse ξ parameter can be interpreted as a control parameter of the softness of the particles. Reducing the value of this parameter for the surrounding bulk particles, denoted by ξ_{bulk} in the following, below that of $\xi = 6/r_{\text{min}}$, the bulk particles become softer in relation to the probe particle and the density field of these softer particles is thus pushed further away from the central particle as the red curve in Fig. 5.4 indicates. In the opposite case, $\xi_{\text{bulk}} > \xi$, the central particle is softer in relation to the surrounding particles and the density field correspondingly moves closer to the probe particle as it is evident from the blue curve in the same figure. This kind of mutual influence seems to suggest that, at least for this hybrid particle-field model, particle-particle correlations are present to some extent, as has also been reported in the past by Koski and co-workers [56] and as was enforced in Chapter 4 where a target density distribution was imposed. Nevertheless, the use of the saddle-point approximation[7] leads to different results of the radial distribution functions compared to those obtained from the MD

7 The saddle-point approximation is to be considered here as a strong simplification taken to avoid unnecessary complexity and to help focus on the conceptual incorporation of advanced inverse potentials of physically relevant interactions into field-theoretic models. This seems legitimate because the inverse potential is part of the field-theoretic model itself, and thus no conceptual difference is to be expected in this respect when realizing fully fluctuating field simulations.

simulations, indicating the coarse-grained nature of the mean-field approach. However, if the saddle-point approximation is taken for granted, all the results derived in this scope appear consistent. As such, the final presentation of the temperature dependence of $g^*(r)$ is no exception in this regard. Indeed, it can be seen in Fig. 5.5 that, compared to the previous case ($\xi_{\text{bulk}} = \xi$ at $T = 80\,\text{K}$ in Fig. 5.4), the main peak becomes broader at higher temperatures and narrower at lower temperatures, which seems consistent with intuitive expectations.

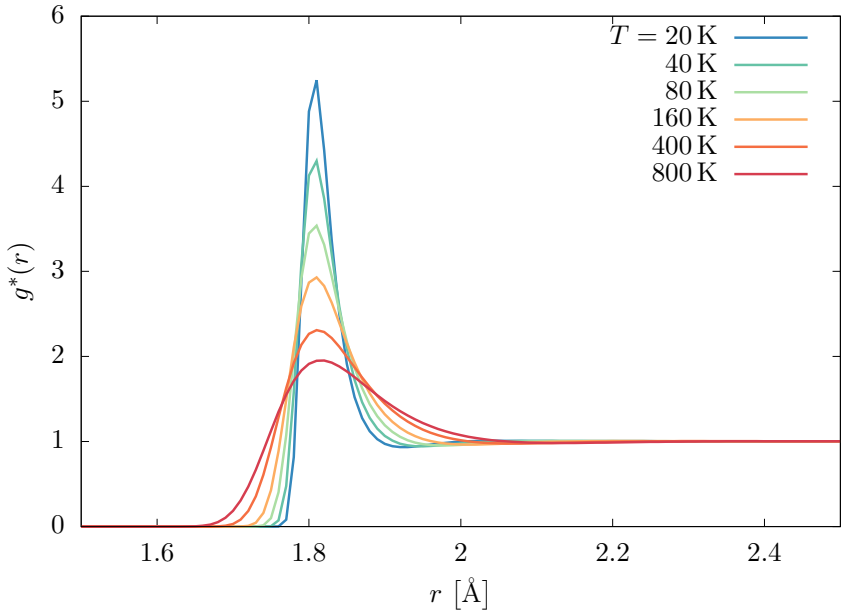

FIGURE 5.5: Saddle-point RDFs $g^*(r)$ at different temperatures.

Overall, the numerical studies put forward here reveal how remarkably straightforward it is to apply advanced analytically derived inverse potentials to field-theoretic simulations in practice. Not only because of the all-important new example of the inverted Morse potential but also with respect to the recipe for direct calculation of advanced inverse potentials presented in Section 5.3, this chapter marks a new starting point for the design of thoroughly novel field-theoretic simulation studies. Contrary to previous works that typically operate on length scales from nanometers to micrometers, the incorporation of these novel and more realistic interatomic interactions allows to account for the underlying chemical details, thereby substantially enriching FTS models and bringing them closer to particle-based ones.

6

SUMMARY AND OUTLOOK

We shall not cease from exploration
And the end of all our exploring
Will be to arrive where we started
And know the place for the first time.
— T. S. Eliot

The decoupling of particle pair interactions is arguably the hallmark par excellence of field-theoretic modeling approaches. Relying on this fundamental consideration, the field-theoretic framework has evolved over the years into a powerful computational tool for the study of soft matter and, in particular, polymer systems being even at its present stage of development not only a valuable complement to conventional particle-based methods but also often the only computational tool available for tackling certain problems. As has been described in the introduction in Chapter 2, the nature of a statistical field model entails certain advantages which allow the exploration of research areas that have remained practically inaccessible by conventional particle-based techniques. At the same time, however, this characteristic decoupling of pair interactions is accompanied by the challenging task of constructing an inverse potential, which has severely limited the further widespread use of field-theoretic methods to more research-specific areas. Identifying solutions to overcome the inverse potential problem that would open great new possibilities in the field has been the primary motivation behind this dissertation.

In addition to giving the overall picture of field-theoretic simulations, special attention was devoted in Chapter 2 to its underlying modeling principles. Most of them, as well as the new ones brought up in subsequent chapters of the thesis are summarized here, the goal being to provide the reader with a practically complete but also very concise synopsis of the actual work accomplished. To this, and contrary to the usual practice to avoid equations in the summary chapter of a thesis, specific equations are presented again here to facilitate the discussion and keep this chapter somehow independent but simultaneously a coherent part of the thesis. First of all, being a key element of the modeling approach, the Gaussian integral identity,

$$\exp\left(-\frac{\beta}{2}\left\langle\hat{\rho}|u|\hat{\rho}\right\rangle\right) = \frac{\int \mathcal{D}w\ \exp\left(-\frac{1}{2\beta}\left\langle w|u^{-1}|w\right\rangle - i\left\langle w|\hat{\rho}\right\rangle\right)}{\int \mathcal{D}w\ \exp\left(-\frac{1}{2\beta}\left\langle w|u^{-1}|w\right\rangle\right)}, \quad (2.8)$$

also known as the Hubbard–Stratonovich transformation, has been discussed and re-derived. Through it, the pair interactions u with respect to the particle-based microscopic density $\hat{\rho}$ are transformed into a field description containing (at least) one newly introduced auxiliary field w and the inverse potential u^{-1}. Adopting (and slightly adapting) the common procedure, it was next demonstrated how the

use of this identity allows to transform a particle-based canonical partition function into a field-based one,

$$\mathcal{Z}_c \propto \int \mathcal{D}w \, \exp\left(-\mathcal{H}[w]\right), \tag{2.20}$$

and thus derive a statistical field model that is described by the field-theoretic Hamiltonian $\mathcal{H}$. Following a new path, the interaction potential and its inverse, formally connected by

$$\int_{\mathbb{R}^d} \mathrm{d}^d r' \; u(\boldsymbol{r}-\boldsymbol{r}')\, u^{-1}(\boldsymbol{r}'-\boldsymbol{r}'') = \delta(\boldsymbol{r}-\boldsymbol{r}''), \tag{2.53}$$

have then been the main focus of the discussion. In that part of the dissertation, not only have the interactions typically used in FTS been outlined but also a systematic classification of non-bonded pair interactions has been provided for the first time. This classification into explicit, implicit, and masked δ-interactions, as concisely condensed in Table 2.1, exposes the remarkable simplicity of commonly used physical particle-based models, thus motivating the subsequent formulation of the inverse potential problem as the major focus of this work.

The class of masked δ-interactions has been taken up in the first part of Chapter 3. Unlike the other two classes, effective interactions denoted as u' are present here at the particle level whose character is greatly impacted by a masking function Γ and the inversion of the embedded potential u is reduced to a trivial case, that of a delta function. By application of the convolution theorem it has then been demonstrated how the concept of effective potentials can be extended by means of more general masking functions, specified by their Fourier transform

$$\hat{\Gamma}(\boldsymbol{k}) = \sqrt{\frac{\hat{u}'(\boldsymbol{k})}{u_0}}, \tag{3.7}$$

and thus how the variety of available effective potentials can be significantly enriched, and two novel examples were given. In the second part of Chapter 3, first the inverse potential problem has been examined from the viewpoint of the reciprocal space in which u and u^{-1} have been found to be related by

$$\mathcal{F}[u^{-1}](\boldsymbol{k}) = \left(\mathcal{F}[u](\boldsymbol{k})\right)^{-1}. \tag{3.21}$$

After discussing the implications from a potentially problematic decay behavior of the inverse potential in Fourier space, the concept of masking functions has been advanced in a new context, that of the masked inverse potentials. For a particular pair potential, let it be denoted as u_1, the masking of its inverse u_1^{-1} provides a more friendly decay behavior in Fourier space, thus allowing for the straightforward computation of an alternative inverse potential $u_2^{-1} = \Gamma * u_1^{-1} * \Gamma$ as a stand-alone function. By imposing the principle of model equiva-

lence, the statistical weights obtained from the particle-to-field transformation of the alternative model,

$$\int_{V^n} \mathrm{d}^{3n}r \, \exp\left(-\frac{\beta}{2}\langle\rho_2|u_2|\rho_2\rangle\right) \propto \frac{\int \mathcal{D}w \, \exp\left(-\frac{1}{2\beta}\left\langle w\middle|\Gamma * u_1^{-1} * \Gamma\middle|w\right\rangle + n\ln Q[iw]_{\rho_2}\right)}{\int \mathcal{D}w \, \exp\left(-\frac{1}{2\beta}\left\langle w\middle|\Gamma * u_1^{-1} * \Gamma\middle|w\right\rangle\right)}, \tag{3.35}$$

have been constructed by relating ρ_2 to the original ρ_1 so as to match the corresponding statistical weights of the original model. The big advantage of such a modeling approach is that the original model containing the intractable inverse potential u_1^{-1} can be described by an alternative, albeit fully equivalent, model containing an easy-to-use u_2^{-1} in its place. In conclusion to Chapter 3, this new approach has been demonstrated using two popular examples, the Gaussian-regularized Edwards model and the Yukawa potential.

Outside the scope of the three classes of interactions, a novel concept has been elaborated in Chapter 4 which aims at inferring from structural information an inverse potential capable of reproducing these structures by itself. In this case, the inverse potential serves as an interface between the FTS framework and external methods from which u^{-1} can be deduced. By this means, molecular dynamics simulations of monatomic particles interacting via the broadly known Morse potential,

$$u_{\mathrm{Morse}}(r) = \epsilon\Big(\exp\left(-2\xi\left(r - r_{\min}\right)\right) - 2\exp\left(-\xi\left(r - r_{\min}\right)\right)\Big), \tag{4.5}$$

have been conducted and the radial distribution function g_{MD} has been computed. On the side of a hybrid particle-field model, and using the saddle-point approximation, the saddle-point density ρ^* is dictated by the MD-computed g_{MD} and the saddle-point field configuration

$$w_{\mathrm{Q}}^*(\boldsymbol{r}) = i\beta u(\boldsymbol{r}) + i\ln\left(\rho^*(\boldsymbol{r})/\rho_0\right) + i\ln Q^{(\mathrm{HPF})} \tag{4.22}$$

derived from it. Closing the circle of this consistent approach, the inverse potential is extracted from the saddle-point equation

$$\frac{1}{\beta}\left[u_{\mathrm{Q}}^{-1} * w_{\mathrm{Q}}^*\right](\boldsymbol{r}) + i\rho^*(\boldsymbol{r}) = 0 \tag{4.24}$$

where it is the only unknown. In subsequent stand-alone field simulations, it was shown that the inverse potential thus imposed is indeed capable of reproducing the original structural features. The need for calibration of the imposed inverse potential, as it is also the case for coarse-grained force fields derived and used in particle-based simulations, has further been demonstrated by means of additional simulations and theoretically explained on a sound way.

The remaining aspect of the problem, the actual direct calculation of inverse potentials for advanced interactions, has been the main

subject of Chapter 5. First, in a naive but instructive approach, the pair potential was discretized and then directly inverted numerically by matrix inversion or deconvolution. In continuation of the previous chapter, the Morse potential was used as an example and its inverse

$$u^{-1}(\boldsymbol{r}_i - \boldsymbol{r}_j) \approx u_{ij}^{-1} \tag{5.2}$$

was identified with the corresponding element of the inverse matrix. Practically identical results from this (matrix inversion) approach were obtained with those from a computationally more favorable one based on deconvolution, which was very encouraging as it helped understand the naive direct inversion in view of the difficult characteristics of inverses apparent in Fourier space, examined in detail in Chapter 3. Also, the strong dependence of the naively derived inverse potential on the discretization chosen was reasoned by comparing against a complementary theoretical approach using a discretization-induced numerical wavenumber cutoff working against the divergence of $\hat{u}^{-1}$ as $k \to \infty$. In the remainder of the chapter, this behavior of the Fourier transform $\hat{u}^{-1}$ served to inspire the analytical inversion of the Morse potential in terms of implicit δ-interactions. A particularly advantageous relation in Fourier space,

$$(i\boldsymbol{k})^n \leftrightarrow \mathcal{F}\left[\nabla^n \delta\right](\boldsymbol{k}), \tag{5.5}$$

has been exploited for this class of interactions to write terms represented in Fourier space as polynomials of the wave vector by real-space derivatives of the Dirac delta function. This has allowed to identify the inverse of an exponential function $u_e(\boldsymbol{r}) = A\exp(-B\,|\boldsymbol{r}|)$ in the context of implicit δ-interactions,

$$u_e^{-1}(\boldsymbol{r}) = \frac{1}{8\pi AB}\left(\nabla^4\delta(\boldsymbol{r}) - 2B^2\nabla^2\delta(\boldsymbol{r}) + B^4\delta(\boldsymbol{r})\right). \tag{5.11}$$

The two exponential terms of the Morse potential have been split accordingly for inversion thereby treating the repulsive and the attractive part separately. Building on the hybrid particle-field model from Chapter 4, this model was extended to a two-field model employing the two analytic inverses of the corresponding components of the Morse potential. A series of numerical studies have subsequently been carried out to demonstrate the straightforwardness of implementing such novel interactions in practice and deriving structural properties from them. In analogy to the previous chapter, the limitations of the saddle-point approximation used as an easy-to-understand demonstration case have been thoroughly pointed out in conclusion of this part.

Within the conceptual summary of the main chapters of this dissertation, the consideration of the inverse potential problem is concisely illustrated from fundamentally different perspectives. The breakdown into effective interactions and masked inverse potentials (Chapter 3) and the ideas of externally imposed inverse potentials (Chapter 4) or analytically derived ones (Chapter 5) constitutes a systematic subdivision of the problem allowing for different solutions and different

levels of consideration, and provides an overall conceptually complete picture. Given that multi-body interaction potentials beyond pair ones, such as 3-body (bending) or 4-body (torsion) angle potentials, are typically modeled at the level of individual molecules suggesting a treatment in terms of reduced, more elaborate partition functions (Chapter 2) without any inversions involved, the picture of advanced interactions in field-theoretic models appears indeed complete. This allows for the foundation of next-generation field-theoretic simulations involving detailed chemically-informed molecular models, thus having inconceivably many and diverse potential applications in the continuing study of soft matter and polymeric materials.

The statistical nature of these models renders the study of especially thermodynamic properties particularly straightforward and obvious. Also, the closer relation of these advanced field descriptions to particle-based ones capable of addressing dynamic properties could significantly facilitate the development of new approaches for tackling nonequilibrium properties. After all, field-theoretic models with advanced interactions may naturally be applied to areas where field-theoretic descriptions have already proven to have great advantages over particle-based methods. A prime example is the large field of polymer self-assembly, which has already been explored by simpler, phenomenological models, thus often requiring calibration or tuning of key model parameters. A multitude of other predestined application areas, some of which are already cited in this dissertation including those of hybrid particle-field theories, can also benefit from richer, more sophisticated interaction models. Having addressed the intrinsic problem of implementing physical interactions in field-theoretic simulations, the conceivable applications seem manifold and good developments will follow naturally.

A

APPENDIX

Beauty, I hear you ask; do not the Graces flee
where integrals stretch forth their necks?
— Ludwig Boltzmann

A.1 DETAILS OF THE HUBBARD–STRATONOVICH TRANSFORMATION

In this supplementary section a derivation of a Gaussian integral identity, in the context of auxiliary field theory also called the Hubbard–Stratonovich transformation, will be sketched using the limiting case $d \to \infty$ for conventional d-dimensional Gaussian integrals.

For d-dimensional Gaussian integrals the following relation can be found:

$$\int_{\mathbb{R}^d} \exp\left(-\frac{1}{2}\boldsymbol{x}^T \cdot \boldsymbol{A} \cdot \boldsymbol{x} + \boldsymbol{b}^T \cdot \boldsymbol{x}\right) \mathrm{d}^d x = \sqrt{\frac{(2\pi)^d}{\det \boldsymbol{A}}} \exp\left(\frac{1}{2}\boldsymbol{b}^T \cdot \boldsymbol{A}^{-1} \cdot \boldsymbol{b}\right), \tag{A.1.1}$$

with the column vector $\boldsymbol{x}$, $\boldsymbol{b} \in \mathbb{C}^d$ and with a positive-definite real part of the complex matrix $\boldsymbol{A} \in \mathbb{C}^{d\times d}$.

To go over to a representation for continuous functions, a continuous function w is first interpreted as a limiting case $d \to \infty$ of its discrete representation given by the d-component vector $\boldsymbol{w} = \Big(w(\boldsymbol{r}_1), w(\boldsymbol{r}_2), \ldots, w(\boldsymbol{r}_d)\Big)^T$ with argument vectors $\boldsymbol{r}_i$. The functional integral is then loosely expressed in the limiting case by a d-dimensional conventional integral involving this discrete representation:

$$\int \mathcal{D}w\, F[w] = \lim_{d\to\infty} \int \mathrm{d}^d w\, F(\boldsymbol{w}). \tag{A.1.2}$$

As can be seen, the functional $F[w]$ is transformed into a conventional function $F(\boldsymbol{w})$ depending on d variables. In a similar way, functionals of continuous functions are to be described in the limiting case $d \to \infty$ by their discrete counterpart. As an example, a functional consisting of the functions $\rho(\boldsymbol{r})$ and $u(\boldsymbol{r})$ (which can describe, for in-

stance, a density field and a pair potential) can be loosely written by discretization of the integrals as

$$\langle\rho|u|\rho\rangle = \int_{\mathbb{R}^3} \mathrm{d}^3r \int_{\mathbb{R}^3} \mathrm{d}^3r'\ \rho(\boldsymbol{r})u(\boldsymbol{r}-\boldsymbol{r}')\rho(\boldsymbol{r}') \tag{A.1.3}$$

$$\begin{aligned}\approx \Delta V^2 \Big[&\rho(\boldsymbol{r}_1)u(\boldsymbol{r}_1-\boldsymbol{r}_1)\rho(\boldsymbol{r}_1) + ... + \rho(\boldsymbol{r}_d)u(\boldsymbol{r}_d-\boldsymbol{r}_1)\rho(\boldsymbol{r}_1)\\ &+\rho(\boldsymbol{r}_1)u(\boldsymbol{r}_1-\boldsymbol{r}_2)\rho(\boldsymbol{r}_2) + ... + \rho(\boldsymbol{r}_d)u(\boldsymbol{r}_d-\boldsymbol{r}_2)\rho(\boldsymbol{r}_2)\\ &+ ...\\ &+\rho(\boldsymbol{r}_1)u(\boldsymbol{r}_1-\boldsymbol{r}_d)\rho(\boldsymbol{r}_d) + ... + \rho(\boldsymbol{r}_d)u(\boldsymbol{r}_d-\boldsymbol{r}_d)\rho(\boldsymbol{r}_d)\Big]\end{aligned} \tag{A.1.4}$$

$$= \Delta V^2 \sum_{i=1}^{d}\sum_{j=1}^{d} \rho(\boldsymbol{r}_i)u(\boldsymbol{r}_i-\boldsymbol{r}_j)\rho(\boldsymbol{r}_j) \tag{A.1.5}$$

$$=: \sum_{i=1}^{d}\sum_{j=1}^{d} \rho_i u_{ij}\rho_j \tag{A.1.6}$$

$$= \boldsymbol{\rho}^T\cdot\boldsymbol{u}\cdot\boldsymbol{\rho}, \tag{A.1.7}$$

where we defined $\rho_i := \rho(\boldsymbol{r}_i)$ and $u_{ij} := \Delta V^2 u(\boldsymbol{r}_i-\boldsymbol{r}_j)$ with $\boldsymbol{\rho}\in\mathbb{R}^d$, and $\boldsymbol{u}\in\mathbb{R}^{d\times d}$ required to be a positive definite matrix. The prefactor ΔV^2 in u_{ij} is introduced to comply with the unit of the continuous counterpart. With Eqs. (A.1.1), (A.1.2), and (A.1.7) equipped, the Gaussian functional identity can now be derived:

$$\exp\left(\frac{1}{2}\langle\rho|u|\rho\rangle\right) = \lim_{d\to\infty}\exp\left(\frac{1}{2}\boldsymbol{\rho}^T\cdot\boldsymbol{u}\cdot\boldsymbol{\rho}\right) \tag{A.1.8}$$

$$= \lim_{d\to\infty}\sqrt{\frac{\det\boldsymbol{u}^{-1}}{(2\pi)^d}}\int_{\mathbb{R}^d}\exp\left(-\frac{1}{2}\boldsymbol{w}^T\cdot\boldsymbol{u}^{-1}\cdot\boldsymbol{w}+\boldsymbol{\rho}^T\cdot\boldsymbol{w}\right)\mathrm{d}^dw \tag{A.1.9}$$

$$= \lim_{d\to\infty}\frac{\int_{\mathbb{R}^d}\exp\left(-\frac{1}{2}\boldsymbol{w}^T\cdot\boldsymbol{u}^{-1}\cdot\boldsymbol{w}+\boldsymbol{\rho}^T\cdot\boldsymbol{w}\right)\ \mathrm{d}^dw}{\int_{\mathbb{R}^d}\exp\left(-\frac{1}{2}\boldsymbol{w}^T\cdot\boldsymbol{u}^{-1}\cdot\boldsymbol{w}\right)\ \mathrm{d}^dw} \tag{A.1.10}$$

$$= \lim_{d\to\infty}\frac{\int_{\mathbb{R}^d}\exp\Big(-\overbrace{\frac{\Delta V^2}{2}\boldsymbol{w}^T\cdot\boldsymbol{u}^{-1}\cdot\boldsymbol{w}}^{\to\frac{1}{2}\langle w|u^{-1}|w\rangle}+\overbrace{\Delta V\boldsymbol{\rho}^T\cdot\boldsymbol{w}}^{\to\langle\rho|w\rangle}\Big)\ \mathrm{d}^dw}{\int_{\mathbb{R}^d}\exp\Big(-\underbrace{\frac{\Delta V^2}{2}\boldsymbol{w}^T\cdot\boldsymbol{u}^{-1}\cdot\boldsymbol{w}}_{\to\frac{1}{2}\langle w|u^{-1}|w\rangle}\Big)\ \mathrm{d}^dw} \tag{A.1.11}$$

$$= \frac{\int\mathcal{D}w\ \exp\Big(-\frac{1}{2}\langle w|u^{-1}|w\rangle+\langle\rho|w\rangle\Big)}{\int\mathcal{D}w\ \exp\Big(-\frac{1}{2}\langle w|u^{-1}|w\rangle\Big)}, \tag{A.1.12}$$

where, by analogy with the requirements of the original Gaussian integral of Eq. (A.1.1), the function u must be positive-definite.

With the substitutions $u \to \beta u$, $\beta > 0$, and $\rho \to c\rho$, $c \in \mathbb{C}$, this result can be brought to a more general form:

$$\exp\left(c^2 \frac{\beta}{2} \langle \rho | u | \rho \rangle\right) = \frac{\int \mathcal{D}w \, \exp\left(-\frac{1}{2\beta} \langle w | u^{-1} | w \rangle + c \langle w | \rho \rangle\right)}{\int \mathcal{D}w \, \exp\left(-\frac{1}{2\beta} \langle w | u^{-1} | w \rangle\right)}. \tag{A.1.13}$$

It is evidently a matter of convention that the choice $c = -i$ is made which leads to the well-known form of the Gaussian integral identity:

$$\exp\left(-\frac{\beta}{2} \langle \rho | u | \rho \rangle\right) = \frac{\int \mathcal{D}w \, \exp\left(-\frac{1}{2\beta} \langle w | u^{-1} | w \rangle - i \langle w | \rho \rangle\right)}{\int \mathcal{D}w \, \exp\left(-\frac{1}{2\beta} \langle w | u^{-1} | w \rangle\right)}. \tag{A.1.14}$$

A.2 USEFUL RELATIONS FOR DIRAC'S BRA–KET NOTATION

To avoid frequently occurring cumbersome integral notations, the use of Dirac's Bra–Ket notation seems particularly useful. Following a pioneer work in statistical field theory [121], one may introduce the notation

$$\langle f | g \rangle := \int_V \mathrm{d}^3 r \, f(\boldsymbol{r}) \, g(\boldsymbol{r}) \tag{A.2.1}$$

and

$$\langle f | h | g \rangle := \int_V \mathrm{d}^3 r \int_V \mathrm{d}^3 r' \, f(\boldsymbol{r}) h(\boldsymbol{r} - \boldsymbol{r}') g(\boldsymbol{r}'), \tag{A.2.2}$$

with f, g, h describing general (placeholder) functions in this context. Since this Bra-Ket notation in the field-theoretic context is motivated by Gaussian integrals, the absence of complex conjugation in Eqs. (A.2.1) and (A.2.2) (in contrast to the original usage in the quantum mechanical context) is intentional and no mistake. Consequently, the functions can be directly exchanged as

$$\langle f | g \rangle = \langle g | f \rangle \tag{A.2.3}$$

and

$$\langle f | h | g \rangle = \langle g | h | f \rangle . \tag{A.2.4}$$

For general $h(\boldsymbol{r})$, Eq. (A.2.2) can be transformed to Eq. (A.2.1) using the convolution notation:

$$\begin{aligned} \langle f | h | g \rangle &= \int_V \mathrm{d}^3 r \int_V \mathrm{d}^3 r' \, f(\boldsymbol{r}) h(\boldsymbol{r} - \boldsymbol{r}') g(\boldsymbol{r}') \\ &= \int_V \mathrm{d}^3 r \, f(\boldsymbol{r}) \int_V \mathrm{d}^3 r' \, h(\boldsymbol{r} - \boldsymbol{r}') g(\boldsymbol{r}') \\ &= \int_V \mathrm{d}^3 r \, f(\boldsymbol{r}) \, [h * g] \, (\boldsymbol{r}) \\ &= \langle f | h * g \rangle , \end{aligned} \tag{A.2.5}$$

and especially for $h(\boldsymbol{r}) = \delta(\boldsymbol{r})$, Eq. (A.2.2) directly transforms into Eq. (A.2.1):

$$\langle f|\delta|g\rangle = \langle f|\delta * g\rangle = \langle f|g\rangle\,. \tag{A.2.6}$$

Applying the interchangeability properties from Eqs. (A.2.3) and (A.2.4) to Eq. (A.2.5), the interchangeability of the convolution can be found:

$$\langle f|h * g\rangle = \langle h * f|g\rangle\,. \tag{A.2.7}$$

Convolutions with a general (masking) function Γ can also be swapped between the inner and outer functions:

$$\begin{aligned}\langle f|h|\Gamma * g\rangle &= \langle f|h * (\Gamma * g)\rangle \\ &= \langle f|(h * \Gamma) * g\rangle \\ &= \langle f|h * \Gamma|g\rangle\end{aligned} \tag{A.2.8}$$

and similarly

$$\langle \Gamma * f|h|\Gamma * g\rangle = \langle f|\Gamma * h * \Gamma|g\rangle\,. \tag{A.2.9}$$

Using the convention of the Fourier transform employed in this dissertation, a relation between the functions f and g in the spatial domain to their Fourier transformed functions $\hat{f}$ and $\hat{g}$ in the reciprocal domain can be established for the Bra-Ket notation as

$$\begin{aligned}\langle f|g\rangle &= \frac{1}{(2\pi)^3}\int_{\mathbb{R}^3}\mathrm{d}^3k\int_{\mathbb{R}^3}\mathrm{d}^3k'\;\hat{f}(\boldsymbol{k})\hat{g}(\boldsymbol{k}') \\ &\qquad\times\underbrace{\frac{1}{(2\pi)^3}\int_{\mathbb{R}^3}\mathrm{d}^3r\;\exp\left(i\left(\boldsymbol{k}+\boldsymbol{k}'\right)\cdot\boldsymbol{r}\right)}_{=\delta(\boldsymbol{k}+\boldsymbol{k}')} \\ &= \frac{1}{(2\pi)^3}\int_{\mathbb{R}^3}\mathrm{d}^3k\;\hat{f}(\boldsymbol{k})\hat{g}(-\boldsymbol{k}) \\ &= \frac{1}{(2\pi)^3}\langle\hat{f}|\mathcal{P}\hat{g}\rangle\end{aligned} \tag{A.2.10}$$

and in analogy also

$$\langle f|g\rangle = \frac{1}{(2\pi)^3}\langle\mathcal{P}\hat{f}|\hat{g}\rangle \tag{A.2.11}$$

where $\mathcal{P}\hat{f}(\boldsymbol{k}) := \hat{f}(-\boldsymbol{k})$ and the integration domains being chosen here as $\mathbb{R}^3$ to rigorously consider the definition of the Fourier transform. Using Eq. (A.2.5) and applying the convolution theorem, it is also possible to find

$$\langle f|h|g\rangle = \frac{1}{(2\pi)^3}\langle\mathcal{P}\hat{f}|\hat{h}\,\hat{g}\rangle. \tag{A.2.12}$$

If $f \in \mathbb{R}$, then $\mathcal{P}\hat{f} = \overline{\hat{f}}$ (the complex conjugate) and Eqs. (A.2.11) and (A.2.12) can be rewritten as

$$\langle f|g\rangle = \frac{1}{(2\pi)^3}\langle\overline{\hat{f}}|\hat{g}\rangle, \tag{A.2.13}$$

$$\langle f|h|g\rangle = \frac{1}{(2\pi)^3}\langle\overline{\hat{f}}|\hat{h}\,\hat{g}\rangle. \tag{A.2.14}$$

A.3 STATIC STRUCTURE FACTOR AND RADIAL DISTRIBUTION FUNCTION

Different definitions, conventions, and approximations used in the theoretical introduction of the static structure factor may seem somewhat confusing at first glance. To establish more conceptual clarity, this section shall provide a theoretical basis for understanding the static structure factor and the associated radial distribution function.

Consistent with the notation from Reference [19], the radial distribution function of a homogeneous and isotropic system is defined as

$$g(\boldsymbol{r}) = \frac{1}{V} \int \mathrm{d}^3 r' \; g_N^{(2)} \left(\boldsymbol{r}, \boldsymbol{r}'\right), \tag{A.3.1}$$

with the n-particle distribution function

$$g_N^{(n)} \left(\boldsymbol{r}^n\right) = \frac{\rho_N^{(n)} \left(\boldsymbol{r}_1, ..., \boldsymbol{r}_n\right)}{\prod_{i=1}^n \rho_N^{(1)} \left(\boldsymbol{r}_i\right)}, \tag{A.3.2}$$

where $\rho_N^{(n)} \left(\boldsymbol{r}_1, ..., \boldsymbol{r}_n\right)$ is the n-particle density. Concerning the latter, the single-particle density

$$\rho_N^{(1)} \left(\boldsymbol{r}\right) = \left\langle \sum_{i=1}^N \delta \left(\boldsymbol{r} - \boldsymbol{r}_i\right) \right\rangle =: \left\langle \hat{\rho} \left(\boldsymbol{r}\right) \right\rangle \tag{A.3.3}$$

and the pair density

$$\rho_N^{(2)} \left(\boldsymbol{r}, \boldsymbol{r}'\right) = \left\langle \sum_{i=1}^N \sum_{j \neq i} \delta(\boldsymbol{r} - \boldsymbol{r}_i) \delta(\boldsymbol{r}' - \boldsymbol{r}_j) \right\rangle \tag{A.3.4}$$

$$= \left\langle \sum_{i=1}^N \delta(\boldsymbol{r} - \boldsymbol{r}_i) \sum_{j=1}^N \delta(\boldsymbol{r}' - \boldsymbol{r}_j) - \sum_{i=1}^N \delta(\boldsymbol{r} - \boldsymbol{r}_i) \delta(\boldsymbol{r}' - \boldsymbol{r}_i) \right\rangle \tag{A.3.5}$$

$$= \left\langle \hat{\rho}(\boldsymbol{r}) \hat{\rho}(\boldsymbol{r}') \right\rangle - \left\langle \sum_{i=1}^N \delta(\boldsymbol{r} - \boldsymbol{r}_i) \delta(\boldsymbol{r}' - \boldsymbol{r}_i) \right\rangle \tag{A.3.6}$$

are of special interest. Following Ref. [19], the static structure factor can be generally derived from the Fourier transformed microscopic density $\mathcal{F}[\hat{\rho}](\boldsymbol{k})$ as

$$\mathcal{S}(\boldsymbol{k}) = \left\langle \frac{1}{N}\mathcal{F}[\hat{\rho}](\boldsymbol{k})\ \mathcal{F}[\hat{\rho}](-\boldsymbol{k}) \right\rangle \tag{A.3.7}$$

$$= \frac{1}{N}\iint \mathrm{d}^3r\ \mathrm{d}^3r'\ \left\langle \hat{\rho}(\boldsymbol{r})\hat{\rho}(\boldsymbol{r}')\right\rangle \exp\left(-i\boldsymbol{k}\cdot(\boldsymbol{r}-\boldsymbol{r}')\right) \tag{A.3.8}$$

$$\overset{\text{Eq. (A.3.6)}}{=} \frac{1}{N}\iint \mathrm{d}^3r\ \mathrm{d}^3r'\ \left(\rho_N^{(2)}(\boldsymbol{r},\boldsymbol{r}') + \left\langle \sum_{i=1}^{N}\delta(\boldsymbol{r}-\boldsymbol{r}_i)\delta(\boldsymbol{r}'-\boldsymbol{r}_i)\right\rangle\right) \times \exp\left(-i\boldsymbol{k}\cdot(\boldsymbol{r}-\boldsymbol{r}')\right) \tag{A.3.9}$$

$$\overset{\text{Eq. (A.3.2)}}{=} \frac{1}{N}\iint \mathrm{d}^3r\ \mathrm{d}^3r'\ g_N^{(2)}(\boldsymbol{r},\boldsymbol{r}')\underbrace{\left\langle\hat{\rho}(\boldsymbol{r})\right\rangle\left\langle\hat{\rho}(\boldsymbol{r}')\right\rangle}_{=:\rho_0^2=\frac{N^2}{V^2}}\exp\left(-i\boldsymbol{k}\cdot(\boldsymbol{r}-\boldsymbol{r}')\right) + \underbrace{\frac{1}{N}\left\langle\sum_{i=1}^{N}\iint \mathrm{d}^3r\ \mathrm{d}^3r'\ \delta(\boldsymbol{r}-\boldsymbol{r}_i)\delta(\boldsymbol{r}'-\boldsymbol{r}_i)\exp\left(-i\boldsymbol{k}\cdot(\boldsymbol{r}-\boldsymbol{r}')\right)\right\rangle}_{=1} \tag{A.3.10}$$

$$\overset{\substack{\boldsymbol{u}:=\boldsymbol{r}-\boldsymbol{r}',\\ \boldsymbol{R}:=\frac{1}{2}(\boldsymbol{r}+\boldsymbol{r}')}}{=} 1 + \frac{\rho_0^2}{N}\int \mathrm{d}^3u\ \exp(-i\boldsymbol{k}\cdot\boldsymbol{u})\underbrace{\int \mathrm{d}^3R\ g_N^{(2)}(\boldsymbol{u},\boldsymbol{R})}_{=Vg(\boldsymbol{u})} \tag{A.3.11}$$

$$= 1 + \rho_0\int \mathrm{d}^3u\ g(\boldsymbol{u})\exp\left(-i\boldsymbol{k}\cdot\boldsymbol{u}\right) \tag{A.3.12}$$

$$= 1 + \rho_0\int \left(g(\boldsymbol{u})-1\right)\exp\left(-i\boldsymbol{k}\cdot\boldsymbol{u}\right)\mathrm{d}^3u + (2\pi)^3\rho_0\delta(\boldsymbol{k}). \tag{A.3.13}$$

To address the last term in Eq. (A.3.13), as done, for example, in Ref. [98][1], it is natural to define an adapted version of the static structure factor as

$$S(\boldsymbol{k}) := \mathcal{S}(\boldsymbol{k}) - (2\pi)^3\rho_0\delta(\boldsymbol{k}) \tag{A.3.14}$$

and Eq. (A.3.13) can be written as

$$S(\boldsymbol{k}) - 1 = \rho_0\int \mathrm{d}^3r\ \left(g(\boldsymbol{r})-1\right)\exp\left(-i\boldsymbol{k}\cdot\boldsymbol{r}\right), \tag{A.3.15}$$

where, up to a prefactor ρ_0, $S(\boldsymbol{k})-1$ and $g(\boldsymbol{r})-1$ turn out to be Fourier transform pairs. For a homogeneous system, that is $\langle\hat{\rho}(\boldsymbol{r})\rangle = \rho_0$, Eq. (A.3.15) can be alternatively written as

$$S(\boldsymbol{k}) = \frac{1}{N}\iint \mathrm{d}^3r\ \mathrm{d}^3r'\ \left(\left\langle\hat{\rho}(\boldsymbol{r})\hat{\rho}(\boldsymbol{r}')\right\rangle - \left\langle\hat{\rho}(\boldsymbol{r})\right\rangle\left\langle\hat{\rho}(\boldsymbol{r}')\right\rangle\right)\exp(-i\boldsymbol{k}\cdot(\boldsymbol{r}-\boldsymbol{r}')) \tag{A.3.16}$$

$$=: \frac{1}{N}\iint \mathrm{d}^3r\ \mathrm{d}^3r'\ \left\langle\delta\hat{\rho}(\boldsymbol{r})\delta\hat{\rho}(\boldsymbol{r}')\right\rangle\exp\left(-i\boldsymbol{k}\cdot(\boldsymbol{r}-\boldsymbol{r}')\right), \tag{A.3.17}$$

where $\delta\hat{\rho}(\boldsymbol{r}) := \hat{\rho}(\boldsymbol{r}) - \langle\hat{\rho}(\boldsymbol{r})\rangle$.

1 As argued in this reference, this part can be attributed physically in scattering experiments to the "coherent forward scattering" of the beam passing through the probe.

BIBLIOGRAPHY

1. Staudinger, H. Über Polymerisation. *Berichte der deutschen chemischen Gesellschaft (A and B Series)* **53,** 1073 (1920).
2. Whitfield, R., Parkatzidis, K., Truong, N. P., Junkers, T. & Anastasaki, A. Tailoring Polymer Dispersity by RAFT Polymerization: A Versatile Approach. *Chem* **6,** 1340 (2020).
3. Flory, P. J. *Principles of Polymer Chemistry* (Cornell University Press, 1953).
4. Gennes, P. G. de. Reptation of a Polymer Chain in the Presence of Fixed Obstacles. *The Journal of Chemical Physics* **55,** 572 (1971).
5. Doi, M. & Edwards, S. F. Dynamics of concentrated polymer systems. Part 1.—Brownian motion in the equilibrium state. *J. Chem. Soc., Faraday Trans. 2* **74,** 1789 (1978).
6. Rubinstein, M. & Colby, R. H. *Polymer Physics* (Oxford University Press, 2003).
7. Rubinstein, M. Polymer physics—The ugly duckling story: Will polymer physics ever become a part of "proper" physics? *Journal of Polymer Science Part B: Polymer Physics* **48,** 2548 (2010).
8. Ganesan, V. & Fredrickson, G. H. Field-theoretic polymer simulations. *EPL (Europhysics Letters)* **55,** 814 (2001).
9. Levine, I. N. *Quantum Chemistry* (Pearson, 2014).
10. Leach, A. R. *Molecular Modelling: Principles and Applications* (Pearson Education, 2001).
11. Frenkel, D. & Smit, B. *Understanding Molecular Simulation* Second (Academic Press, San Diego, 2002).
12. Müller-Plathe, F. Coarse-Graining in Polymer Simulation: From the Atomistic to the Mesoscopic Scale and Back. *ChemPhysChem* **3,** 754 (2002).
13. Chen, C., Depa, P., Sakai, V. G., Maranas, J. K., Lynn, J. W., Peral, I. & Copley, J. R. A comparison of united atom, explicit atom, and coarse-grained simulation models for poly(ethylene oxide). *The Journal of Chemical Physics* **124,** 234901 (2006).
14. Hoogerbrugge, P. & Koelman, J. Simulating microscopic hydrodynamic phenomena with dissipative particle dynamics. *EPL (Europhysics Letters)* **19,** 155 (1992).
15. Koelman, J. & Hoogerbrugge, P. Dynamic Simulations of Hard-Sphere Suspensions Under Steady Shear. *EPL (Europhysics Letters)* **21,** 363 (1993).
16. Español, P. & Warren, P. Statistical Mechanics of Dissipative Particle Dynamics. *EPL (Europhysics Letters)* **30,** 191 (1995).

17. Groot, R. D. & Warren, P. B. Dissipative particle dynamics: Bridging the gap between atomistic and mesoscopic simulation. *The Journal of Chemical Physics* **107,** 4423 (1997).

18. Español, P., Serrano, M., Pagonabarraga, I. & Zúñiga, I. Energy-conserving coarse-graining of complex molecules. *Soft Matter* **12,** 4821 (2016).

19. Hansen, J.-P. & McDonald, I. R. *Theory of Simple Liquids: With Applications to Soft Matter* Fourth Edition (Academic Press, Oxford, 2013).

20. Forsman, J. & Woodward, C. E. in *Variational Methods in Molecular Modeling* 101 (Springer Singapore, Singapore, 2017).

21. Anderson, J. D. & Wendt, J. *Computational Fluid Dynamics* Third (Springer, 2009).

22. Caillol, J.-M., Patsahan, O. & Mryglod, I. The collective variables representation of simple fluids from the point of view of statistical field theory. *Condensed Matter Physics* **8,** 665 (2005).

23. Caillol, J.-M., Patsahan, O. & Mryglod, I. Statistical field theory for simple fluids: The collective variables representation. *Physica A: Statistical Mechanics and its Applications* **368,** 326 (2006).

24. Sherck, N., Shen, K., Nguyen, M., Yoo, B., Köhler, S., Speros, J. C., Delaney, K. T., Shell, M. S. & Fredrickson, G. H. Molecularly Informed Field Theories from Bottom-up Coarse-Graining. *ACS Macro Letters* **10,** 576 (2021).

25. Edwards, S. F. & Freed, K. F. Cross linkage problems of polymers I. The method of second quantization applied to the cross linkage problem of polymers. *Journal of Physics C: Solid State Physics* **3,** 739 (1970).

26. Edwards, S. F. & Freed, K. F. Cross linkage problems of polymers II. Dilute cross linked systems of polymers. *Journal of Physics C: Solid State Physics* **3,** 750 (1970).

27. Edwards, S. F. & Freed, K. F. Cross linkage problem of polymers III. Dense cross linked system of polymers. *Journal of Physics C: Solid State Physics* **3,** 760 (1970).

28. Fredrickson, G. H. & Delaney, K. T. Coherent states field theory in supramolecular polymer physics. *The Journal of Chemical Physics* **148,** 204904 (2018).

29. Edwards, S. F. The statistical mechanics of polymers with excluded volume. *Proceedings of the Physical Society* **85,** 613 (1965).

30. Edwards, S. F. The theory of polymer solutions at intermediate concentration. *Proceedings of the Physical Society* **88,** 265 (1966).

31. Fredrickson, G. H., Ganesan, V. & Drolet, F. Field-Theoretic Computer Simulation Methods for Polymers and Complex Fluids. *Macromolecules* **35,** 16 (2002).

32. Fredrickson, G. H. Computational field theory of polymers: opportunities and challenges. *Soft Matter* **3,** 1329 (2007).

33. Fredrickson, G. H. & Delaney, K. T. Field-theoretic simulations: An emerging tool for probing soft material assembly. *MRS Bulletin* **43,** 371 (2018).

34. Delaney, K. T. & Fredrickson, G. H. Recent Developments in Fully Fluctuating Field-Theoretic Simulations of Polymer Melts and Solutions. *The Journal of Physical Chemistry B* **120,** 7615 (2016).

35. Matsen, M. W. & Beardsley, T. M. Field-theoretic simulations for block copolymer melts using the partial saddle-point approximation. *Polymers* **13,** 2437 (2021).

36. Beardsley, T. M., Spencer, R. K. W. & Matsen, M. W. Computationally Efficient Field-Theoretic Simulations for Block Copolymer Melts. *Macromolecules* **52,** 8840 (2019).

37. Vorselaars, B., Stasiak, P. & Matsen, M. W. Field-Theoretic Simulation of Block Copolymers at Experimentally Relevant Molecular Weights. *Macromolecules* **48,** 9071 (2015).

38. Bates, F. S., Hillmyer, M. A., Lodge, T. P., Bates, C. M., Delaney, K. T. & Fredrickson, G. H. Multiblock Polymers: Panacea or Pandora's Box? *Science* **336,** 434 (2012).

39. Ginzburg, V., Weinhold, J., Hustad, P., Trefonas, P., Kim, B., Laachi, N. & Fredrickson, G. in *Directed Self-assembly of Block Co-polymers for Nano-manufacturing* (eds Gronheid, R. & Nealey, P.) 67 (Woodhead Publishing, 2015).

40. Matsen, M. Field theoretic approach for block polymer melts: SCFT and FTS. *The Journal of Chemical Physics* **152,** 110901 (2020).

41. Müller, M. Process-directed self-assembly of copolymers: Results of and challenges for simulation studies. *Progress in Polymer Science* **101,** 101198 (2020).

42. Kriksin, Y. A., Neratova, I. V., Khalatur, P. G. & Khokhlov, A. R. Pattern multiplication by template-guided self-assembly of cylinder-forming copolymers: Field-theoretic and particle-based simulations. *Chemical Physics Letters* **492,** 103 (2010).

43. Vorselaars, B., Spencer, R. K. & Matsen, M. W. Instability of the microemulsion channel in block copolymer-homopolymer blends. *Physical Review Letters* **125,** 117801 (2020).

44. Spencer, R. K. & Matsen, M. W. Coexistence of Polymeric Microemulsion with Homopolymer-Rich Phases. *Macromolecules* **54,** 1329 (2021).

45. Danielsen, S. P. O., McCarty, J., Shea, J.-E., Delaney, K. T. & Fredrickson, G. H. Molecular design of self-coacervation phenomena in block polyampholytes. *Proceedings of the National Academy of Sciences* **116,** 8224 (2019).

46. Delaney, K. T. & Fredrickson, G. H. Theory of polyelectrolyte complexation—Complex coacervates are self-coacervates. *The Journal of Chemical Physics* **146,** 224902 (2017).

47. Riggleman, R. A., Kumar, R. & Fredrickson, G. H. Investigation of the interfacial tension of complex coacervates using field-theoretic simulations. *The Journal of Chemical Physics* **136,** 024903 (2012).

48. Lee, J., Popov, Y. O. & Fredrickson, G. H. Complex coacervation: A field theoretic simulation study of polyelectrolyte complexation. *The Journal of Chemical Physics* **128,** 224908 (2008).

49. Martin, J. M., Li, W., Delaney, K. T. & Fredrickson, G. H. SCFT Study of Diblock Copolymer Melts in Electric Fields: Selective Stabilization of Orthorhombic Fddd Network Phase. *Macromolecules* **51,** 3369 (2018).

50. Martin, J. M., Delaney, K. T. & Fredrickson, G. H. Effect of an electric field on the stability of binary dielectric fluid mixtures. *The Journal of Chemical Physics* **152,** 234901 (2020).

51. Spencer, R. K. & Matsen, M. W. Field-theoretic simulations of bottlebrush copolymers. *The Journal of Chemical Physics* **149,** 184901 (2018).

52. Panagiotou, E., Delaney, K. T. & Fredrickson, G. H. Theoretical prediction of an isotropic to nematic phase transition in bottlebrush homopolymer melts. *The Journal of Chemical Physics* **151,** 094901 (2019).

53. Sides, S. W., Kim, B. J., Kramer, E. J. & Fredrickson, G. H. Hybrid Particle-Field Simulations of Polymer Nanocomposites. *Physical Review Letters* **96,** 250601 (2006).

54. Koski, J. P., Ferrier, R. C., Krook, N. M., Chao, H., Composto, R. J., Frischknecht, A. L. & Riggleman, R. A. Comparison of Field-Theoretic Approaches in Predicting Polymer Nanocomposite Phase Behavior. *Macromolecules* **50,** 8797 (2017).

55. Chao, H., Lindsay, B. J. & Riggleman, R. A. Field-Theoretic Simulations of the Distribution of Nanorods in Diblock Copolymer Thin Films. *The Journal of Physical Chemistry B* **121,** 11198 (2017).

56. Koski, J., Chao, H. & Riggleman, R. A. Field theoretic simulations of polymer nanocomposites. *The Journal of Chemical Physics* **139,** 244911 (2013).

57. Daoulas, K. C. & Müller, M. Single chain in mean field simulations: Quasi-instantaneous field approximation and quantitative comparison with Monte Carlo simulations. *The Journal of Chemical Physics* **125,** 184904 (2006).

58. Daoulas, K. C., Müller, M., Pablo, J. J. de, Nealey, P. F. & Smith, G. D. Morphology of multi-component polymer systems: single chain in mean field simulation studies. *Soft Matter* **2,** 573 (2006).

59. Li, W. & Müller, M. Thermodynamics and Kinetics of Defect Motion and Annihilation in the Self-Assembly of Lamellar Diblock Copolymers. *Macromolecules* **49,** 6126 (2016).

60. Lennon, E. M., Katsov, K. & Fredrickson, G. H. Free Energy Evaluation in Field-Theoretic Polymer Simulations. *Phys. Rev. Lett.* **101,** 138302 (2008).

61. Mezzenga, R., Bo Lee, W. & Fredrickson, G. H. Design of liquid-crystalline foods via field theoretic computer simulations. *Trends in Food Science & Technology* **17.** Functionality in Complex Foods, 220 (2006).

62. Delaney, K. T. & Fredrickson, G. H. Polymer field-theory simulations on graphics processing units. *Computer Physics Communications* **184,** 2102 (2013).

63. Xuan, Y., Delaney, K. T., Ceniceros, H. D. & Fredrickson, G. H. Deep learning and self-consistent field theory: A path towards accelerating polymer phase discovery. *Journal of Computational Physics* **443,** 110519 (2021).

64. Fredrickson, G. H. *The Equilibrium Theory of Inhomogeneous Polymers* (Oxford University Press on Demand, 2006).

65. Hubbard, J. Calculation of Partition Functions. *Physical Review Letters* **3,** 77 (1959).

66. Stratonovich, R. Sov. Phys. Solid State 2, 1824 (1958). *Sov. Phys. Solid State (in Russian)* **2,** 1824 (1958).

67. Edwards, S. The Statistical Thermodynamics of a Gas with Long and Short-range Forces. *Philosophical Magazine* **4,** 1171 (1959).

68. Kac, M. On the Partition Function of a One-Dimensional Gas. *The Physics of Fluids* **2,** 8 (1959).

69. Siegert, A. Partition functions as averages of functionals of Gaussian random functions. *Physica* **26** (1960).

70. Edwards, R. E. *Fourier Series, A Modern Introduction* (Springer-Verlag, New York, 1979).

71. Düchs, D., Delaney, K. T. & Fredrickson, G. H. A multi-species exchange model for fully fluctuating polymer field theory simulations. *The Journal of Chemical Physics* **141,** 174103 (2014).

72. Schoenmaker, W. J. Monte Carlo simulations and complex actions. *Phys. Rev. D* **36,** 1859 (6 1987).

73. Lin, H. Q. & Hirsch, J. E. Monte Carlo versus Langevin methods for nonpositive definite weights. *Phys. Rev. B* **34,** 1964 (3 1986).

74. Hong, K. M. & Noolandi, J. Theory of Inhomogeneous Multicomponent Polymer Systems. *Macromolecules* **14,** 727 (1981).

75. Matsen, M. W. & Schick, M. Stable and Unstable Phases of a Diblock Copolymer Melt. *Physical Review Letters* **72,** 2660 (1994).

76. Schmid, F. Self-consistent-field theories for complex fluids. *Journal of Physics: Condensed Matter* **10,** 8105 (1998).

77. Vigil, D. L., Delaney, K. T. & Fredrickson, G. H. Quantitative Comparison of Field-Update Algorithms for Polymer SCFT and FTS. *Macromolecules* **54,** 9804 (2021).

78. Bender, C. M. & Orszag, S. *Advanced Mathematical Methods for Scientists and Engineers* (McGraw-Hill New York, 1978).

79. Klauder, J. R. A Langevin approach to fermion and quantum spin correlation functions. *Journal of Physics A: Mathematical and General* **16,** L317 (1983).

80. Parisi, G. On complex probabilities. *Physics Letters B* **131,** 393 (1983).

81. Weingarten, D. Complex Probabilities on R^N as Real Probabilities on C^N and an Application to Path Integrals. *Physical Review Letters* **89,** 240201 (2002).

82. Aarts, G., Seiler, E. & Stamatescu, I.-O. Complex Langevin method: When can it be trusted? *Physical Review D* **81,** 054508 (2010).

83. Aarts, G., James, F. A., Seiler, E. & Stamatescu, I.-O. Complex Langevin: etiology and diagnostics of its main problem. *The European Physical Journal C* **71,** 1756 (2011).

84. Weyman, A., Mavrantzas, V. G. & Öttinger, H. C. Field-theoretic simulations beyond δ-interactions: Overcoming the inverse potential problem in auxiliary field models. *The Journal of Chemical Physics* **155,** 024106 (2021).

85. Flory, P. J. Thermodynamics of High Polymer Solutions. *The Journal of Chemical Physics* **10,** 51 (1942).

86. Huggins, M. L. Solutions of Long Chain Compounds. *The Journal of Chemical Physics* **9,** 440 (1941).

87. Glaser, J., Qin, J., Medapuram, P. & Morse, D. C. Collective and Single-Chain Correlations in Disordered Melts of Symmetric Diblock Copolymers: Quantitative Comparison of Simulations and Theory. *Macromolecules* **47,** 851 (2014).

88. Glaser, J., Medapuram, P., Beardsley, T. M., Matsen, M. W. & Morse, D. C. Universality of Block Copolymer Melts. *Physical Review Letters* **113,** 068302 (2014).

89. Beardsley, T. & Matsen, M. Calibration of the Flory-Huggins interaction parameter in field-theoretic simulations. *The Journal of Chemical Physics* **150,** 174902 (2019).

90. Willis, J. D., Beardsley, T. M. & Matsen, M. W. Simple and Accurate Calibration of the Flory–Huggins Interaction Parameter. *Macromolecules* **53,** 9973 (2020).

91. Wang, Z.-G. Fluctuation in electrolyte solutions: The self energy. *Physical Review E* **81,** 021501 (2010).

92. Villet, M. C. & Fredrickson, G. H. Efficient field-theoretic simulation of polymer solutions. *The Journal of Chemical Physics* **141,** 224115 (2014).

93. Villet, M. C. *Advanced Computational Field Theory Methods for Fluctuating Polymer Solutions* PhD thesis (2012).

94. Likos, C. N. Effective interactions in soft condensed matter physics. *Physics Reports* **348,** 267 (2001).

95. Ranjan, A., Qin, J. & Morse, D. C. Linear Response and Stability of Ordered Phases of Block Copolymer Melts. *Macromolecules* **41,** 942 (2008).

96. Leimkuhler, B, Matthews, C & Tretyakov, M. On the long-time integration of stochastic gradient systems. *Proceedings of the Royal Society A: Mathematical, Physical and Engineering Sciences* **470,** 20140120 (2014).

97. Weyman, A., Bier, M., Holm, C. & Smiatek, J. Microphase separation and the formation of ion conductivity channels in poly(ionic liquid)s: A coarse-grained molecular dynamics study. *The Journal of Chemical Physics* **148,** 193824 (2018).

98. Yarnell, J., Katz, M., Wenzel, R. G. & Koenig, S. Structure Factor and Radial Distribution Function for Liquid Argon at 85 K. *Physical Review A* **7,** 2130 (1973).

99. Verlet, L. Computer "Experiments" on Classical Fluids. II. Equilibrium Correlation Functions. *Phys. Rev.* **165,** 201 (1968).

100. Matsumoto, A. Parameters of the Morse Potential from Second Virial Coefficients of Gases. *Zeitschrift für Naturforschung A* **42,** 447 (1987).

101. Lim, T.-C. The Relationship between Lennard-Jones (12-6) and Morse Potential Functions. *Zeitschrift für Naturforschung A* **58,** 615 (2003).

102. Weik, F., Weeber, R., Szuttor, K., Breitsprecher, K., Graaf, J. de, Kuron, M., Landsgesell, J., Menke, H., Sean, D. & Holm, C. ESPResSo 4.0 – An Extensible Software Package for Simulating Soft Matter Systems. *The European Physical Journal Special Topics* **227,** 1789 (2019).

103. Thompson, R. B., Rasmussen, K. O. & Lookman, T. Improved convergence in block copolymer self-consistent field theory by Anderson mixing. *The Journal of Chemical Physics* **120,** 31 (2004).

104. Matsen, M. W. Fast and accurate SCFT calculations for periodic block-copolymer morphologies using the spectral method with Anderson mixing. *The European Physical Journal E* **30,** 361 (2009).

105. Stasiak, P. & Matsen, M. Efficiency of pseudo-spectral algorithms with Anderson mixing for the SCFT of periodic block-copolymer phases. *The European Physical Journal E* **34,** 110 (2011).

106. McQuarrie, D. A. *Statistical Mechanics* (Harper & Row, 1976).

107. Percus, J. K. & Yevick, G. J. Analysis of classical statistical mechanics by means of collective coordinates. *Physical Review* **110,** 1 (1958).

108. Rushbrooke, G. & Scoins, H. On the theory of fluids. *Proceedings of the Royal Society of London. Series A. Mathematical and Physical Sciences* **216,** 203 (1953).

109. Rosenfeld, Y., Schmidt, M., Löwen, H & Tarazona, P. Dimensional crossover and the freezing transition in density functional theory. *Journal of Physics: Condensed Matter* **8,** L577 (1996).

110. Rosenfeld, Y, Schmidt, M., Löwen, H & Tarazona, P. Fundamental-measure free-energy density functional for hard spheres: Dimensional crossover and freezing. *Physical Review E* **55,** 4245 (1997).

111. Weyman, A., Mavrantzas, V. G. & Öttinger, H. C. Direct calculation of the functional inverse of realistic interatomic potentials in field-theoretic simulations. *The Journal of Chemical Physics* **156,** 224115 (2022).

112. Vigil, D. L., Quah, T., Sun, D., Delaney, K. T. & Fredrickson, G. H. Self-Consistent Field Theory Predicts Universal Phase Behavior for Linear, Comb, and Bottlebrush Diblock Copolymers. *Macromolecules* **55,** 4237 (2022).

113. Baeurle, S. A., Martoňák, R. & Parrinello, M. A field-theoretical approach to simulation in the classical canonical and grand canonical ensemble. *The Journal of Chemical Physics* **117,** 3027 (2002).

114. Baeurle, S. A, Efimov, G. V & Nogovitsin, E. A. Calculating field theories beyond the mean-field level. *Europhysics Letters (EPL)* **75,** 378 (2006).

115. Baeurle, S. A., Efimov, G. V. & Nogovitsin, E. A. On a new self-consistent-field theory for the canonical ensemble. *The Journal of Chemical Physics* **124,** 224110 (2006).

116. Baeurle, S. A. Multiscale modeling of polymer materials using field-theoretic methodologies: a survey about recent developments. *Journal of Mathematical Chemistry* **46,** 363 (2009).

117. Milano, G. & Kawakatsu, T. Hybrid particle-field molecular dynamics simulations for dense polymer systems. *The Journal of Chemical Physics* **130,** 214106 (2009).

118. De Nicola, A., Zhao, Y., Kawakatsu, T., Roccatano, D. & Milano, G. Hybrid Particle-Field Coarse-Grained Models for Biological Phospholipids. *Journal of Chemical Theory and Computation* **7,** 2947 (2011).

119. Lakkas, A. T., Sgouros, A. P. & Theodorou, D. N. Self-Consistent Field Theory Coupled with Square Gradient Theory of Free Surfaces of Molten Polymers and Compared to Atomistic Simulations and Experiment. *Macromolecules* **52,** 5337 (2019).

120. Peskin, M. E. & Schroeder, D. V. *An Introduction to Quantum Field Theory* (CRC Press, 2018).

121. Caillol, J.-M. Statistical field theory for simple fluids: mean field and Gaussian approximations. *Molecular Physics* **101,** 1617 (2003).

ACKNOWLEDGMENTS

Love is wise – Hatred is foolish.
— Bertrand Russell

The deepest gratitude I owe to Hans Christian Öttinger for offering me the privilege of conducting my doctoral studies in his group. On my way to becoming an "adult scientist" I was constantly amazed, inspired, and sometimes challenged by his broad and deep scientific understanding and his physical intuition beyond imagination, while at the same time being a humorous and exceedingly interesting person to talk to. My sincere and heartfelt thanks, Hans Christian!

I would like to express my particular thanks to Vlasis Mavrantzas who has supervised my work and has been an invaluable help in jointly processing my ideas, concepts and scientific work. I would also like to thank his family for their understanding of our occasional working together on weekends. It is a great pleasure and honor for me to work with you and I greatly appreciate your always positive and constructive attitude; thank you very much for all of this, Vlasis!

It is my great honor to thank Glenn Fredrickson and Robert "Rob" Riggleman for having a genuine interest in my work and for being part of the examination committee. To you, Rob, I would like to extend my sincere thanks for the stimulating discussions during your short stay at ETH.

I am particularly grateful to Martin Kröger for the countless inspiring and engaging discussions and the fantastic collaboration in a new and very creative computational course at ETH. Thank you, Martin, also for your dedicated and virtually always available support with "the little technical things" and your social commitment in bringing our group closer together!

From the bottom of my heart I would like to thank my long-time roommates and now very good friends Meisam Pourali and Ioanna Tsimouri for the many good moments and enriching discussions but also for the mutual support in difficult pandemic times. Especially the many countless trips to the Swiss mountains over the years with you, Meisam, occasionally joined by our dear friends from the group Xiaocheng Shang and Alberto Montefusco, have constantly allowed me to look at my work with a fresh view and from different perspectives, thus inspiring me to come up with many new ideas.

I feel grateful for the other teaching assistant opportunities under the supervision of Andrei Gusev or Martin Willeke and I would like to thank my fellow colleagues Ahmad Moghimikheirabadi, Aikaterini Galata, and Romain Chessex for the excellent collaboration and the students for their excellent feedback. I would also like to express my thanks to my other colleagues, especially but not exclusively Elia Dietler, Massimo Borelli, Rea Dalipi, Samarth Agrawal, Mohsen

Talebi, Monika Zimmermann, and Alan Luo for the always good relationship and the many entertaining conversations.

I would like to sincerely thank Patricia Horn for her kind support with bureaucratic matters for the doctorate and the always friendly relationship. Besides, I would like to thank Harald Lehmann and Marc Petitmermet for supporting me with technical issues concerning the computing infrastructure of the group.

As a respectful tribute to my formative years in Stuttgart, which have laid the groundwork for this dissertation, I would like to thank Axel Arnold, Maria Fyta, Jens Smiatek, and Christian Holm in particular for introducing me to the field of computational physics and awakening my interest in the study of soft matter and complex fluids, and Holger Cartarius and Markus Bier for educating and dedicatedly guiding me in the principles of theoretical physics.

I sincerely want to thank my family and my friends from Germany on this occasion for their continued support. To you, Maximilian, thank you for our friendship, which we are measuring now already in decades filled with fantastic shared memories. But also thanks to you, Laurin, for the fun times we have had so far applying theoretical physics from our common studies to the real world. To my parents, it is my heartfelt wish to thank them for all the love and support I have received from them throughout my life.

Last but not least, I am grateful to my partner Nina for all her love and support throughout my doctorate and for helping me keep the bigger picture in mind.

CURRICULUM VITAE

PERSONAL DATA

Name	Alexander Weyman
Date of Birth	February 20, 1991
Place of Birth	Dachau, Germany
Citizen of	Germany

EDUCATION

2017 –	ETH Zurich Zurich, Switzerland
2011 – 2016	University of Stuttgart Stuttgart, Germany *Final degree:* Master of Science in Physics
– 2010	Max-Born-Gymnasium (grammar school) Backnang, Germany *Final degree:* Abitur (university entrance diploma)